HYDRODYNAMIC STUDY OF A DUAL FLUIDIZED BED SYSTEM AT ROOM AND ELEVATED TEMPERATURES

by

PAULA ANDREA REYES RAMIREZ

B.Sc, Universidad Industrial de Santander, Colombia, 2006

A THESIS SUBMITTED IN PARTIAL FULFILLMENT OF
THE REQUIREMENTS FOR THE DEGREE OF

MASTER OF APPLIED SCIENCE

in

The Faculty of Graduate and Postdoctoral Studies

(Chemical and Biological Engineering)

THE UNIVERSITY OF BRITISH COLUMBIA

(Vancouver)

September 2013

Abstract

Gasification with in-situ CO_2 looping cycle is a promising technology to produce energy while reducing CO_2 emissions. An alternative reactor concept to carry out the integrated process is a Dual Fluidized Bed (DFB). In this reactor, a solid sorbent is continuously circulated between two vessels to undergo multiple carbonation and sorbent regeneration. A comprehensive understanding of the fluidization characteristics of lime-based sorbents (commonly used for CO_2 capture), solids transport between the vessels, and operational analysis of DFB are important for the design and scale-up of the integrated process.

In this study, the hydrodynamic behaviour of limestone of mean diameter 438 μm in a DFB consisting of a riser interconnected via a loop-seal and a downcomer to a bubbling fluidized bed (BFB) was investigated at temperatures up to 250°C. The effects of operating parameters influencing the performance and stability of the system such as riser superficial gas velocity (2.5-6.5 m/s), aeration velocity (1 to $7U_{mf}$) and solids circulation flux (25-139 kg/m^2·s) on the pressure profiles and cross-sectional average solids holdup in the riser were determined at room temperature. Further experimental work was conducted in the same DFB facility, and employing the same limestone particles to study the effect of scale on hydrodynamics, while increasing the bed temperature. Gas leakage between the coupled fluidized beds and its relationship with operating conditions, was also measured based on a gas tracer technique.

Stable operation of the DFB was obtained under the conditions evaluated. The cross-sectional solids holdup in the riser was found to increase with increasing solids mass flux and decreasing riser gas velocity. The DFB riser operated within the fast fluidization and the dilute-phase transport regimes with the transition point characterized by the presence of accumulative choking. Analysis of the pressure profiles revealed that the pressure head in the loop-seal is an important parameter to obtain high solids circulation flux. Furthermore, the pressure in the BFB was found to influence the rate of leakage of riser product gas into this reactor. Smoother fluidization was obtained at elevated temperatures. The results showed that solids holdup in riser decreased with increasing temperature.

Preface

All the work presented in this thesis was completed by the author under the supervision of Professors Naoko Ellis, Jim Lim and John Grace in the Clean Energy Research Centre (CERC) at the University of British Columbia. The author developed the experimental design, conducted the experimental work, operated the chemical looping pilot plant and compiled the results.

Some of the results from Chapter 3 were presented at the 62nd Canadian Chemical Engineering Conference within the 3rd International Symposium on Gasification and its Applications, October 14-17, 2012 in Vancouver, BC.

Versions of Chapter 3 were also presented as posters at the I, II and III Carbon Management Canada Annual Conferences in 2011- 2013, respectively.

Table of Contents

List of Tables

List of Figures

Nomenclature

Ar	Archimedes Number, $\frac{\rho_g \rho_p d_p^3 g}{\mu^2}$
C_d	Drag coefficient, -
d_p	Surface-volume mean particle diameter, m
$d_{b,max}$	Maximum bubble diameter, m
D	Reactor Diameter, m
g	Gravitational acceleration, m/s^2
G_s	Solids circulation flux, kg/m^2·s
G_s^*	Solids circulation flux at saturation carrying capacity, kg/m^2·s
k	Pressure transducer calibration slope, kPa/V
Fr	Froude Number, $\frac{U_0^2}{gD}$
L	Reactor height, m
$\dot{m}$	Elutriation rate, kg/h
N_{or}	Number of orifices in distributor plate
P	Pressure, kPa
U_a	Aeration velocity in loop-seal, m/s
U_c	Velocity at the onset of turbulent regime, m/s
U_0	Superficial gas velocity, m/s
U_{BFB}	BFB superficial gas velocity, m/s
U_{ms}	Minimum slugging velocity, m/s
U_{mf}	Minimum fluidization velocity, m/s
U_r	Riser superficial gas velocity, m/s
U_t	Particle terminal settling velocity, m/s
Re	Reynolds Number, $\frac{\rho_g U_0 D}{\mu}$
Re_c	Reynolds Number at the onset of turbulent regime, $\frac{\rho_g U_c d_p}{\mu}$
Re_{mf}	Particle Reynolds Number at minimum fluidization conditions, $\frac{\rho_g U_{mf} d_p}{\mu}$
Re_p	Particle Reynolds Number, $\frac{\rho_g U_0 d_p}{\mu}$
V	Voltage, V
V_0	Initial voltage, V
z_r	Height above riser distributor, m

Greek letters

ΔP_r	Pressure drop across riser, kPa
$\Delta P_{r,bottom}$	Pressure drop across riser bottom, kPa
ΔP_{cyc}	Pressure drop across cyclone, kPa
$\Delta P_{ls,v}$	Pressure drop across vertical section of loop-seal, kPa
ΔP_v	Pressure drop across solids control valve, kPa
ΔP_d	Pressure drop across downcomer, kPa
ρ_b	Bulk density, kg/m^3
ρ_p	Particle density, kg/m^3
ρ_g	Gas density, kg/m^3
$\emptyset$	Particle sphericity, -
ε	Voidage, -
ε_{mf}	Voidage at minimum fluidization conditions, -
ε_p	Cross-sectional average solids holdup, -
μ	Gas viscosity, Pa·s

Abbreviations

BFB	Bubbling fluidized bed
CFB	Circulating fluidized bed
DFB	Dual fluidized bed
FCC	Fluid catalytic cracking
GHG	Greenhouse gas
PSD	Particle size distribution
TSI	Total solids inventory
SEM	Scanning electron microscope

Acknowledgments

Dedicated to my husband and my mother,

To whom I owe so much love,

unconditional care and support.

Chapter 1: Introduction

1.1. Overview

Climate change caused by the rise of the earth's mean surface temperature has been the main focus of much of the recent research related to energy. Scientists have demonstrated that the main factor responsible for elevated temperature is the anthropogenic emission of greenhouse gases (GHG) into the atmosphere. Carbon dioxide (CO_2), whose main emission source is fossil fuel combustion, is the largest contributor to the greenhouse effect, accounting for about 64% of total GHG emissions (Gupta et al. 2003).

According to the International Energy Agency (IEA), considering the population growth by 2050, the world energy demand is expected to increase by 50% in the next twenty years (Zero Emissions Platform 2009). Due to their large availability and high energy content, fossil fuels will likely continue to be the primary energy source, contributing approximately 81% of the total energy supply by 2030 (Zero Emissions Platform 2009).

The development and implementation of technologies for power generation based on renewable sources such as biomass, wind, solar, geothermal heat can contribute to the energy supply chain and prevent or significantly reduce CO_2 emissions over the next decades. However, most of these new technologies are at the research stage and require further efforts and advances before they can be implemented at an industrial scale. In the meantime, significant efforts are being made to develop technologies that can assist in the reduction of global warming by stabilizing and controlling CO_2 emissions from combustion sources, without greatly affecting overall plant efficiency.

Carbon Capture and Storage (CCS) could become an economically-attractive and viable alternative to reduce the GHG emissions to the atmosphere. When applying CCS to an industrial process, the CO_2 produced is captured, then compressed, transported and subsequently stored underground (geological sequestration). There are three general approaches to capture the CO_2 from power generation plants: pre-combustion, post-combustion and oxy-fuel combustion. In pre-combustion, the CO_2 is captured before fuel is burned. In post-combustion the CO_2 is separated and recovered from the flue gas; while, in oxy-fuel combustion, fuel is burned in a pure oxygen atmosphere resulting in cleaner combustion and sequestration-ready CO_2 flue gas. The capture step is the most costly phase of the CCS strategy, accounting for as much as 70% to 80% of the overall cost of CCS (ICO_2N, 2009). Consequently, reducing the cost of CO_2 capture is one of the principal focuses of CCS research.

Currently, absorption by amine scrubbing is the closest-to-market technology to separate CO_2 by post-combustion capture. This technology can be integrated to existing power plants where the CO_2 concentration in the flue gas stream is very low. Although amine scrubbing has been widely employed in the oil and gas industry for many decades to remove pollutants such as SO_2 and NO_x, in addition to CO_2, the technology is not cost-effective for CO_2 capture on the scale required for significant GHG mitigation due to the elevated cost of the amine-based solvents and the large energy requirement for regeneration.

1.2. Chemical Looping

Chemical looping is a promising and efficient alternative to amine solvents for the capture and concentration of CO_2 produced by power generation. Chemical looping involves a chemical reaction accomplished at high temperature in two complementary stages. Solids are employed to carry chemical species and heat between two reactors. Apart from generating a nearly pure stream of CO_2 ready for sequestration, the application of chemical looping to power generation also seeks to reduce the cost of the capture step of a CCS project, while maintaining high efficiency. Recently, two alternative chemical looping reaction systems (CO_2 looping cycle and O_2 looping cycle (Anthony, 2008)) have been identified for CO_2 capture in combustion and gasification processes. Figure 1.1 illustrates the principle of these two main looping cycles.

O_2 looping involves two separate reactors, where solids undergo reduction and oxidation. Metal oxides are employed as the solid material to provide the oxygen from the air reactor to the fuel reactor so that the fuel is never in contact with air. In this manner, dilution by nitrogen and the production of nitrogen oxides (NO_x) and other pollutants are inhibited. The metal oxide in its reduced form is re-oxidized in the air reactor before being transferred back to the reducer to complete the loop. The reduction of the metal oxide yields a stream containing CO_2 and H_2O. Thus, the CO_2 produced by the process can be easily and inexpensively sequestered after the water is removed by condensation.
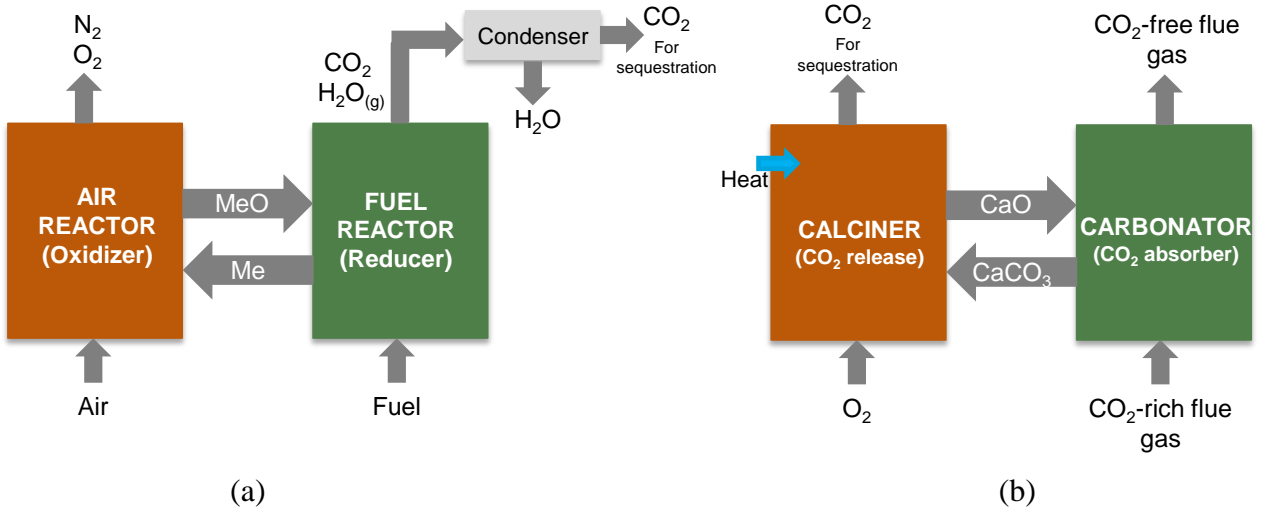
Figure 1.1: Schematic representation of solid looping cycles: (a) O_2 Looping Cycle; (b) CO_2 Looping cycle. (adapted from Anthony, 2008).

The second type of chemical looping system involves a reversible reaction (Eq. 1.1), which is also accomplished in two separate vessels. Instead of metal oxides, solid sorbents, usually calcium-based, are employed to remove CO_2 from the flue gas through the carbonation reaction

$$CaO_{(s)} + CO_{2(g)} \leftrightarrow CaCO_{3(s)} \qquad \Delta H_{298}^0 = -178 \; kJ \; mol^{-1} \qquad (1.1)$$
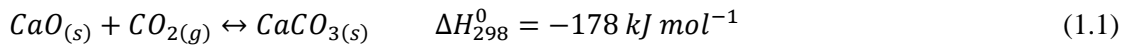
Similar to the O_2 looping cycles, $CaCO_3$ sorbent is regenerated at high temperatures in a different reactor (calciner), where a high-purity stream of CO_2 is released for sequestration (Figure 1.1). The regenerated sorbent is then circulated ("looped") between the two rectors to undergo multiple carbonation-calcination reactions. The highly exothermic carbonation reaction supplies most of the heat necessary for the calcination to take place. Therefore, compared to other post-combustion CO_2 capture technologies such as MEA scrubbing, the calcium looping cycle imposes lower energy penalties associated with sorbent regeneration.

The CO_2 looping cycle usually employs geologically formed calcium-derived sorbents such as limestone and dolomite as the CO_2 carrier. This makes the CO_2 capture economically attractive due to the high availability of these sorbents and their low cost. Moreover, the spent sorbent released in the carbonator has the potential to be used as a feedstock for the production of cement, thereby reducing CO_2 emissions in both industries, and handling and disposal costs (Blamey et al., 2010, Fan et al., 2012).

Both chemical looping schemes can be accomplished with various reactor designs. Due to the fact that good contact between the gas and solid phases is required, as well as continuous transportation of particles between

the vessels, fluidized beds are attractive options for reactor design of this technology. Moreover, fluidized beds appear to be appealing when scaling-up the process since they are well established and widely used in industries such as oil and gas (especially in Fluid Catalytic Cracking (FCC) units).

Thus far, research on looping cycles has mostly focused on technologies employing metal oxides (or chemical looping combustion). Overall, most studies of chemical looping combustion propose a viable way to reduce CO_2 emissions based on completely new power generation facilities using gaseous fuels (like methane) as feedstock.

Looping cycles involving absorption of CO_2 offer a feasible approach to reduce emissions from coal-fired power plants (by post-combustion) and gasification systems (by pre-combustion CO_2 capture). The latter has recently gained attention for a variety of reasons (explained in Section 1.3), but also because CO_2 capture actually improves gasification performance. In addition, since CO_2 is removed within the same reactor where gasification takes place, the high cost associated with new CO_2 capture facilities is likely to be avoided.

Gasification by means of looping and *in-situ* CO_2 capture is described in the next section. Drawbacks related to scale-up and commercialization of this integrated process are also presented.

1.3. Gasification in Dual Fluidized Beds with *in-situ* CO_2 Capture

Gasification is a process where low-value solid or liquid hydrocarbons, or renewable sources are processed to produce a gaseous product which can be used as a fuel for electrical power generation or as a synthetic gas, representing an important pathway for future energy supply. In addition to electricity or steam generation, gasification offers an alternative to the processing of natural gas and feedstocks required for downstream industries such as fertilizers, hydrogen and transportation fuels.

Gasification can be performed in different reactor types, such as fixed beds, moving-beds, entrained flow, bubbling beds, and circulating fluidized beds (including dual fluidized beds) (Pfeifer et al. 2011). More recently, Dual Fluidized Beds (DFB) have increasingly been employed to carry out the gasification process, in which heat released by char combustion in one reactor can be utilized to provide the endothermic heat of gasification reactions, decreasing the need for an external heat source. In addition, by separating the combustion and the gasification zones, it is possible to yield a nearly nitrogen-free product gas (Pfeifer et al. 2004).

Recently, a new approach to further improve the product gas from gasification has been investigated. This is the integration of gasification with *in-situ* CO_2 capture by means of dual fluidized beds. In the combined process, CO_2 is captured by a sorbent from the gasifier reactor, allowing hydrogen production to be improved

4

while reducing CO_2 emissions. Figure 1.2 describes the combined gasification and CO_2 looping cycle. Here, the bed material (commonly CaO) absorbs CO_2 from the gasifier through carbonation reaction at temperatures of 600-700°C. The bed material as $CaCO_3$, together with the char produced in the gasifier, are then transferred to the adjacent reactor where the sorbent is regenerated by calcination at higher temperature. In this second reactor, combustion of char or other fuel also takes place with air, enriched air or oxygen as the fluidizing agent. Subsequently, regenerated sorbent is cycled back to the gasifier/carbonator to complete the loop. As in DFB gasification where olivine or sand acts as heat carrier between reactors, the circulation of Ca-derived sorbent carries heat from the combustion reactor to the gasifier reactor.

Flue gas+
CO_2

H_2-rich
syngas

CaO
+
Heat

COMBUSTOR/
CALCINER

800-900ºC

GASIFIER/
CARBONATOR

600-700ºC

Biomass/
Coal

$CaCO_3$,
char

Air/O_2

Steam
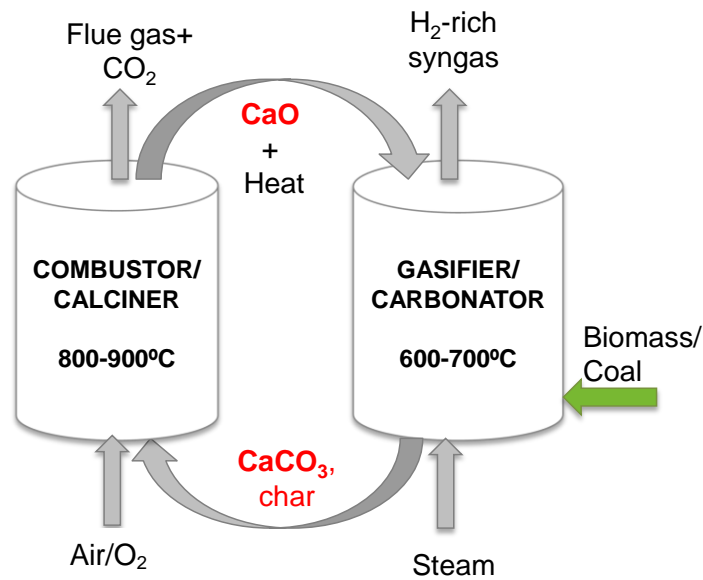
Figure 1.2: Process diagram of Gasification in Dual Fluidized Beds with in-situ CO_2 capture. (Adapted from Soukup et al. 2009)

Sorbents derived from limestone have been used to increase the hydrogen production by CO_2-adsorption for many years (Han & Harrison 1994, Pfeifer et al. 2007); however, the concept of using fluidized beds to regenerate the sorbent in a separate reactor and to provide the heat by circulation of bed material is relatively new. Grace (2011) listed the main advantages of CaO as bed material in the integrated process as follows:

(a) The heat release by the carbonation reaction inside the gasifier can be used to provide heat for the endothermic gasification;

(b) Removal of CO_2 from the gasifier shifts the chemical equilibrium, enhancing the water-gas shift reactions. As a result the production of hydrogen is increased in the gasifier; and

(c) CaO can act as catalyst for tar cracking, improving the hydrogen production and reducing the detrimental impact of tars.

Nonetheless, the success and efficiency of the process is linked to a number of factors, many of which are still under investigation. First, the cycling activity or CO_2 carrying capacity of the sorbent decreases with increasing the number of cycles, mostly attributed to the reduction of the available surface area due to sintering, and the formation of a $CaCO_3$ product layer at the surface, preventing CO_2 from being absorbed in the carbonation reaction (Salvador et al. 2003, Fennell et al. 2007). Second, limestone-derived sorbents are fragile, i.e., their mechanical stability is low, making them susceptible to attrition and leading to significant particle loss. Third, stable and continuous circulation of bed material must be assured in order to provide sufficient CaO for the carbonation reaction, as well as heat transport between the reactors.

A large number of studies have been dedicated to study the reactivity of lime-derived sorbents for CO_2 capture, mostly employing Thermogravimetric analysis (TGA) to drive the sorbent between the carbonation/calcination environments (e.g., Abanades & Alvarez, 2003, Wu et al. 2010). Efforts have also been made not only on the reversibility of the sorbent, but also on their resistance to attrition by sorbent modification, e.g., by hydration and pelletization (Kuramoto et al. 2003, Manovic, 2007, Sun et al. 2008, Yinghai et al. 2012) or by developing novel synthetic sorbents (e.g. Pacciani et al. 2008).

While it is clear that sorbents decay, and lack of reversibility are major challenges for this research area, knowledge of solids circulation rates and their effect on reactor hydrodynamics is also essential for scale-up of the process. Loss of bed material due to attrition can greatly affect solids circulation rates and hence the performance of the process. TGA experiments provide excellent insights into the kinetic performance of different sorbents and CO_2 capture, but they do not provide accurate information related to reactor design and operation. Particle attrition and hydrodynamics are highly dependent on the reactor configuration, size and operating conditions employed during tests (Blamey et al., 2010), especially in circulating fluidized beds where particles are subjected to higher mechanical stresses due to the high velocities required to recirculate large amounts of bed material.

1.4. Gas-solid Fluidized Beds

Fluidized beds have been used in many industries due to the advantages that they offer, including good heat and mass transfer, and contact between the gas and solid phases. In a fluidized bed, a gas or liquid passes upwards through a bed of particulate material at a sufficient velocity to support the solids. A fluidized bed normally requires a distributor plate that uniformly disperses the gas through a bed of solids, a vessel containing the particles, a gas-solid separator (cyclone) and a particle separation system.

1.4.1. Fluidization flow regimes

Different gas-solid fluidized bed flow regimes have been identified. Figure 1.3 shows the more relevant hydrodynamic regimes of gas-solid fluidized beds as the gas flow through the bed is increased. At very low fluid velocities (U_0), the gas passes through the interstices of a bed of particulate material without causing any particle movement. As the fluid velocity is increased, the buoyancy and drag force counterbalance the weight of the bed, leading to minimum fluidization. Bed expansion and bubbling then occur at velocities higher than the minimum fluidization velocity. Bubbling fluidization regime is characterized by the formation of bubbles within the fluidized bed that may reach a maximum stable size, improving the contacting between the gas and particles. Depending on the reactor size and particle properties, higher velocities may cause the formation of slugs (bubbles of sizes close to the diameter of the reactor) within the fluidized bed. With further velocity increments the bubbles begin to break down rather than to continue growing. This flow regime is called the turbulent regime, with transition from bubbling (or slugging) regime occurring at the point where the amplitude of pressure fluctuations reaches a maximum or where pressure fluctuations level-off when the superficial gas velocity increases (Lim et al. 1995). When the bed is in the turbulent flow regime, the elutriation of fines from the bed becomes substantial. Gas-solids separators then become essential to return the solids to the bottom of the reactor. This is called the fast fluidization regime, characterized generally by formation of a relatively dense zone of particles at the bottom of the reactor and a more dilute one at the top. Pneumatic transport occurs when the bed is fluidized at velocities significantly higher than the transport velocity at the same solids reinjection flux. The absence of a denser zone at the bottom of the reactor is the main characteristic of this flow regime, i.e., only the dilute phase is present over the entire reactor height. As seen in Figure 1.3, as the gas velocity increases, the voidage within the fluidized bed becomes higher. Thus, knowledge of axial voidage (ε) profile of a fluidized bed gives also valuable insights to understand the gas-solids flow pattern. Fast fluidization, turbulent and bubbling fluidization are the most common fluidization flow regimes utilized by industry, including for gasification and combustion applications.

Increasing U_0, ε

| Fixed bed | Bubbling Regime | Slugging Regime | Turbulent Regime | Fast Fluidization | Pneumatic Conveying |
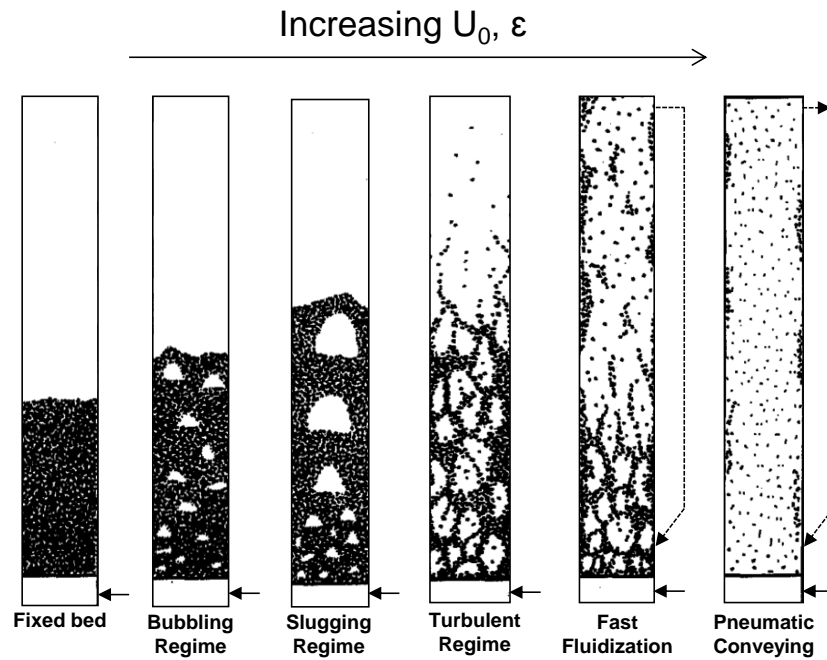
Figure 1.3: Schematic diagram of gas-solid fluidization regimes. (Adapted from Lim et al. 1995)

The main factors affecting the gas-solids flow pattern in a fluidized bed are: particle properties (density, sphericity, and diameter), gas properties (density and viscosity), reactor geometry, and the gas and solids entrance configurations. Every system requires careful understanding of the hydrodynamic behaviour so that the process can be successfully implemented for large-scale applications.

1.4.2. Powder classification

Geldart (1973) classified particles into four groups based on their density and size, as shown in Figure 1.4. Group A powders have a small size and relatively low density. When fluidized, these particles exhibit a large bed expansion before the bubbling fluidization regime is reached. Group B particles have larger diameters (~ 100-1000 µm) and densities compared to Group A particles. Unlike Group A particles, Group B particles form bubbles immediately after the minimum fluidization stage is reached. Group C particles are very small in size and their fluidization is difficult because of interparticle cohesive forces which promote channelling in the bed. The last group (Group D) represents particles of large diameter and/or high density (e.g. peas, wheat). These particles tend to form stable spouted beds when the gas is injected through a centrally positioned hole (Geldart, 1973). Often in Industry, Geldart Group A particles are used for processes involving catalytic reactions such as Fluid Catalytic Cracking (FCC); whereas, groups B and D particles are common in combustion and gasification processes.
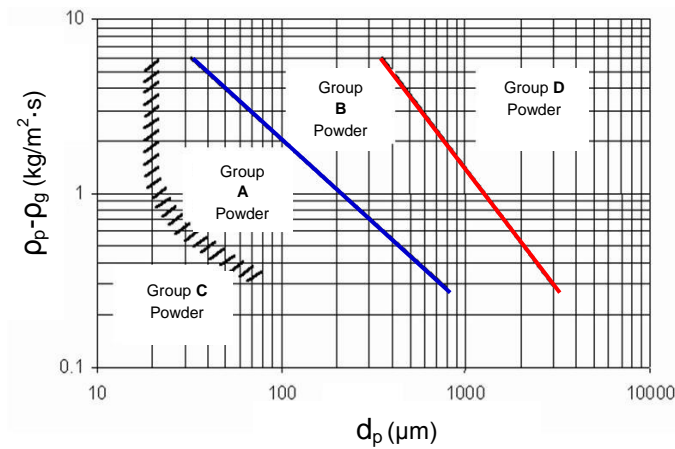
Figure 1.4: Powder classification diagram for fluidization with air at ambient conditions (Adapted from Geldart, 1973).

1.4.3. Circulating fluidized beds (CFB)

Circulating Fluidized Beds (CFBs) have been employed in industrial processes for several years. In the hydrocarbon industry, CFBs find applications in gas treatment, using dry sorbents to capture pollutants such as SO_2, and in fluid catalytic processes to refine fossil fuels. In the energy sector, CFBs are used for combustion of fossil fuels and renewable fuels. Some advantages include temperature uniformity, ability to control the retention time of solids in the bed, reduced particle agglomeration and good gas-solid contact (Grace, 1990). The main components of a CFB are a tall vessel ("riser"), a cyclone, a downcomer or standpipe, a solids control device and, in many cases, a secondary cyclone (see Figure 1.5). The gas is injected at the bottom of the riser at velocities high enough to entrain the particles from the reactor. The entrained particles are separated from the gas stream in a cyclone and subsequently returned to the bottom of the riser via a downcomer and control valve. The accumulation of particles in the downcomer builds pressure, facilitating circulation of particles around the loop.

The external solids flux in a CFB is mainly controlled by a solids control valve that can be mechanical (e.g., butterfly and slide valves) or non-mechanical (e.g., L-valve, loop-seal). The latter are commonly controlled by fluidizing particles at a bubbling fluidization state with aeration gas injected at different ports. The solids flow is controlled by adjusting the aeration flow rate. For applications requiring high temperatures, non-mechanical valves are common since they do not present erosion problems as in the case of mechanical actuators (Kim et al. 1999). Moreover, non-mechanical valves are often used in processes employing Geldart B particles because they tend to give good control of the solids flow (Knowlton, 2003).

The pressure balance around the loop (shown in Figure 1.5) plays an important role for the successful operation of a CFB. The pressure difference between the riser and downcomer sides provides the driving force to move the solids around the loop. The pressure drop across the riser, cyclone and solids control valve must be compensated by pressure gained in the return side of the loop, i.e.,

$$\Delta P_r + \Delta P_c + \Delta P_v = \Delta P_d \qquad \text{Eq. (1.2)}$$

Depending on the operating conditions, the solids suspension in the riser changes resulting in three possible fluidization regimes, dilute phase transport, fast fluidization and dense-phase transport (Lim et al. 1995).
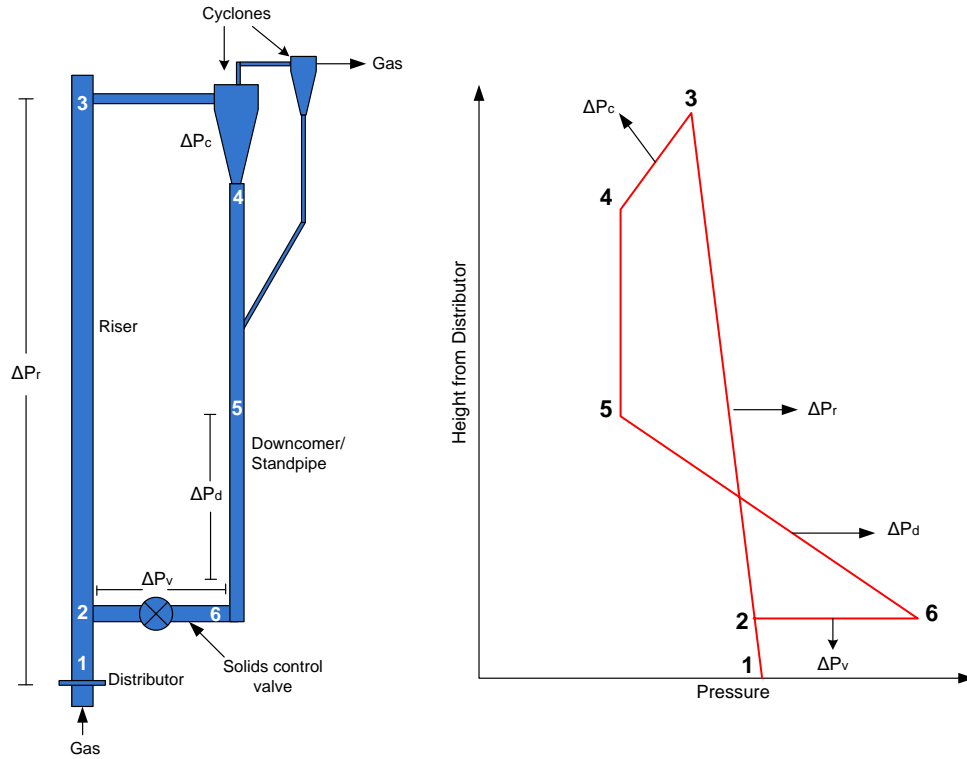
Figure 1.5: Diagram and pressure balance of a typical CFB.

CFB hydrodynamics have been studied by various authors. The relationship between the pressure balance, solids circulation rates, solids inventory and gas-flow pattern in the riser was explored by Bi & Zhu (1993). Several studies have developed hydrodynamic models to predict the gas-solids behaviour around the loop by solving the global pressure balance (e.g., Rhodes & Geldart, 1987; Lei & Horio, 1998; Kim et al. 2002). Grieco & Marmo (2008) for example, proposed a model that considers the pressure drop across different sections of the loop coupled with a model for particle entrainment. Although their model was based on empirical correlations that might not be applicable for all riser conditions, it gives an understanding of the relationship of the variables named above to CFB operation. They noted a positive effect of increased solids

inventory on the maximum achievable solids circulation rate. At a fixed superficial gas velocity in the riser and a given solids inventory, their experiments showed that increasing solids circulation flux around the loop increases the axial solids volume fraction (hold-up) in the riser. Similar experimental findings have been reported by other researchers (e.g., Kim et al. 2002).

Bi & Zhu (1993) performed an instability analysis of the operation of a CFB. They found that the solids circulation rates are strongly affected by the pressure available for solids feeding (due to the amount of solids in the downcomer and/or geometry), the opening of the solids control valve and the total solids inventory in the system. The solids circulation rates and solids density in the riser are maximized when the pressure buildup in the downcomer is sufficient to push the particles into the bottom of the riser. Likewise, careful operation of the control valve is required to attain stable and maximum solids circulation.

Apart from the factors mentioned above, the effect of other elements on the axial solids distribution in a CFB riser has been documented (e.g., Bai et al. 1992; Mastellone et al. 1999; Lackermeier et al. 2002). These factors include column dimensions and geometry (diameter, height, solids entrance and exit structure) and particle properties (mean size, density, size distribution).

1.5.Dual Fluidized Bed (DFB) Reactor Design and Configuration

Several reactor configuration modes have been proposed and investigated for calcium looping and gasification, with diverse combinations of fluidized beds and solids control valves (Löffler et al. 2003; Lu et al, 2008; Ryu et al, 2009; Soukup et al. 2009; Karmakar & Datta, 2010; Bi & Liu, 2010; Guan et al. 2010; Sung et al, 2010; Martinez et al. 2010; Charitos et al. 2010; Fang et al. 2010; Alonso et al. 2010; Schmid et al. 2011; Seo et al. 2011; Nguyen et al. 2012). As summarized by Xu et al. (2006), four different combinations of fluidized beds have been developed for Dual Fluidized Bed Gasification (DFBG) (Figure 1.6): twin Bubbling Fluidized Beds (BFB); twin circulating fluidized beds (CFB); or a CFB coupled with a BFB in the return leg (Figures 1.6c and 1.6d).
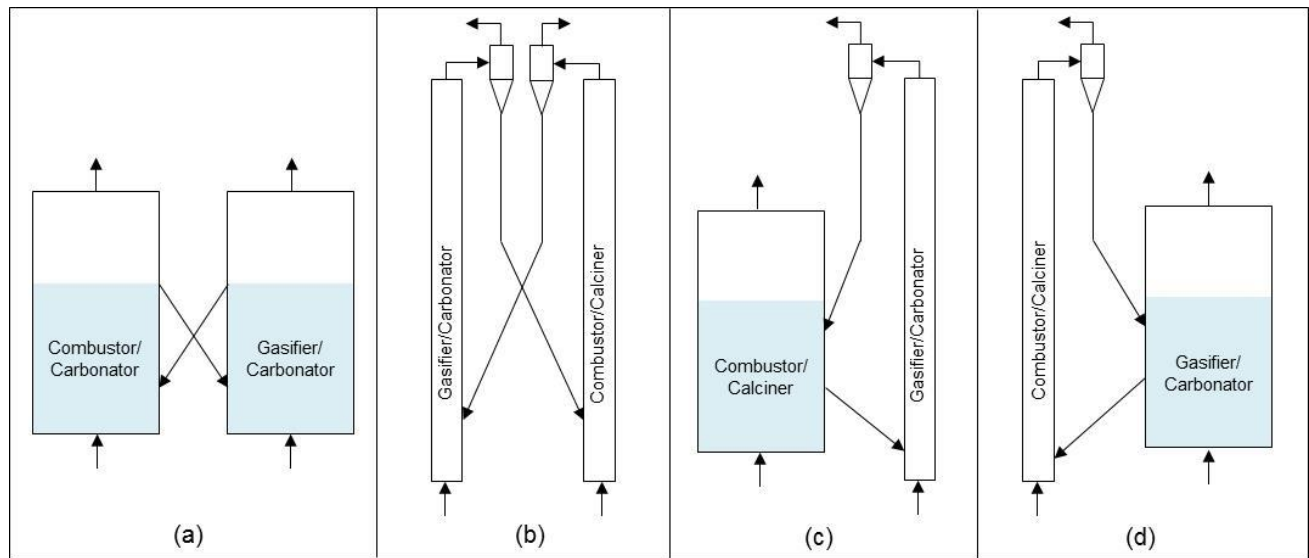
Figure 1.6: DFB reactor configurations: (a) Twin BFBs; (b) Twin CFBs; (c, d) CFB-BFB combinations (Adapted from Xu et.al., 2006)

A variety of factors influence the selection of a DFB reactor, such as the gas-solid contact required for reactions, solids residence time, required circulation between the fluidized beds, heat and mass transfer, and the amount of gas and particles to be processed. Table 1.1 shows the main qualitative hydrodynamic features offered by the single fluidized beds used in DFB reactor design. Table 1.1 indicates that, for instance, if high and continuous solid flows between the reactors are required (as in gasification/combustion processes); option (a) of Figure 1.6 is unlikely to be suitable.

Table 1.1: Fluidized bed hydrodynamic features. (Adapted from (Xu et al. 2006, and Xu, 2010).

Feature	BFB	CFB
Transport of particles	Very little	High
Solids residence time	Long	3-10 s
Particle-particle interaction	Good	Poor
Gas-solid contact	Poor	Good
Superficial gas velocity	Low	High
Total solids inventory (TSI)	High	Low
Height-to-diameter ratio (H/D)	Small	High
Particle elutriation	Low	High

1.6. DFB Hydrodynamics

As in a CFB, the operation of a DFB requires understanding of the pressure balance around the system. A number of hydrodynamic parameters, including superficial gas velocities in the reactors, particle properties and solids control valve operation (solids circulation flux), can influence the pressure balance around the loop. As stated above, in gasification systems, depending on the heat requirements when combined with CO_2 capture, the solids flux between the reactors is a very important operational parameter. Likewise, knowledge of the axial solids suspension in the riser and its dependence on operating parameters provides valuable information for reactor modeling, design and scale-up. The hydrodynamics of CFB and BFB systems have been studied separately, but relatively few studies have investigated the hydrodynamics of coupled fluidized beds. Most studies have been for cold models of big facilities. Therefore, comparing the hydrodynamics of these cold models is difficult as they vary in configuration, solids control devices and particle characteristics. Nonetheless, hydrodynamic analysis and qualitative conclusions can provide valuable insights on the global operation of a DFB and the interaction of operating parameters like gas flow rates, particle circulation, inventory of bed material, gas-solids pattern in the reactors, solids properties, and geometry.

One promising configuration for gasification integrated with CO_2 capture involves the use of a CFB and a BFB as in Figure 1.6d. This study reports on hydrodynamic studies of this type of configuration involving a CFB coupled with a BFB.

1.6.1. Effect of operating conditions

Kaiser et al. (2003) and Löffler et al. (2003) studied the hydrodynamics and stability of a gasifier using a scaled cold model composed of a riser of low H/D ratio with gas injection at three positions along the column and a BFB connected via a loop-seal at the top of the reactors, with a fluidized inclined channel connecting the gasification reactor with the combustion zone. The effects of riser fluidization, solids inventory and geometry of the connection pipe between the vessels on the overall solids circulation rates and riser gas-flow pattern were investigated. The solids circulation rate was found to be strongly affected by the inclination of the connection pipe between the gasification and the combustion zones, the total solids inventory, and the flow of air into the bottom of the riser reactor. Injection of gas at higher points in the riser decreased the axial solids distribution negatively affecting the total solids flow.

These experimental findings regarding the effect of riser bottom air on the solids circulation rates and solids holdup are in agreement with those performed in a DFB of similar geometry (Karmakar & Datta, 2010). These authors also investigated the effect of aeration flow to their two non-mechanical valves, and the effect of particle size. Their results indicated that solids circulation rates are enhanced by increasing the aeration flow in the L-valve, increasing the pressure drop across the downcomer, as noted by Kim et al. (1999), and

reducing the particle size, while increasing the particle concentration in the riser. The same effect of the aeration flow on the solids circulation flux was reported by Sung et al. (2010) and Nguyen et al. (2011), who also found a less noticeable effect of the riser superficial gas velocity, suggesting that the aeration flow is the most important parameter in controlling the solids flux. Guan et al. (2010) reported that the solids circulation flux decreased with increasing particle size.

Charitos et al. (2010) reported on the hydrodynamics of a scaled cold model of a carbonate looping cycle facility. A riser and a BFB were again employed, with the reactors interconnected via loop-seals at the top and bottom. The loop-seal at the top was divided into two outlets so that particles leaving the riser returned to the bottom section to increase the solids holdup. The solids circulation between the reactors was controlled by varying the opening orifice of a cone valve. In this study, the authors studied the effect of varying the aperture of the cone valve, Total Solids Inventory (TSI), particle size, outlet pressure of the BFB and gas flow rate in the riser on the global circulation rates and riser hydrodynamics. As in previous studies, they found that these parameters determined the distribution of solids in the DFBs. The strong effect observed by other investigators of increasing of solids circulation rates with increasing riser superficial gas velocity was also exhibited. Unlike previous investigations, the authors did not find a strong effect of TSI on solids holdup at the top of the riser or on the solids circulation flux.

The solids circulation flux has also found to be affected by the bed height in the BFB. As in a normal CFB, where the solids flux is influenced by the height of solids in the downcomer, Guan et al. (2010) reported an increase in solids flux when the bed inventory on the BFB side was high, which is in turn related to the system TSI.

The effect of superficial gas velocity in the BFB has been documented in the literature. Kaiser et al. (2003) found a negligible effect of superficial gas velocity in the BFB on the solids flux. Kehlenbeck et al. (2001), Seo et al. (2011) and reported that the solids circulation rates are not a function of the fluidization in the BFB at gas flows higher than required for minimum fluidization. This is because at velocities higher than the minimum fluidization velocity, the pressure drop in the BFB becomes virtually constant, resulting in a constant solids conveying through the overflow pipe connected to the loop-seal, with no further effect on the solids circulation rate.

1.6.2. Pressure balance

As in a CFB, the pressure balance around the loop is important to achieve stable operation. Analysis of the pressure drop in different sections of the loop provides information on how the bed material is distributed around the system and how the operating conditions are related to the pressure profiles. Several authors have analyzed the pressure profile around the loop of a CFB-BFB (Kaiser et al. 2003; Charitos et al. 2010;

Karmakar & Datta, 2010). Numerical models solving the pressure balance of particular reactors have been developed to predict the solids circulation flux. However, the operability analysis and measurement of pressure profiles have been limited to relatively narrow operating conditions (low gas velocities and circulation flux) and small units (reactor height). There is a need for useful information on the operation of a DFB at higher solids circulation fluxes in tall beds.

1.7. Gas Leakage in DFB Reactors

A major potential disadvantage when combining fluidized beds is unintentional slippage of gas from one side to the other. When this occurs, the product gas quality deteriorates resulting in economic losses for the process.

Gas leakage is of particular importance in this study because in gasification with integrated CO_2 capture, gas bypassing would result in the reduction of hydrogen content in the syngas and dilution of CO_2 produced in the calciner/combustor. Thus, gas leakage must be minimized. Knowledge of the gas leakage between the reactors is needed to help optimize the reactor configuration of DFB systems.

Measurements of gas leakage between the zones of DFBs comprising CFB-BFB combinations are scarce. Johansson et al. (2003) performed DFB experiments to determine gas leakage. They found that approximately 2.0% of the product gas from the BFB left the system through the cyclone of the riser and 2.0-12.0% of the aeration flow in a particle sealpot leaked to the BFB. In the same study, no gas leakage from the riser to the BFB side was found. Xu, (2010), on the other hand, reported 0.8-3.0% gas leakages from the BFB to the riser depending on the pressure drop through the loop-seal connecting the reactors. These authors found no slippage of gas from the BFB to the cyclone of the riser and negligible gas leakage from the riser to the BFB.

The gas leakage has been found to be dependent on the distribution bed material in the system (Kronberger et.al. 2004), and on the solids circulation between the reactors. (Xu, 2010) Thus, improved knowledge of gas leakage is important for the design of DFB systems.

1.8. DFB Scale-up

Successful operation of a new fluidized bed reactor depends on the gas-solid dynamic behaviour. Thus, when designing a new process, it is desirable to know the quality of the hydrodynamics. Unfortunately, accurately predicting the hydrodynamics in real processes is very difficult; therefore, a cold model becomes very useful to simulate the hydrodynamics of commercial systems. Authors have proposed different scaling parameters that must be matched between the fluidized beds (e.g. Horio, 1989; Glicksman, 1994; Meer et al. 1999). The most widely used scaling laws are those proposed by Glicksman (1984), derived by non-dimensionalizing the

governing equations of motion for the fluid and solids phases and the boundary conditions. In addition to geometric similarity, the full set of scaling parameters to be matched is:

$$\frac{\rho_g \rho_p d_p^3 g}{\mu^2}, \frac{U_0^2}{gD}, \frac{\rho_g U_0 D}{\mu}, \frac{\rho_p}{\rho_g}, \frac{G_s}{\rho_p U_0}, \frac{L}{D}, \text{ bed geometry, } \emptyset, \text{ Particle Size Distribution (PSD)} \qquad (1.3)$$

The above scaling groups exclude interparticle forces due to phenomena like electrostatics and cohesive forces. However, as pointed out by Glicksman (1984), interparticle forces should be taken into account when fine particles are employed.

Glicksman (1984), proposed a simplified form of the dimensionless parameters to increase the degrees of freedom when designing a scale model. When the flow is viscous or inertial dominated, the full set of the scaling parameters to be matched can be reduced to:

Viscous limit
$$\frac{\rho_p^2 d_p^3 g}{\mu^2}, \frac{U_0^2}{gD}, \frac{G_s}{\rho_p U_0}, \frac{L}{D}, \text{ bed geometry, } \emptyset, \text{ PSD} \qquad (1.4)$$

Inertial limit
$$\frac{U_0^2}{gD}, \frac{\rho_p}{\rho_g}, \frac{G_s}{\rho_p U_0}, \frac{L}{D}, \text{ bed geometry, } \emptyset, \text{ PSD} \qquad (1.5)$$

For viscous limited flow (low Reynolds number) the ratio of the inertial forces between solids and gas is neglected. At high Reynolds number, where the fluid is mostly dominated by inertial forces, the contribution of gas viscosity to the bed dynamics is minimal, so viscous stresses are neglected.

In practice, matching all the dimensionless parameters, either in the reduced or complete form, is difficult, leading commonly to different dynamic behaviours between scaled units and full-scale fluidized bed. To achieve hydrodynamic similarity between a cold model and the prototype, not only the geometry must be matched, but also all the other dimensionless parameters in Eq. 1.3. Cold flow models usually operate at ambient temperature and pressure. To compare the hydrodynamics of processes operating at high temperature with that of the cold model, particles of very different density must be used in both facilities to satisfy the ratio of inertial forces (solids-to-gas densities). This in turn demands a different particle size and superficial gas velocity to match the other dimensionless parameters. Sometimes the difference in particle size between the cold model and the real process is so great that the cold model could end up using a bed material of a different Geldart's classification with different fluidization behaviour (Knowlton et al. 2005). Furthermore, the use of a different bed material in the cold model may result in different particle sphericity, again affecting the

hydrodynamic behaviour. Thus, it would be of great advantage to maintain identical particles between the two models to achieve dynamic similarity and account for interparticle forces.

Verification of the scaling laws remains a subject of great importance for fluidized beds. Many experiments have been performed to test the full set or simplified form of the scaling laws in bubbling and circulating fluidized beds, as summarized by Glicksman (1994). However, the scaling laws for dual fluidized beds involving a riser and a BFB have not yet been verified.

There have been a number of studies reporting on the design of cold models to simulate the hydrodynamics of large facilities based on the simplified form of the scaling laws (e.g. Kaiser et al. 2003; Charitos et al. 2010; Martínez et al. 2010). Nonetheless, the set of dimensionless parameters could not be fully matched in these cases, leading to lack of full similarity of the hydrodynamics of the facilities. In addition, these cold models have differed considerably in size from the big facility, making comparison even more complicated if phenomena related to wall effects are present (Charitos et al. 2010).

Generally, cold flow models in DFB have been designed to solve operational problems or to optimize existing plants. Therefore, the analysis or verification of dimensionless parameters governing the hydrodynamics of DFB is still a major focus for scale-up of processes involving this type of reactor. One possible way to do this is by carrying out experiments in models of identical size and particle characteristics, where the key gas properties (μ, ρ_g) can be altered to evaluate the effect of viscous and inertial drag forces on the hydrodynamics.

1.9. Summary

Based on the literature background presented above, the following conclusions can be drawn:

- The integration of the calcium looping cycle and the gasification in dual fluidized beds is a promising emerging technology to reduce/control CO_2 emissions.
- Limestone-derived sorbents are a promising option to capture CO_2 due to the variety of advantages that they offer to the gasification reactions and to the economics of the process. Hydrodynamic experiments performed to date on calcium looping and gasification have been based on scaled cold models of larger facilities with particle characteristics differing from those in the real plant. It is necessary to investigate the fluidization behavior of sorbents that are likely to be used in a real plant. Dual fluidized beds coupling a CFB and a BFB is a promising configuration for gasification with in-situ CO_2 capture.
- Although some studies have reported on the relationship between operating parameters and hydrodynamics, more experimental information is needed to fully understand the performance of a

DFB operating high solids circulation flux. Hydrodynamics depend on scale and reactor configuration.

- Knowledge of gas leakage between the coupled fluidized beds is needed to design and improve the operation and/or reactor configuration of dual beds.

- The scaling laws have been employed to design cold models of large facilities. Several studies have been carried out to verify the scaling laws for CFB and BFB. However, little information is available in literature regarding the hydrodynamic behaviour of a DFB when the scaling laws are applied to scale-up. Due to lack of hydrodynamic comparability between a cold model and a real plant, it is still necessary to study effects of scale on DFB hydrodynamics.

1.10. Research Objectives

The primary objective of the present research is to characterize the hydrodynamic behaviour of limestone particles at room and elevated temperatures in a DFB comprised of a riser, a BFB and a loop-seal for particle circulation. The experiments are performed for a fixed solids inventory, given initial PSD and constant fluidization velocity in the BFB. The analysis of the overall performance of the looping system will be analyzed with the following objectives:

- To measure the solids circulation rates under different aeration flows in the loop-seal connecting the BFB and the riser and superficial gas velocity in the riser.

- To find the effect of operating conditions (superficial gas velocity and solids circulation flux) on the axial distribution of solids in the riser and the overall pressure profile around the loop.

- To study the stability of the system with increasing solids circulation fluxes.

- To operate the DFB at different temperatures to find the effect of scaling parameters on the gas-solid behaviour in the riser, pressure profiles and solids mass flux.

- To measure the gas leakage between the BFB and the riser for different operating conditions, including superficial gas velocities, solids circulation rates and temperatures.

Chapter 2: Experimental Setup and Methods

This chapter describes the Dual Fluidized Bed (DFB) facility used for this work, as well as the process description and the techniques employed for data acquisition.

2.1. Dual Fluidized Bed System

A schematic diagram of the experimental setup is shown in Figure 2.1. It consists of DFB components made of stainless steel that include a vertical riser (0.041 m i.d., height = 6.0 m) interconnected via a 0.041 m diameter loop-seal to a Bubbling Fluidized Bed (BFB) (0.13 m i.d. (dense bed region), height = 2.0 m (including freeboard)). Both riser and BFB employ a perforated plate as the gas distributor (additional details on perforated plates can be found in Appendix E). The hot unit was built based on results obtained by Xu (2010), and it is available for use at the Clean Energy Research Centre (CERC).

In the BFB, particles are fluidized with superficial air velocities above the minimum fluidization velocity. Two internal cyclones (connected in parallel) in the BFB freeboard separate the entrained particles from the gas and return them to the dense phase. The particulate material then travels from the BFB to the riser via the loop-seal, which not only controls the solid circulation between the columns, but also is intended to prevent gas exchange between the two vessels. In the loop-seal, particles are fluidized at the bottom and horizontal sections with $U_a \geq U_{mf}$. Subsequently, particles are transferred to the riser where gas is injected at the bottom at high velocities. The fluidizing gas entrains the particles from the reactor to a primary cyclone located at the exit which separates particles from the gas stream. A high efficiency primary cyclone returns most of the particles to the BFB via a return leg or downcomer (0.041 m diameter) completing the looping cycle. A high efficiency secondary cyclone, located after the primary cyclone, separates fines not captured by the primary cyclone. The outgoing gas is filtered to remove any elutriated fines and to allow a clean exhaust gas. The exhaust gas is subsequently extracted by the building ventilation system. The fine particles separated by the secondary cyclone are returned to the BFB via a dipleg (0.013 m diameter), as shown in Figure 2.1. A Standard Operating Procedure (SOP) of the facility has been prepared (Reyes-Ramirez, 2012).

The unit is operated at atmospheric pressure. Some experiments were carried out at elevated temperatures (up to 250°C). Compressed air from the building air supply was the fluidizing agent for all experiments. As shown in Figure 2.2, air was distributed between the column inlets and the vertical and horizontal sections of the loop-seal. Two mass flow meters previously calibrated for nitrogen were used to measure the gas flow rate to the reactors, whereas the flow rate to the loop-seal was measured by two rotameters from *Omega Engineering Inc.* and controlled by internal gate valves. In order to assess the effect of temperature on the hydrodynamics,

the total flow rates to the columns were adjusted at each operating temperature to maintain the same superficial gas velocities.

This experimental study encompassed different riser superficial gas velocities, loop-seal aeration flow rates and temperatures. The ranges of each of these operating variables and particle characteristics are provided in Table 2.1.

Table 2.1: Ranges of experimental operating conditions.

Variable	Range	Units
Riser superficial gas velocity (U_r)	2.5 - 6.5	m/s
BFB superficial gas velocity (U_{BFB})	0.24	m/s
Aeration velocity in loop-seal (U_a/U_{mf})	1 - 7	-----
Solids inventory (*TSI*)	12	kg
Temperatures	25, 80, 250	ºC
Solids circulation flux (G_s)	25-139	kg/m^2·s
Particle density (ρ_p)	2870	kg/m^3
Bulk density (ρ_b)	1364	kg/m^3
Surface-volume mean particle diameter (d_p)	438	μm
Particle size distribution (*PSD*)	212-1180	μm
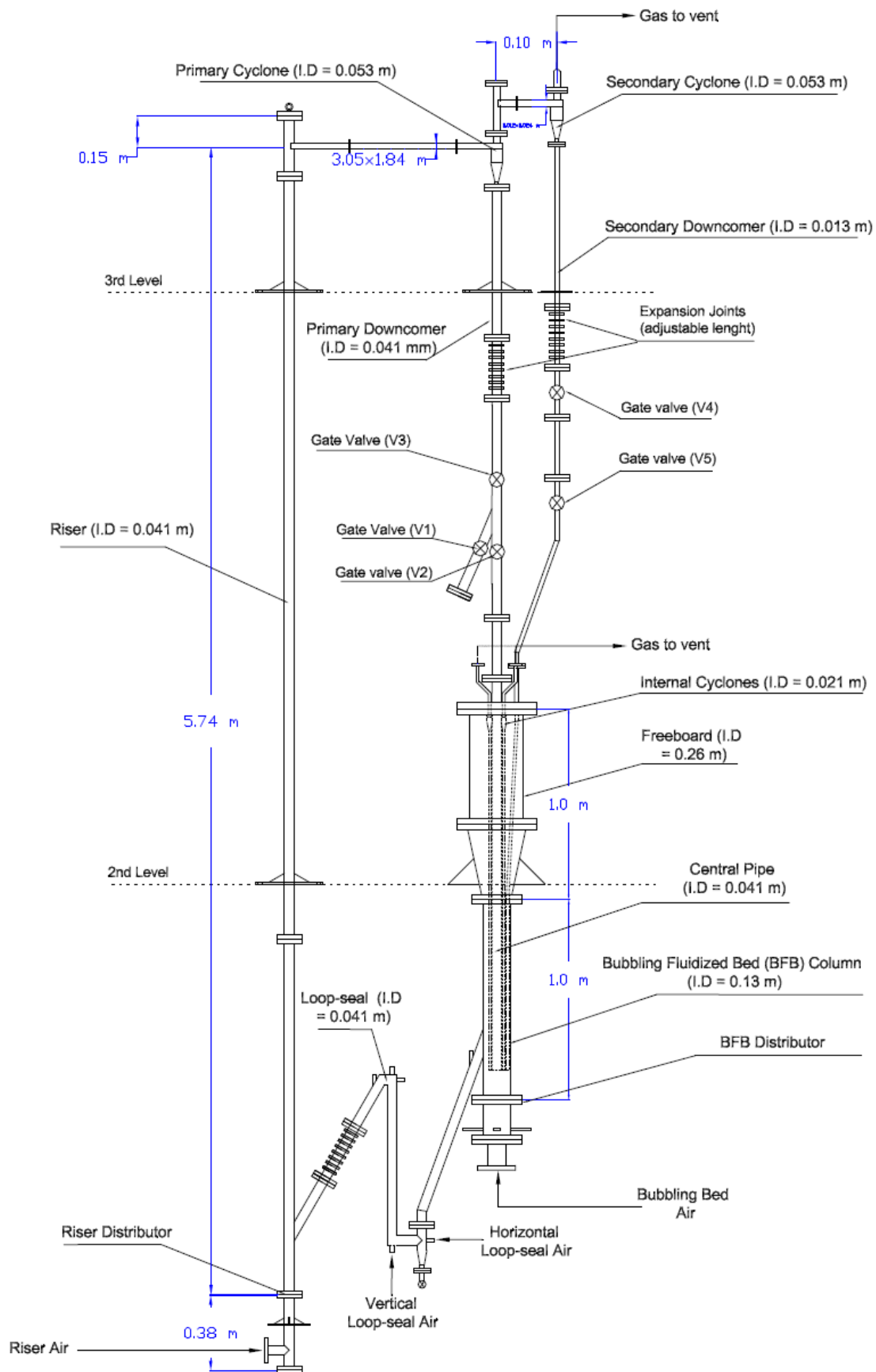
Figure 2.1: Schematics of Dual Fluidized Bed (DFB) facility at UBC.
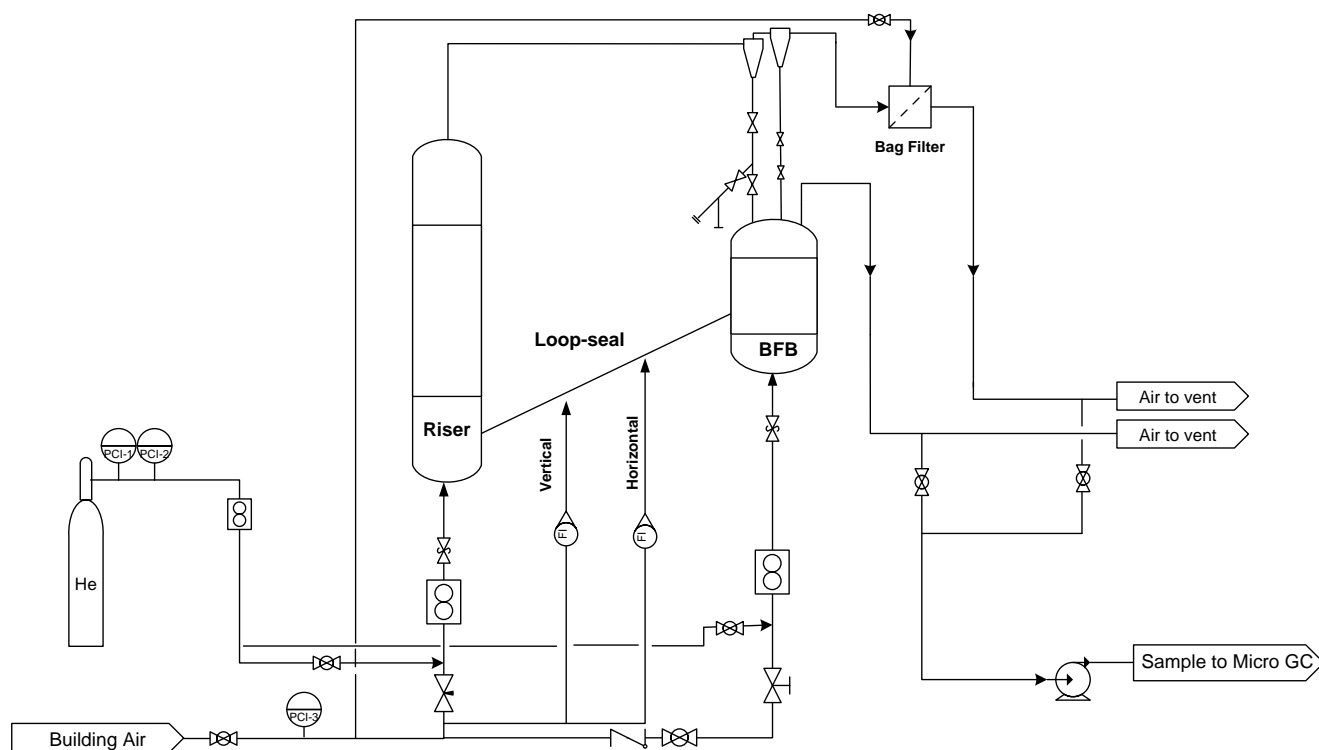
Figure 2.2: Flow diagram of Dual Fluidized Bed (DFB). A detailed PDF can be found in the operating report (Reyes-Ramirez, 2012)

2.2. Measurement Techniques

2.2.1. Bed material characterization

Cadomin limestone particles from Alberta provided by *Lehigh Cement Company* were used as the bed material for all experiments. These particles were crushed and classified to 212-1180 μm size. A *Mastersizer2000* measured the initial Particle Size Distribution (PSD) used for the experimental runs (see Figure 2.3). The measured surface-volume mean particle diameter was 438 μm. The skeletal density of particles (2870 kg/m^3) and the bulk density (1364 kg/m^3) were measured by a gas pycnometer provided by *Quantachrome Instruments* and by a graduated cylinder, respectively. A total mass of 12 kg of bed material was initially loaded into the looping system for the experiments. Based on the density difference between particles and fluidizing gas, and its mean particle diameter, the limestone belongs to Group B in the Geldart (1973) classification of fluidizable powders.
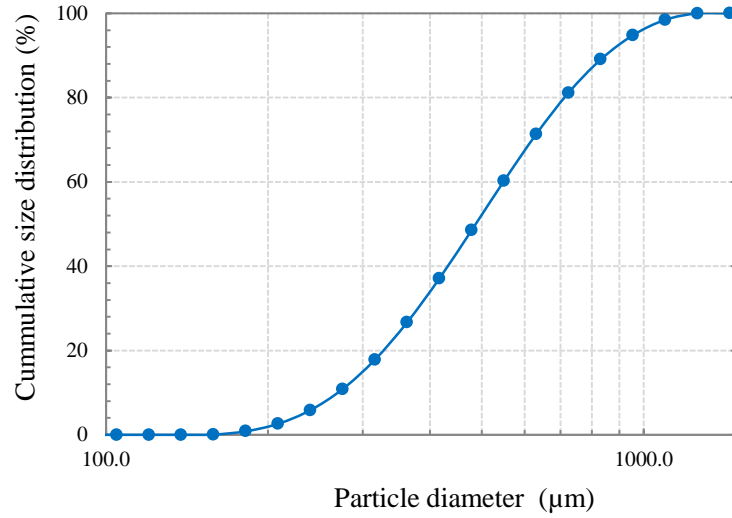
Figure 2.3: Particle size distribution of Cadomin Limestone.

2.2.2. Minimum fluidization velocity of particulate material

The minimum fluidization velocity (U_{mf}) of powders is commonly estimated based on correlations from literature. The application of these correlations in this study may lead to uncertainties, since most of them have been derived at ambient conditions with particles of variable characteristics, such as the shape factor, which can greatly affect U_{mf}. Therefore, the minimum fluidization velocity of limestone particles in this investigation was determined both experimentally and by empirical correlation. The former was carried out in a two-dimensional column made of acrylic. The volumetric flow of air through the unit and the bed pressure drop were measured by a mass flow meter and a differential pressure transducer from Omega, respectively. The unit was vigorously fluidized before the experiment to remove internal stresses and agglomeration due to filling. Pressure drops were measured in both the fluidization and de-fluidization states. The minimum fluidization velocity of limestone (0.11 m/s) was determined from a plot of bed pressure drop vs. superficial gas velocity (Figure 2.4).

In addition, U_{mf} was predicted by equating the Ergun equation to the pressure drop of the bed at the minimum fluidization state (Yang, 2003). The resulting expression correlates the Archimedes number to the Reynolds number at minimum fluidization as follows:

$$Ar = 150 \frac{(1 - \varepsilon_{mf})}{\emptyset^2 \varepsilon_{mf}^3} Re_{mf} + 1.75 \frac{1}{\emptyset \varepsilon_{mf}^3} Re_{mf}^2 \tag{2.1}$$

with ε_{mf} estimated from

$$\frac{1}{\emptyset \varepsilon_{mf}^3} \approx 14 \tag{2.2}$$

and particle sphericity, $\emptyset = 0.6$ (Jia et al., 2007). Table 2.2 reports the calculated values of minimum fluidization velocities at room and elevated temperature. The discrepancy between theoretical and experimental values could be attributed to wall effects occurring in the 2D-column, as well as particle segregation caused by the large particle size distribution used in this study. To ensure complete fluidization, the predicted U_{mf}, i.e., the higher U_{mf} value, was used to calculate U_a and U_{BFB} for the experiments in this study.
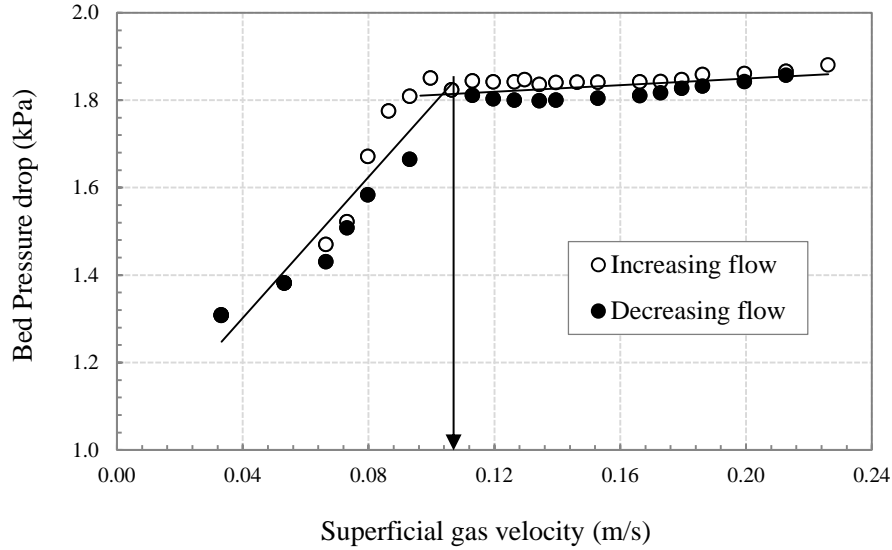
Figure 2.4: Experimental determination of U_{mf} from bed pressure drop vs. superficial gas velocity. Bed material: Limestone, 23°C.

Table 2.2: Predicted and experimental values of minimum fluidization velocity at room temperature.

Temperature (°C)	Theoretical U_{mf} [Wen & Yu] (m/s)	Experimental U_{mf} (m/s)	Deviation (%)
23	0.15	0.11	32.4
80	0.14	**	**
250	0.11	**	**

**Not determined

2.2.3. Solid circulation flux

A solids diversion method was chosen as the technique to measure the solids circulation rate between the fluidized beds. A bypass line of 0.041 m diameter and two gate valves were installed on the return leg of the primary cyclone (Figure 2.5). After reaching the steady state operation, *valves* V1 and V2 were opened and closed, respectively, for no more than 12 seconds allowing the solids to be diverted to the bypass line. Particles were then collected in a receiver, 0.018 m^3 container made of stainless steel. The resulting solids circulation flux was subsequently calculated based on the weight of particles collected (ranging from 0.02 to 1.3 kg), the time of collection and the riser cross-sectional area. A high-temperature filter bag was attached to the outlet of the bypass line so that most of the fines leaving the system were retained and diverted into the container. The accuracy of this technique depends on the validity of the assumptions that all of the entrained particles are captured by the primary cyclone and returned to the bubbling fluidized bed, and that the system pressure balance is not greatly influenced by the solids diversion. In addition, the successful application of this technique to measure the solids mass flux between the reactors also depends on the accuracy of the diversion time.

In order to minimize errors due to changes in total solid inventory, the extracted solids were returned to the system immediately after every solid circulation flux measurement through a solids return device mounted at the top of the primary cyclone.
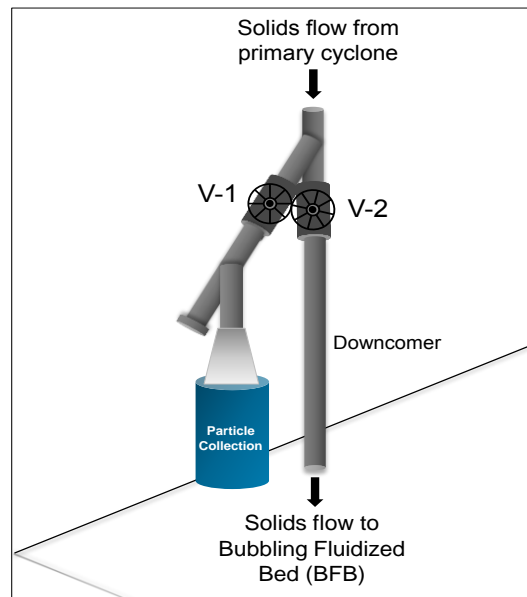
Figure 2.5: Set-up for determination of solids circulation flux.

2.2.4. Gas leakage

A helium gas-tracer technique was used to investigate gas leakage between the interconnected reactors. Helium was added at the inlet of the riser and or the BFB inlet, with less than 3.0% molar concentrations, in order to not affect the hydrodynamics. Helium injection was performed via a mass flow controller previously calibrated for this gas by the supplier (*Omega Engineering Inc.*). The concentration of helium was measured in different sections of the facility using a *Varian CP-4900* micro Gas Chromatograph (GC) capable of detecting concentrations as low as 100 ppm. The micro GC was initially calibrated using mixtures of helium and compressed air (Appendix B). A helium mass balance led to the determination of extent of gas leakage between the two vessels.

2.2.5. Pressure and temperature

Local pressures in the DFB system were measured by a series of pressure transducers from Omega Engineering (PX164 and PX142 series). These transducers were connected to pressure taps fitted along the vessels, downcomers and loop-seal. A 10 μm stainless steel mesh was placed on the fitting-end of each port to prevent powder from invading the differential pressure lines. Both differential and gauge pressures were measured, depending on the location, as shown in Figure 2.6. Voltage signals from the transducers were collected at a sampling frequency of 100 Hz during 10-15 min intervals after steady-state was reached. Signals were then sent to a computer via a data acquisition (DAQ) board and converted to pressure and temperature signals using *LabVIEW* software. Pressure transducers were calibrated prior to the measurements using a water manometer. The corresponding calibration curves and detailed explanations are given in Appendix B.

For the higher temperature runs, the DFB system was heated by a series of semi-cylindrical and coil ceramic heaters attached to the external surface of the reactors, as indicated in Figure 2.7. To minimize heat loss, these ceramic heaters were also wrapped in a two-inch (51 mm) layer of *FiberFrax* blanket insulation, held in place by 1/8-inch (3.2 mm) thick aluminum panels. Five thermocouples on the surface of the heaters were electrically connected to controllers to adjust the temperature in the two columns. In addition, K-type thermocouples were immersed in the cold model reactors to measure the temperatures in the beds and at other locations around the loop (see Figure 2.6). Temperature control was achieved by an on/off control strategy.

Table 2.3: Pressure measurements and transducer range specifications

Pressure port	Pressure measurement	Pressure range [psi]
P2-P6, P23	differential	0-1
P7-P14	differential	0-0.36
P20-P22	differential	0-0.36
P24	differential	0-5
P27	differential	0-30
P1, P15-P19, P28-P30, P32-P33	gauge	0-15
P25, P26	gauge	0-30
P26, P31	gauge	0-30
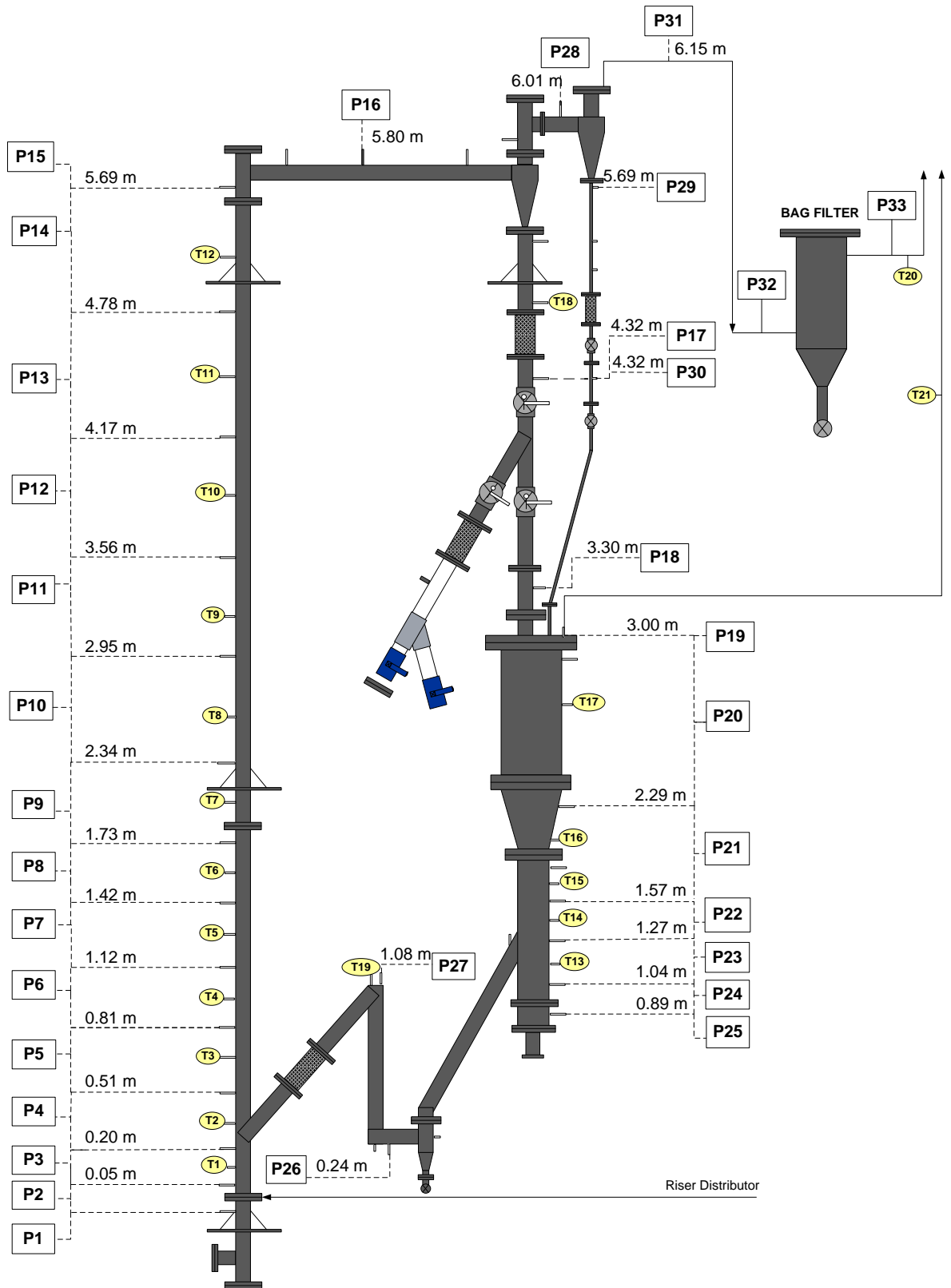
Figure 2.6: Locations of pressure transducers (P) and thermocouples (T) in looping system. Reference level for all heights is top of riser distributor. All pressure ports are flush with column wall or pipe wall. Thermocouples are all at centreline.

Figure 2.7: Location of heaters and their specifications.
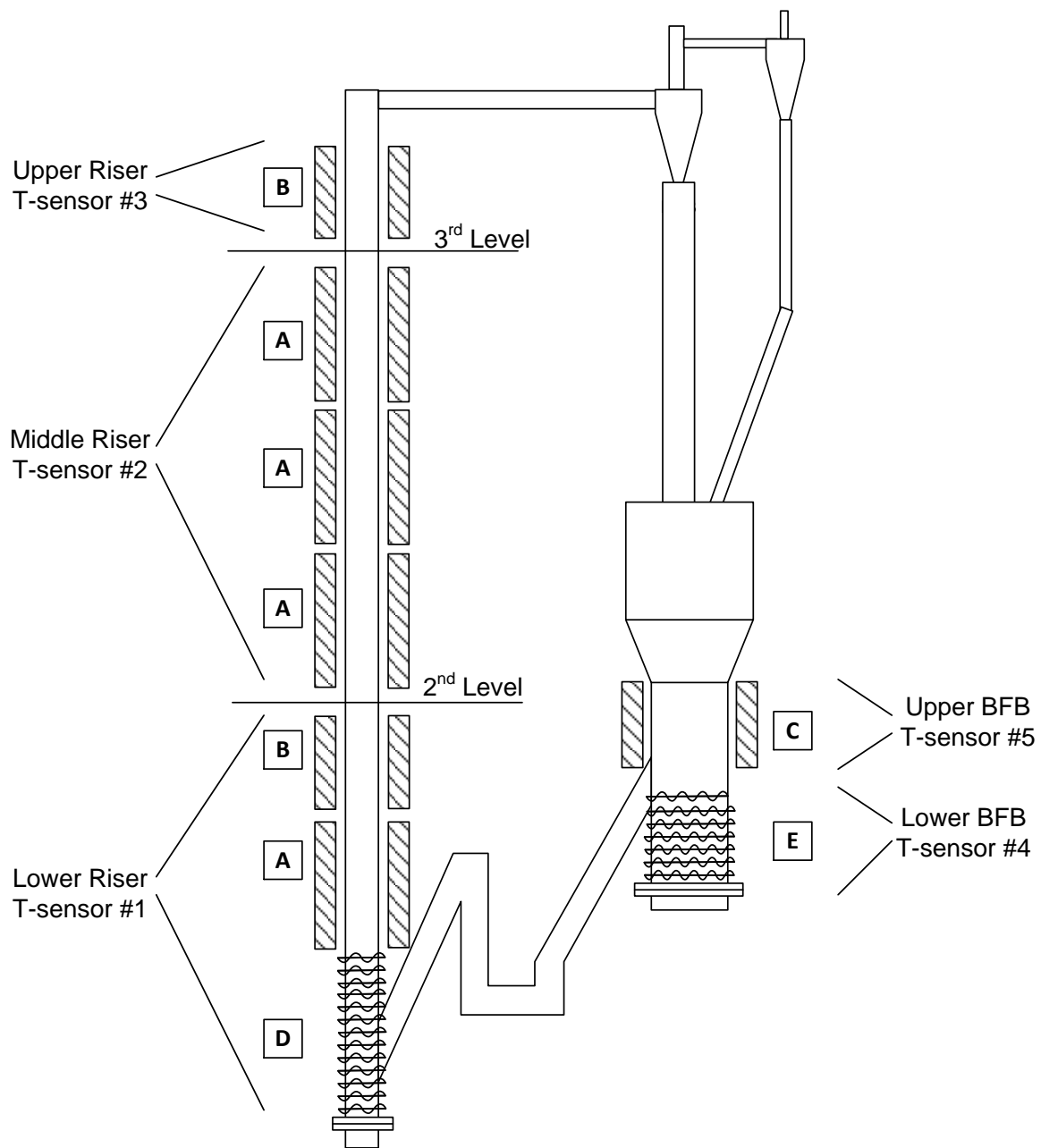
HEATER TYPE	DESCRIPTION	LENGTH*	MAX. POWER
A	Semi-cylindrical ceramic fibre	0.61 m	1100 W
B	Semi-cylindrical ceramic fibre	0.46 m	750 W
C	Semi-cylindrical ceramic fibre	0.61 m	3000 W
D	Resistance wire with ceramic beads coiled around pipe	0.52 m	3600 W
E	Resistance wire with ceramic beads coiled around pipe	0.40 m	4800 W

*For heaters D and E, length is the height of the heater along the pipe

2.2.6. Apparent solids concentration in riser reactor

Apparent solids concentrations in the riser were estimated based on total pressure drops. The total pressure drop in a vertical pneumatic transport pipe is dictated by the static head or weight of particles, the pressure drop due to particle acceleration and the pressure drop due to friction between particle-gas and particle-reactor wall (Lim et al. 1995; Bidwe et al. 2011). For simplicity in the determination of the total pressure drop, and in dilute systems (as in the case of risers with an absence of a dense phase zone), the pressure drops due to friction and acceleration are commonly neglected (Lim et al. 1995). Neglecting these terms, we can infer the average apparent solids concentration from the time-average pressure drop across different sections in the reactor. Thus, the average solids concentration can be estimated from the static pressure drop by means of

$$-\frac{\Delta P}{\Delta H} = \left[\rho_s \varepsilon_p + \rho_g (1 - \varepsilon_p)\right] g \tag{2.3}$$

where $\frac{\Delta P}{\Delta H}$ is the time-average static pressure drop over a vertical section of the reactor, ε_p is the average solids holdup, and ρ_p and ρ_g are the solids and fluid densities, respectively.

Chapter 3: Hydrodynamic Study of a Dual Fluidized Bed Containing Limestone Particles

This chapter presents the hydrodynamic behaviour of limestone particles at room temperature. The effects of gas flow rates in the riser and loop-seal on the solids circulation flux, axial solids distribution in the riser and pressure balance around the loop are determined and analyzed. Further in this chapter, gas leakage between the reactors is presented as a function of the operating conditions.

As mentioned in Chapter 1, the superficial gas velocity in a BFB has been found to not significantly affect the solids circulation flux in a DFB. Therefore, the experimental study was performed with a constant BFB superficial gas velocity (U_{BFB}) of 0.24 m/s ($1.7U_{mf}$). Likewise, the system used in the present chapter operated with a fixed initial inventory of crushed limestone of 12 kg.

3.1. Measurement of Solids Circulation Flux

The solids circulation flux was measured according to the methodology explained in Chapter 2. The flow of solids was collected once the system achieved a steady-state at the pre-set operating conditions. Steady-state was deemed to have been attained when the standard deviation of the pressure drops in the system, i.e., across the riser, BFB and loop-seal, did not change by more than 10% in ten minutes, indicating a constant flow of particles around the loop. Three to seven measurements were recorded for every set of experimental conditions to increase the level of reliability.

3.1.1. Effect of aeration velocity in loop-seal, U_a, on solids flux, G_s

As discussed in Section 1.1.1, in a circulating fluidized bed the solids mass flux around the system is determined by the gas injection flow rate at the bottom of the non-mechanical valve, which provides the momentum necessary to carry the particles from one side to the other. In this case, the flow rate in the loop-seal was varied in order to find a relationship between U_a and G_s. Figure 3.1 shows the influence of total gas velocity in the loop-seal (U_a) (varying from 0 to $7U_{mf}$) on the circulation flux ,G_s, at a fixed superficial gas velocities in the riser U_r = 2.5 m/s, and the BFB, U_{BFB} = 0.24 m/s. As expected, G_s increased with increasing loop-seal aeration velocity. When no air was supplied to the loop-seal (U_a=0 m/s), G_s was only 0.16 kg/m^2·s, indicating the absence of solids transport from the riser to the BFB for this operating condition. Figure 3.1 shows that G_s increased from 5.2 kg/m^2·s to 34 kg/m^2·s as the flow rate in the loop-seal was raised to $7U_{mf}$. However, augmenting U_a from $5U_{mf}$ to $7U_{mf}$ did not significantly influence G_s, resulting in small increment of only 4 kg/m^2·s. This is because at fixed superficial gas velocity in the riser and solids inventory, there is a

maximum solids circulation flux that the gas is able to provide in the reactor. At $U_a \geq 5U_{mf}$, the pressure drop in the reactor increases which causes a reduction in pressure head of solids on the right hand side of the loop (as seen in Figure 2.1). This at the same time decreases the solids circulation around the system.
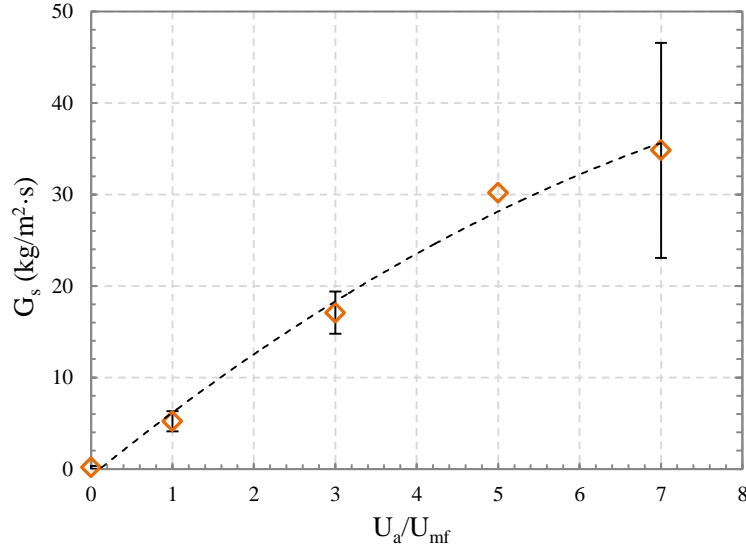
Figure 3.1: Effect of aeration velocity on solids circulation flux between riser and BFB. U_r=2.5 m/s. Error bars correspond to standard error of measurements.

3.1.2. Influence of riser superficial gas velocity on G_s

In a CFB, the fluidization velocity in the riser (U_r) can influence the solids mass flux around the system for a pre-set aeration flow rate. The effect of U_r (from 2.5 to 6.5 m/s) on the solids mass flux (G_s) at different aeration velocities (U_a) is shown in Figure 3.2. As can be seen, G_s increased from 0.16 to 118 kg/ m²·s when U_r was increased from 2.5 to 5.0 m/s at different aeration velocities (U_a). The rate of change in G_s increased at higher aeration velocities (U_a) because increasing U_r increases the drag force on the particle surface. Thus, any increment of U_r increases the drag force causing more particles to move upward and be entrained from the reactor, resulting in an increase in G_s. However, G_s was not greatly affected by U_r when $U_r > 5.0$ m/s.
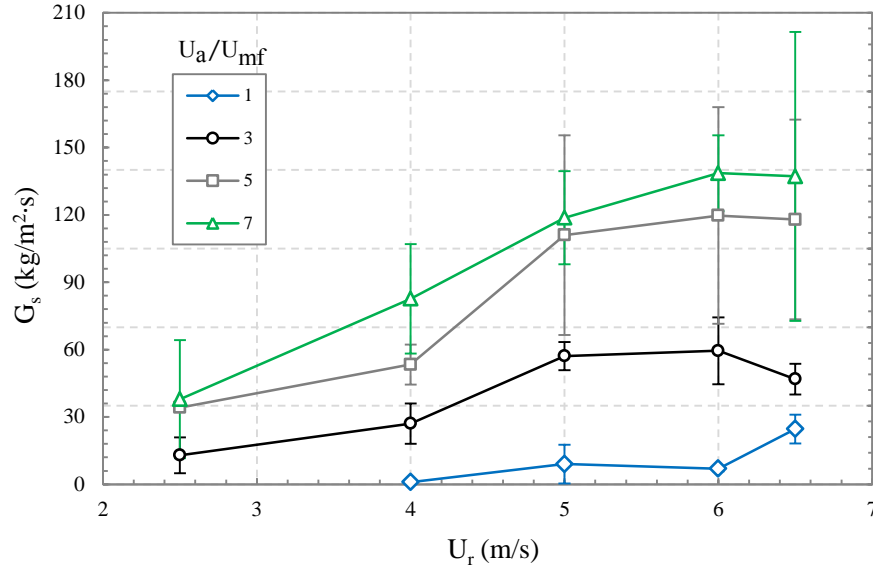
Figure 3.2: Solids circulation flux as a function of riser fluidization velocity for different U_a/U_{mf}. Error bars correspond to standard error of measurements.

Based on the experimental findings in an apparatus similar to that employed in this study, Xu (2010) and Fushimi et al. (2011) suggested that the pressure head in the loop-seal or gas-sealing bed provides the driving force to feed the particles to the bottom of the riser. The relationship between riser superficial gas velocities, solids circulation flux and pressure head in the loop-seal (pressure difference between P26 and P27 in Figure 2.6) is depicted in Figure 3.3 for the different aeration velocities (U_a) tested in our system. As can be seen, the pressure drop across the vertical section of the loop-seal ($\Delta P_{ls,v}$) increases with increasing solids circulation flux (G_s). Beyond U_r = 5.0 m/s, the pressure in the loop-seal did not increase further as U_r increased. This indicates that the pressure exerted by the solids in the loop-seal is an important factor to account for if high circulation fluxes from riser to BFB are desired, as found by previous researchers.

At high solids flux, that is for $U_r \geq 5.0$ m/s and $U_a \geq 5U_{mf}$, it was observed visually (during the solids mass flux measurements) that the solids flow through the downcomer from the primary cyclone was periodic, rather than continuous. This behaviour resulted in higher deviations in the measurements (as seen in Figures 3.1 and 3.2), as there were some difficulties in collecting the entire batch of solids flowing down the return leg. At the same time, higher fluctuations in pressure drop were observed at these operating conditions. Figure 3.4 shows an example of variation of pressure drop across the riser (ΔP_r = P$_3$-P$_{15}$) and across the loop-seal ($\Delta P_{ls,v}$ = P$_{26}$-P$_{27}$) at U_r = 6 m/s and U_a = 5U_{mf}, showing the variation of solids inventory between the riser and loop-seal.
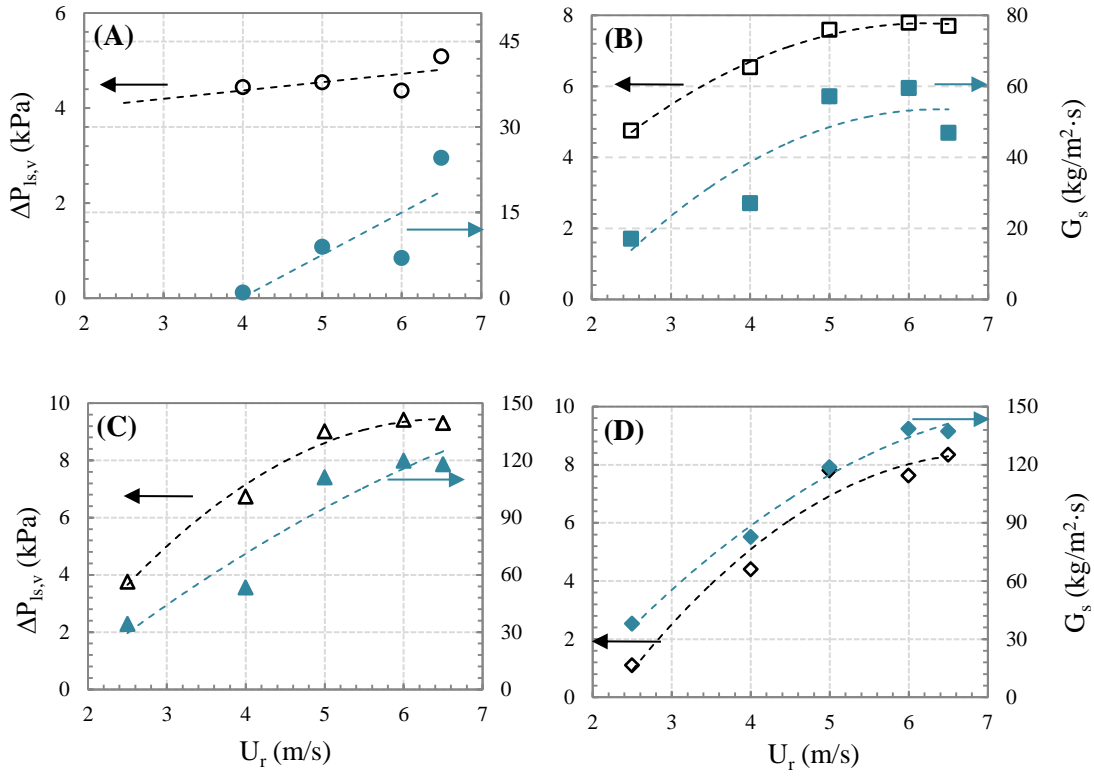
Figure 3.3: Relationship between riser superficial velocity (U_r), pressure head in loop-seal ($\Delta P_{ls,v}$) and solids circulation flux (G_s). (A) $U_a=1U_{mf}$, (B) $U_a=3U_{mf}$, (C) $U_a=5U_{mf}$, (D) $U_a=7U_{mf}$.
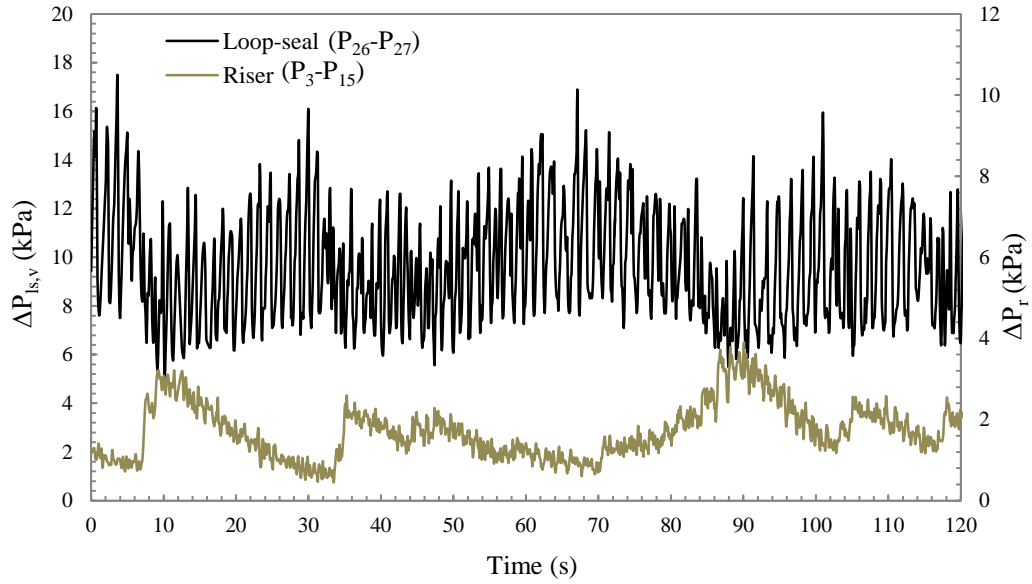
Figure 3.4: Example of pressure fluctuations in riser and vertical section of loop-seal. $U_r=6$m/s, $U_a=5U_{mf}$. See Figure 2.6 for position of pressure ports.

The above gas-solid behaviour could result from "choking" in the system at these operating conditions. Choking has been used to describe a phenomenon in vertical pneumatic transport systems, where there is an abrupt change in the gas-solid behaviour when varying the operating conditions (Bi et al, 1993). Due to controversy when defining choking in conveying systems, Bi et al (1993), extensively reviewed the different choking mechanisms found by previous researchers and classified them into three main categories:

Type C choking or "classical choking" refers to a system that experience severe slugging flow when the gas velocity of the transport line is reduced. As the gas velocity is reduced, a dense zone starts to form along the vertical pipe which eventually collapses to terminate in the formation of slugs/plugs along the bed. Slug formation could be persistent to the point that the bed becomes inoperable under these operating conditions. Vertical conveying systems of small diameter operating with particles of a large size and high density are most likely to experience classical choking (Bi et al., 1993; Xu et al., 2001; Yang, 2004).

Type B or "premature choking" occurs due to standpipe/blower limitations. A system becomes inoperable if the blower is not able to supply the sufficient pressure head to support the weight of the particles in the bed. As for standpipe limitations, the inoperability of the system could affect whether solids can be fed to the riser at the predetermined flow rate because the gas flow is not enough to entrain the particles from the bed. In that case, the pressure balance between the riser and the down-comer can no longer be maintained, interrupting the operation and destabilizing the system.

Type A is another choking mechanisms identified by Bi et al. (1993), denoted as "accumulative choking". Type A choking occurs at the point where significant solids recirculation at the wall of the reactor appears as the gas velocity is reduced causing solids to accumulate at the bottom of the column. Accumulative choking is therefore referred to as the transition from a dilute or almost uniform solids concentration along the column to a point where there is axial variation in voidage due to coexistence of a dense phase at the bottom and a more dilute zone at the top of the riser or transport line. The point at which solids begin to accumulate at the bottom of the column corresponds to the maximum saturation carrying capacity of the system. The saturation carrying capacity is thus the maximum solids circulation flux (G_s^*) that a given gas velocity (U_r) can support without forming a dense region at the bottom of the riser (Weng & Chen, 1982; Bi et al., 1993; Xu et al., 1999). The collapse of the dilute suspension that leads to the formation of a dense zone has been attributed to the formation of particle clusters or streamers (Bi et al., 1993; Xu et al., 2001).

When decreasing the gas velocity in a vertical solids conveying system at a fixed solids mass flux or increasing the solids mass flux at a fixed gas velocity, the type A choking could begin, indicating the transition between dilute-phase transport and fast fluidization, followed by type C (for slugging beds) or type B if there are standpipe/blower limitations.

Among the three choking categories, types A and C represent distinctive gas-solid behaviour with continuous operation, whereas type B is directly related to facility or design limitations that cause instabilities and

subsequent interruption of the operation. Type A has been found to be the more common type of choking in a vertical pneumatic column such as a CFB riser (Xu et al., 2001).

Grace (1982) presented a set of criteria that establishes the conditions necessary for a fluidized bed to develop slug flow regime. These conditions are presented in Table 3.1 and have been applied to the present research to confirm slugging in the riser.

Table 3.1: Criteria for slugging formation in fluidized bed system (Grace, 1982)

1	$U_r > U_{ms} = U_{mf} + 0.07\sqrt{gD}$
2	$L \geq 3.5D\left(1 - \dfrac{1}{\sqrt{N_{or}}}\right)$
3	$(d_b)_{max} \geq 0.6D$
4	$U_{ms} \leq U_r < U_c$

Here U_{ms} is the minimum slugging velocity, U_c is the gas velocity corresponding to the onset of the turbulent fluidization regime, and N_{or} is the number of holes in perforated place (N_{or} =128) . The maximum stable bubble size $(d_b)_{max}$ can be estimated from

$$(d_b)_{max} = 2.0\frac{(U_t^*)^2}{g} \tag{3.2}$$

where U_t^* is the terminal velocity calculated for a spherical particle of diameter $2.7d_p$ (Grace, 1982).

According to the above criteria, riser dimensions (length and diameter), and the data reported on Table 3.2, only condition N° 4, which requires that the superficial gas velocity is lower than the onset of turbulent fluidization, but higher than the minimum slugging velocity, is not fulfilled. Instead, the riser was operated at gas velocities considerably above U_c. This indicates that the slugging regime was not likely to have been encountered for the DFB riser conditions investigated. Thus, the abrupt change in gas-solid behaviour that resulted in higher deviations in G_s at $U_a \geq 5U_{mf}$ and $U_r \geq 5.0$ m/s (seen in Figure 3.2), can be attributed to Type A choking.

Table 3.2: Operating conditions for slugging flow regime determination

Variable	Value
Riser gas velocity, U_r (m/s)	4.0, 5.0, 6.0, 6.5
Minimum slugging velocity[1], U_{ms} (m/s)	0.20
Minimum fluidization velocity, U_{mf} (m/s)	0.15
Gas velocity at the onset of turbulent regime[2], U_c (m/s)	1.71
Maximum bubble size, $(d_b)_{max}$ (m)	8.78

[1]Based on Stewart & Davidson (1967); [2]based on Abba et.al., (2003)

3.2. Axial Solids Hold-up in Riser

The axial variation of solids holdup in the riser is an important parameter that provides information on the flow regime at different operating conditions. Parameters such as mixing, heat and mass transfer and reaction performance are affected by the flow regime in the vertical pneumatic transport line.

As mentioned in the Chapter 1, the axial solids distribution in a riser varies according to the amount of gas injected at the bottom, as well as the solids circulation flux. Therefore, the following discussion focuses on the effect of superficial gas velocity in the riser on the solids mass flux around the loop.

3.2.1. Effect of riser superficial gas velocity

The cross-sectional average solids holdup (ε_p) was estimated based on differential pressure drop as reported in Chapter 2. Figure 3.5 shows how the solids holdup varied with riser superficial gas velocity (U_r) at aeration velocities U_a of: $3U_{mf}$ (A); $5U_{mf}$ (B); and $7U_{mf}$ (C). It is seen that the solids holdup in the riser increased at the bottom ($z_r < 0.40$ m) and middle section (0.40 m $< z_r < 3.90$ m) as U_r was reduced at all U_a. At the lowest G_s ($U_a = 3U_{mf}$), the effect of U_r on ε_p was negligible at $U_r \geq 6.0$ m/s at every reactor height, as the concentration was very dilute, with almost no variation of ε_p along the riser ($\varepsilon_p \leq 0.002$). As the superficial gas velocity decreased to 5.0 m/s, a dense region began to appear at the bottom of the riser, with solids fraction varying from 0.005 to 0.01. A lower solids concentration ($\varepsilon_p \sim 0.001$) was observed in other sections of the riser.
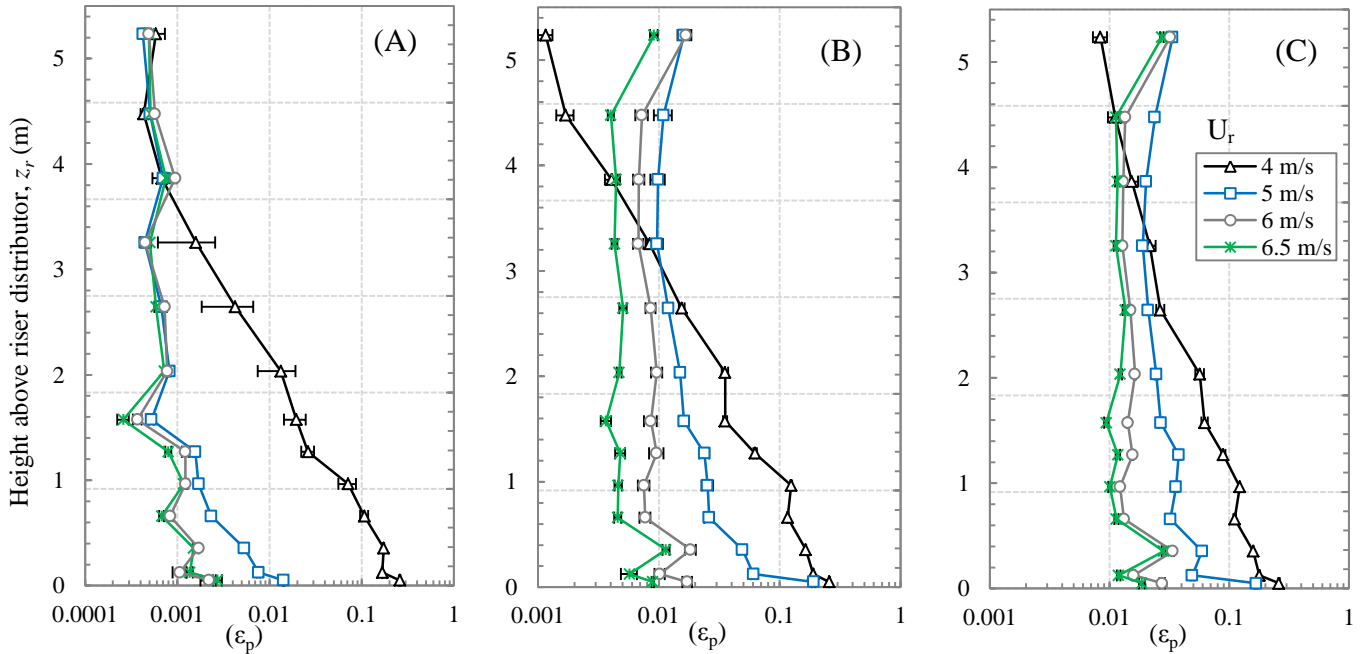
Figure 3.5: Axial distribution of solids in riser at different U_r: (A) $U_a = 3Umf$, (B) $U_a = 5U_{mf}$, (C) $U_a = 7U_{mf}$. Error bars correspond to standard error of measurements.

Little variation of the solids holdup was observed at $z_r > 1.0$ m when U_r is increased from 5.0 m/s to 6.5 m/s. This is because, as shown in Figure 3.2, the entrainment of solids from the reactor is negligible at $U_r > 5.0$ m/s. A significant increase in solids holdup was observed when U_r was reduced to 4.0 m/s, especially in the lower and middle section of the riser where ε_p varied from 0.27 to 0.07. Substantial variation of solids holdup was noted at the bottom of the reactor, with $\varepsilon_p > 0.11$ at $z_{r<}$ 0.40 m. Similar behaviour is seen in Figure 3.5B and 3.5C where ε_p is seen to have decreased as U_r was reduced. Formation of a dense zone is also seen in Figures 3.5B and 3.5C with U_r = 5.0 m/s, also reflecting the choking at the transition between dilute-phase pneumatic transport and the fast fluidization flow regime. It is believed that solids downward flow at the wall of the reactor began at these operating conditions causing the formation of the dense zone (Bi & Grace, 1993). However, this observation could not be confirmed, as no flow visualization in the riser was possible during the experiments. Bai et al. (1992) and Pugsley et al. (1997) showed that abrupt exist configurations, such as a sharp 90° elbow (as in this investigation), change the solids profile significantly due to particle recirculation at the top. Therefore, at high gas velocities, $U_r \geq 5.0$ m/s, where the entrainment of particles becomes significant (Figures 3.5B and 3.5C), the solids holdup was increased at the top of the riser, resulting in a so-called C-shaped cross-sectional solids profile characteristic of fast fluidization regime (Bai et al, 1992) and, in some cases, dilute-phase flow, where the solids holdup was slightly higher at the entrance due to particle acceleration.

3.2.2. Effect of solids circulation flux

The cross-sectional solids holdup (ε_p) is also influenced by the particle circulation in the system. Because the circulating flux between the combustor/calciner and gasifier/carbonator in an integrated practical system needs to be high to transfer enough CaO and heat, only the influence of the highest solids circulation fluxes (corresponding to $U_a=3U_{mf}$, $5U_{mf}$ and $7U_{mf}$) on solids concentration along the riser is evaluated in this section. Figure 3.6 shows the unique effect of solids circulation flux (G_s) on the axial distribution of solids in the riser at different superficial gas velocities (U_r). At $U_r = 4.0$ m/s (Figure A), the solids concentration was almost constant at the bottom of the riser and increased at higher locations as G_s increased from 27 to 83 kg/m²·s. Bai & Kato (1999) found that ε_p changed little with solids circulation flux when the maximum attainable solids circulation rate was higher than or equal to the maximum carrying capacity, i.e., $G_s \geq G_s^*$. Thus, for this fluidization condition, G_s^* is considered to be reached at 27 kg/m²·s. At higher superficial gas velocities U_r = 5.0 m/s (Figure 3.6B), ε_p increased significantly when G_s increased from 57 to 111 kg/m²·s. At 57 kg/m²·s the concentration of solids was dilute, with $\varepsilon_p \leq 0.01$. As G_s increased to 111 kg/m²s ($U_a=5U_{mf}$), the dense zone in the bottom section of the riser increased in depth, indicating transition from dilute-phase to fast fluidization.

A further increment in G_s did not change ε_p greatly at the bottom of the riser. Thus, the maximum saturation carrying capacity of the transport line was reached at $G_s^*=111$ kg/m$^2\cdot$s.
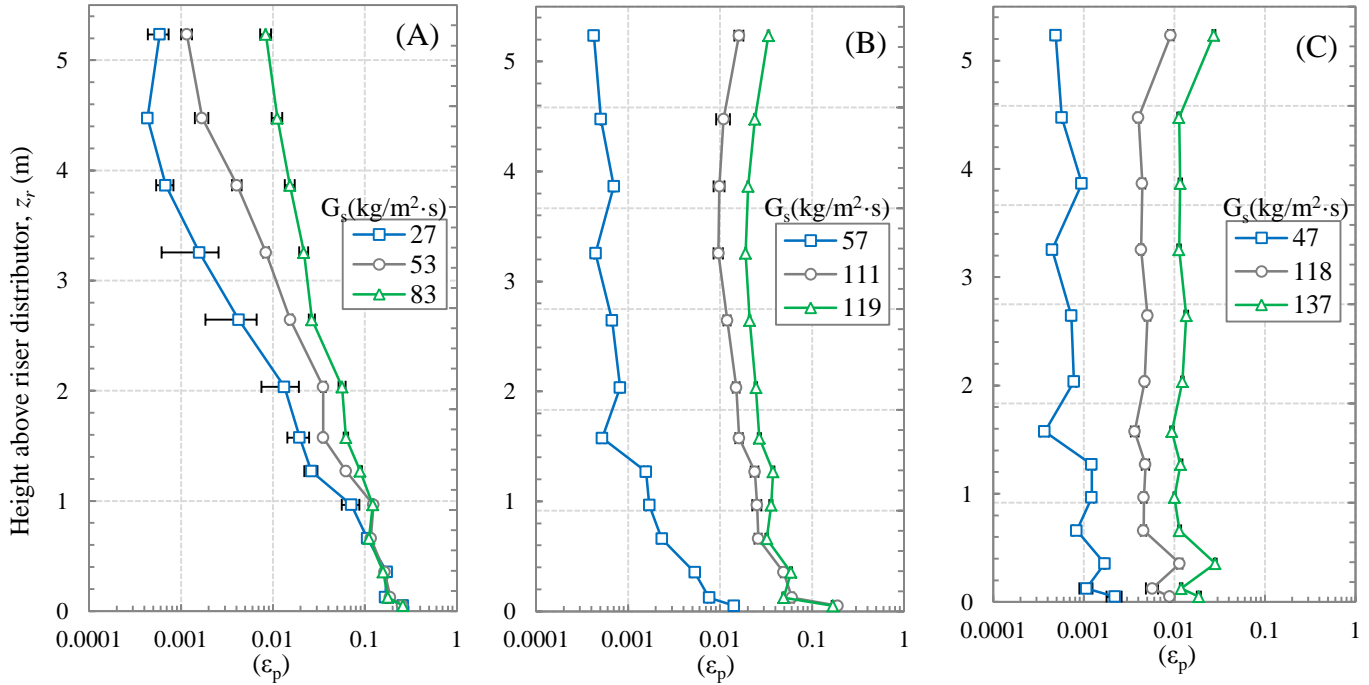
Figure 3.6: Axial solids profile variation with solids circulation flux at different riser velocities: (A) U_r = 4.0 m/s, (B) U_r=5.0 m/s, (C) U_r = 6.5 m/s. Error bars correspond to standard error of measurements.

The cross-sectional solids holdup increased at all riser heights when G_s increased from 47 to 137 kg/m$^2\cdot$s at U_r = 6.5 m/s (Figure 3.6C). The flow regime at these operating conditions is considered to be dilute, with ε_p low at the bottom of the riser. The cross-sectional average solids holdup (ε_p) along the riser at these operating conditions is equal or less than 0.03. As illustrated in Figures 3.6B and 3.6C, the solids holdup increased at the top of the reactor at G_s >100 kg/m$^2\cdot$s and was high due to exit geometry effects (as mentioned in Section 3.2.1).

3.2.3. Variation of riser pressure drop (ΔP_r) and axial solids holdup (ε_p) with U_r and G_s

Accumulative type A choking, which represents the transition from pneumatic transport (dilute-phase regime) to fast fluidization, has been said to occur when there is an abrupt change in the voidage or pressure drop across the riser of a circulating fluidized bed. Figure 3.7 illustrates the effect of superficial gas velocity (U_r) on ε_p at different riser locations for a fixed aeration velocity ($U_a=5U_{mf}$). The axial solids holdup at the bottom

decreased with increasing U_r, whereas ε_p at the middle remained almost constant at all superficial gas velocities, and ε_p increased at the top at $U_r \geq 5.0$ m/s where the entrainment rate was high. ε_p exhibits an inflection point between $U_r = 5.0$ and 6.0 m/s at the bottom section corresponding to the choking point. When U_r exceeded the choking velocity, the concentration of solids at all locations in riser was very low corresponding to the dilute-phase flow regime. The abrupt change in gas-solids flow is also reflected by the pressure gradient at the bottom of the riser (P_1-P_5 in Figure 2.6), as shown in Figure 3.8, with the pressure drop decreasing considerably to an almost constant value at $U_r \geq 6.0$ m/s.
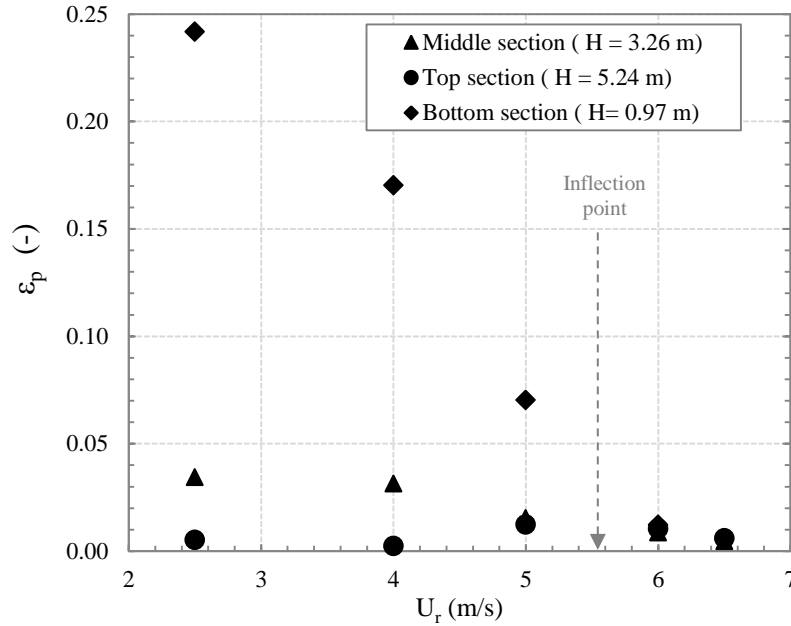
Figure 3.7: Solids fraction at different sections in the riser as a function of U_r and at $U_a=5U_{mf}$.
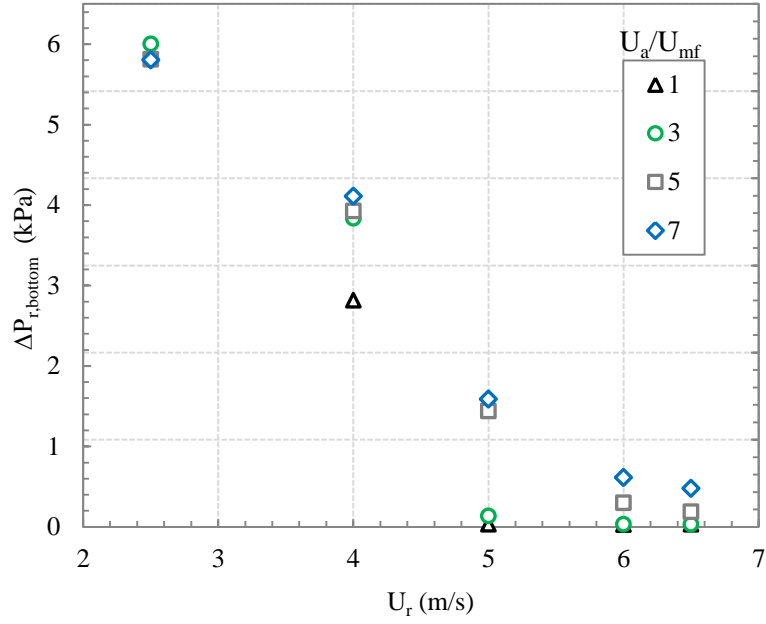
Figure 3.8: Variation of pressure drop at the riser bottom for different U_r.

Figure 3.9 illustrates the relationship between G_s and the pressure drop over the whole riser for three different superficial gas velocities. As can be seen, the pressure drop and G_s appear to be related exponentially for each of the three velocities. No significant variation of pressure drop across riser ($\Delta P_r = P_1 - P_{14}$, in Figure 2.6) is seen at low G_s, indicating dilute-phase flow. As the solids circulation flux increased beyond the maximum carrying capacity, a sharp increase in pressure drop is observed. This sudden change denotes the transition between pneumatic transport regime to fast fluidization, as noted by Bi & Grace (1999) and Bi & Liu (2010). Some systems may become inoperable as soon as the bottom dense phase is formed if the blower is not able to supply sufficient pressure head to support the dense phase. However, note that the present DFB could operate stably under these operating conditions.
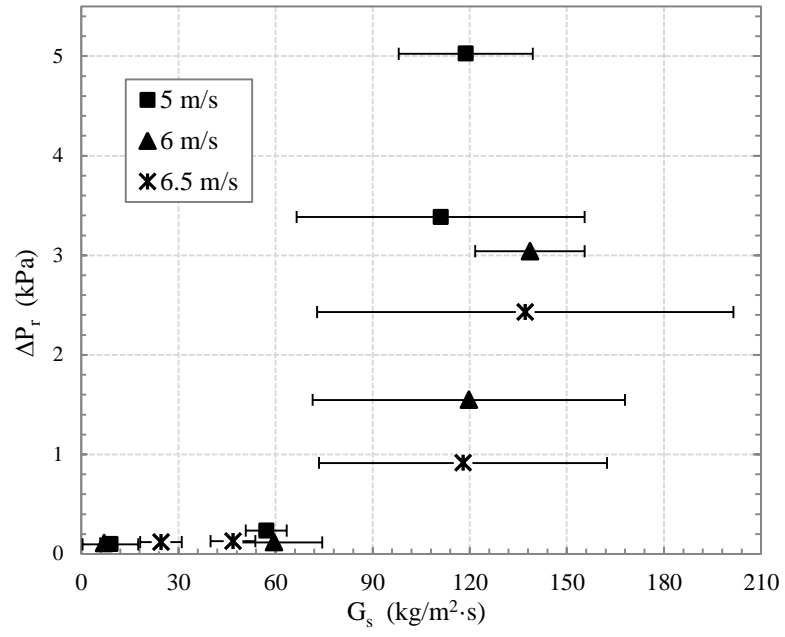
Figure 3.9: Effect of solids circulation flux on pressure drop across the riser for different U_r. Error bars correspond to standard error of measurements.

3.3. Pressure Profiles

In a CFB the pressure balance must be maintained, i.e., the pressure at the bottom of the riser minus the pressure drop at the bottom of downcomer (right side of loop in Figure 3.10) should be equal to the pressure drop gradient across the loop-seal to achieve stable operation of the system. Figure 3.10 presents a typical pressure profile for the system investigated in this project. The pressure loop symbolizes the passage of gas and solids in the system, with *A-B-C-D-E-F-G-H-A*, representing the pressures at *Riser inlet–Riser exit–Cyclone-riser connection pipe–Upper downcomer–Lower downcomer–BFB–Loop-seal bottom–Loop-seal top–Riser inlet,* respectively. The pressure at every section of the loop is plotted against the height from riser distributor, with the pressure at the outlet of secondary cyclone as the reference pressure (P_{ref}).
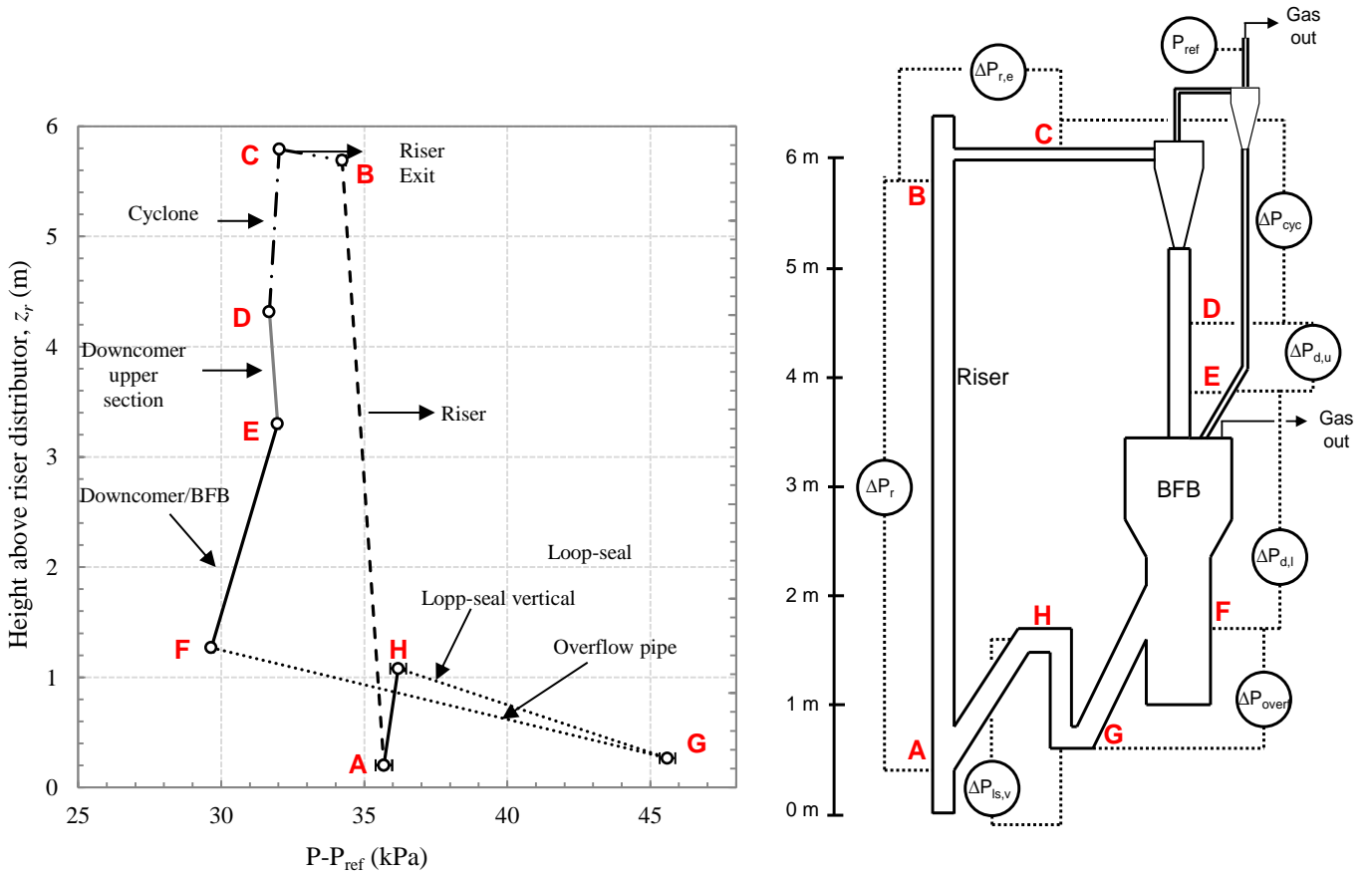
Figure 3.10: Typical pressure profile of chemical looping system. Conditions: 23°C, $U_r = 6.0$ m/s, $U_a=7U_{mf}$ ($G_s= 139$ kg/m^2·s).

3.3.1. Effect of solids circulation flux

Figures 3.11 and 3.12 illustrate the pressure profiles for different solids circulation fluxes (G_s) at two superficial gas velocities (U_r = 5.0 and 6.0 m/s). It is observed that the pressure at every point in the system increases as the aeration flow is increased. The highest pressure around the loop is encountered at the bottom of the loop-seal (point G) for all conditions, and this increases with increasing solids circulation flux (G_s). As mentioned above, the pressure gradient between the bottom and top of loop-seal provides the driving force to feed the particles to the bottom of the riser. Thus, when the solids circulation flux increases, a corresponding higher pressure drop across the riser (A-B) is noted, due to the higher particle concentration in the reactor, especially at its bottom. Owing to the significant particle entrainment and the constrictions at the exit of the reactor, the pressure drops at the exit and across the connection with the primary cyclone (B-C), increase with increasing G_s. As the BFB is open to atmosphere, the pressure at the overflow pipe level (point F) is the lowest pressure around the system.
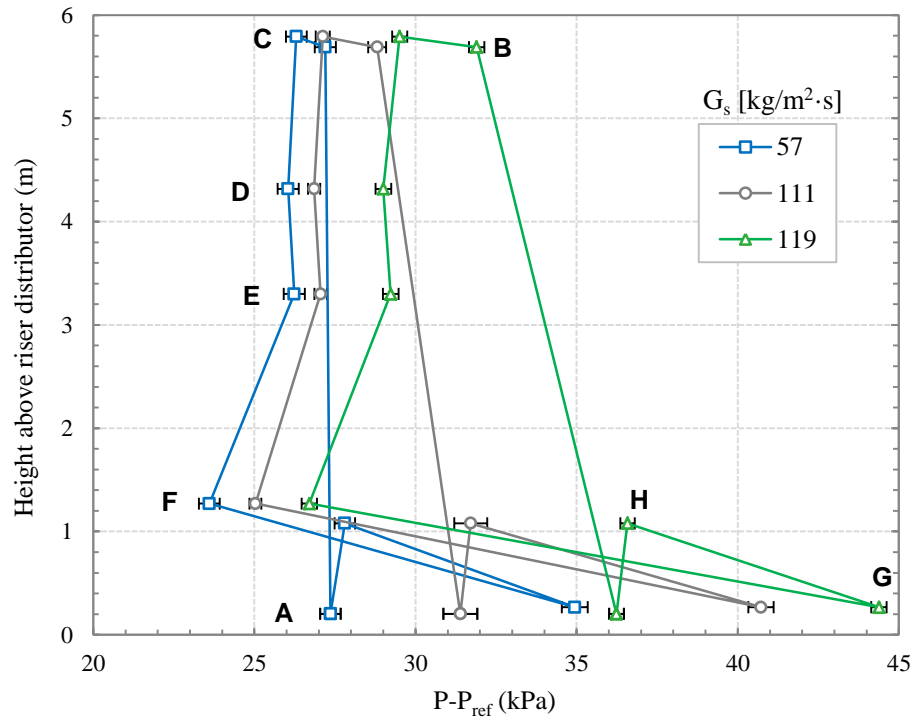
Figure 3.11: Pressure profiles at different solids circulation flux for 23°C and U_r = 5.0 m/s. Error bars correspond to standard error of measurements.
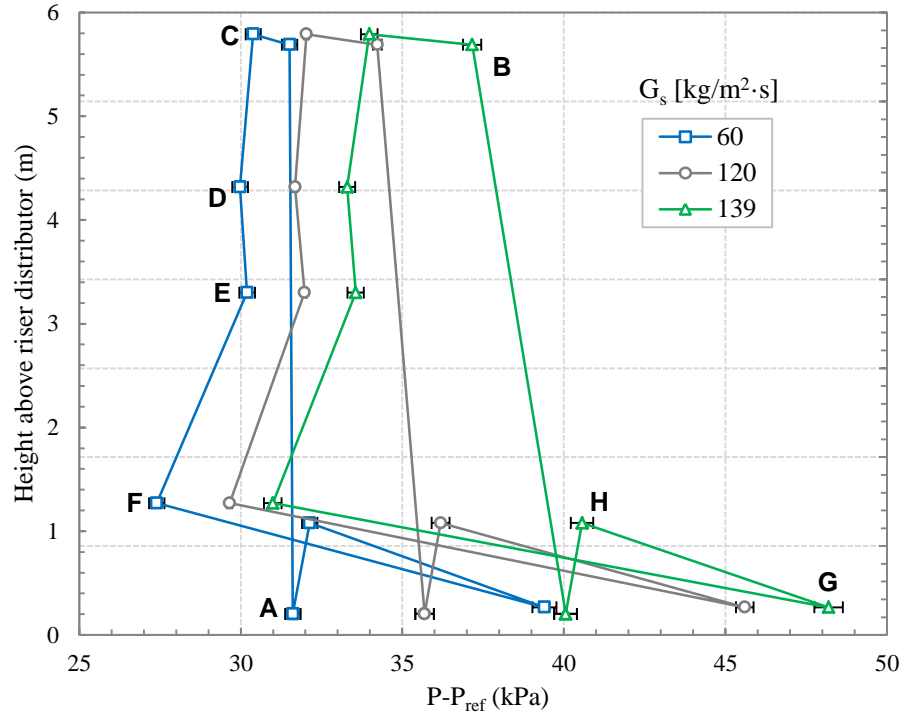
Figure 3.12: Pressure profiles at different solids circulation flux for 23°C and $U_r = 6.0$ m/s. Error bars correspond to standard error of measurements.

3.3.2. Effect of superficial gas velocity

Figures 3.13 and 3.14 illustrate the pressures profiles as a function of riser gas velocity (U_r) for aeration velocities of, $U_a = 5U_{mf}$ and $7U_{mf}$. The results indicate a shift in the pressure profile towards a higher pressure as the volumetric flow of air is increased at the bottom of the riser. Due to the high solids entrainment at $U_r \geq$ 5.0 m/s, the pressure drop between the bottom and top of the riser (i.e., between points A and B) progressively declines, resulting in a smaller pressure difference compared to that obtained at the lowest U_r. The pressure profile also indicates the effect of G_s as this parameter only increases significantly up to $U_r = 5.0$ m/s (as seen in Figure 3.2). Due to the accumulation of solids at the bottom of the riser, the pressure head in loop-seal (G-H) is reduced to compensate for the increased pressure drop across the riser.
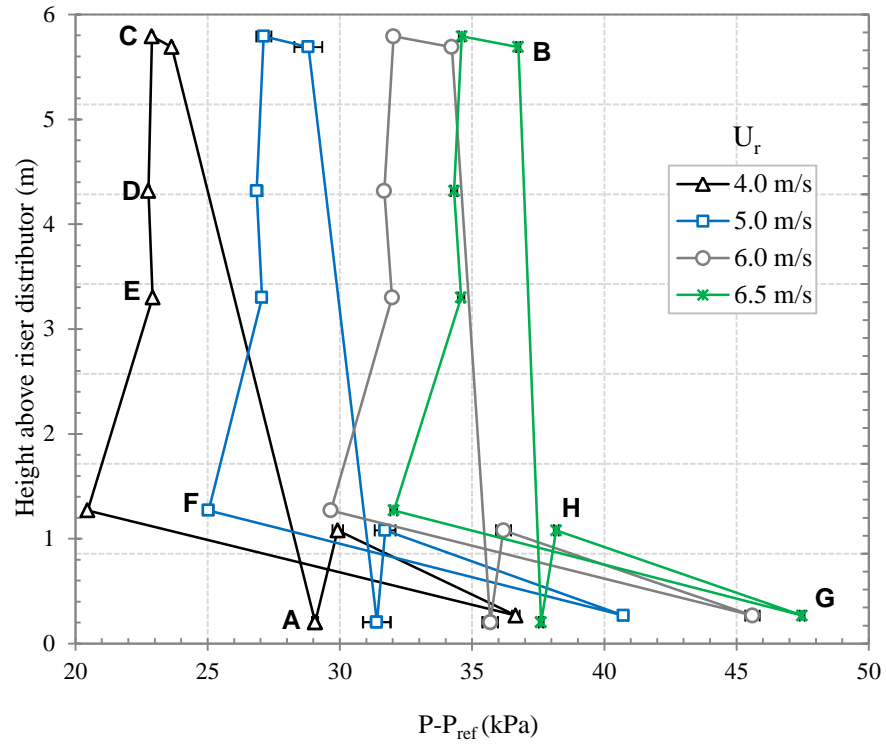
Figure 3.13: Pressure profiles at different riser superficial velocities for 23°C and $U_a = 5U_{mf}$. Error bars correspond to standard error of measurements.
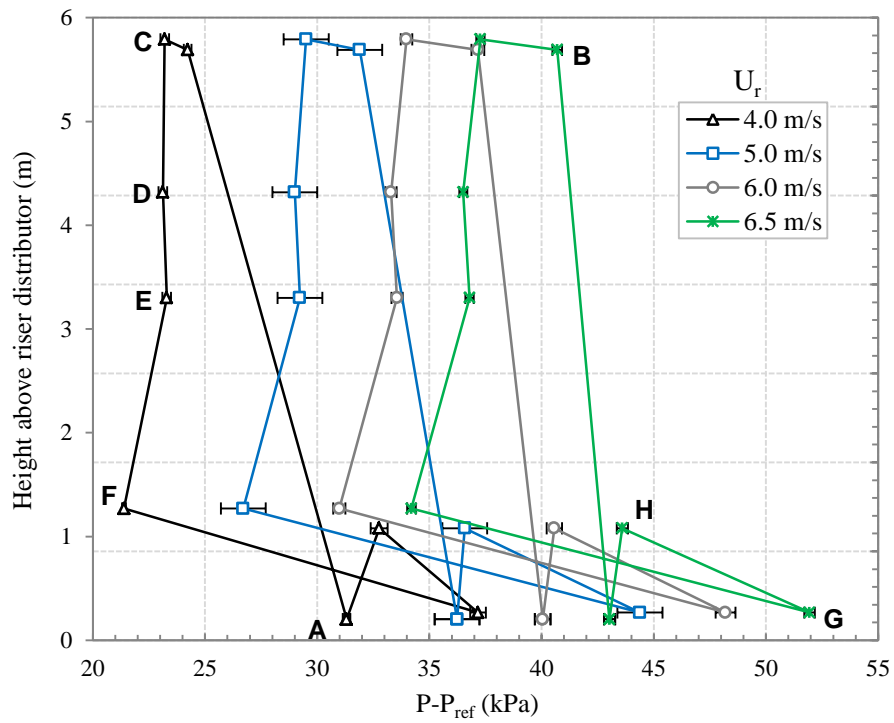
Figure 3.14: Pressure profiles at different riser superficial velocities for 23°C and $U_a = 7U_{mf}$. Error bars correspond to standard error of measurements.

3.4. Gas Leakage

One of the drawbacks when interconnected fluidized beds are employed to carry out different reactions is the possibility of gas leakage between the vessels. If oxygen leaks into a steam gasifier, this may react with the syngas (H_2 and CO) to form H_2O and CO_2, decreasing the gasification efficiency. Aeration in the loop-seal may also dilute the product gas in the BFB. In ideal operation, gas injected at the different ports in the loop-seal should follow the path of the solids from BFB to riser bottom. However, depending on the pressure balance around the loop and the location of the aeration ports, gas added to the loop-seal may leak into the BFB.

The evaluation of gas leakage in this study focuses only on leakage between the coupled fluidized beds. Helium was used as the tracer gas with injection volume concentrations less than 3.0% in either reactor. A mass flow controller previously calibrated for helium was employed to inject a predetermined amount of helium into the flow entering either the BFB or riser. A *Varian CP-4900* micro Gas Chromatograph (GC) measured the concentrations at the inlet and outlet of the reactors (See Figure 2.2). Helium was injected for a period long enough to obtain a stable concentration at the outlet of the reactor (approx. 40 min). Figure 3.15 shows an example of helium measurement at the BFB outlet. The average of the last five points was used to calculate the gas leakage for the specific operating condition, defined as the fraction of gas injected into one reactor that reaches the outlet of the other reactor.
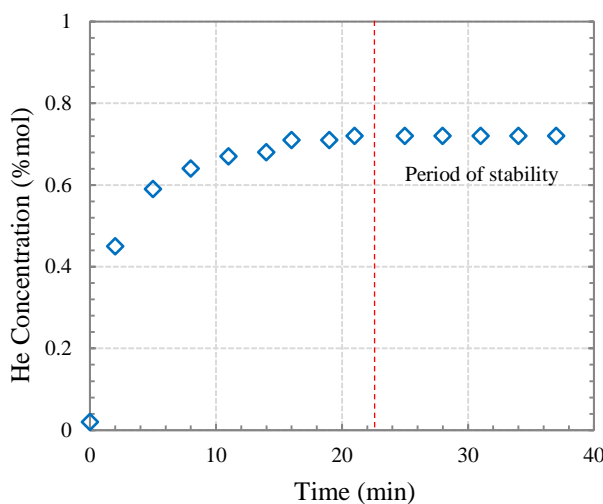
Figure 3.15: Example of gas leakage detection at BFB outlet.

3.4.1. Gas leakage from BFB to riser

To examine the gas leakage from the BFB to the riser, helium was injected at the BFB inlet and detected at the riser outlet using the Micro GC (as seen in Figure 3.16). Figure 3.16 illustrates the possible routes for the gas to leak into the riser side. Routes A and B take place against the solids pathway and encompass the leakage through the downcomer/standpipe of the primary cyclone and through the standpipe of the secondary cyclone, respectively. On the contrary, in route C gas from the BFB follows the solids trajectory through the Loop-seal–Riser–Primary cyclone–Secondary cyclone.

In order to investigate the influence of operating conditions such as riser velocity and loop-seal aeration, gas leakage was studied at U_r varying from 4.0 to 6.5 m/s with $U_a = 3U_{mf}$, $5U_{mf}$ and $7U_{mf}$. Three experiments were conducted for each set of condition to estimate the repeatability of the experimental results. For these operating conditions, no gas leakage from the BFB to riser side could be detected. This is because the pressure at the bottom of the loop-seal is always higher than that at the BFB, as this reactor is open to the atmosphere. Therefore all the gas produced in the BFB left the reactor through the internal cyclones (shown in Figure 2.1) instead of following the solids through the loop-seal. Thus, having a sufficient pressure head in the loop seal is important to prevent gas from leaking into the riser.
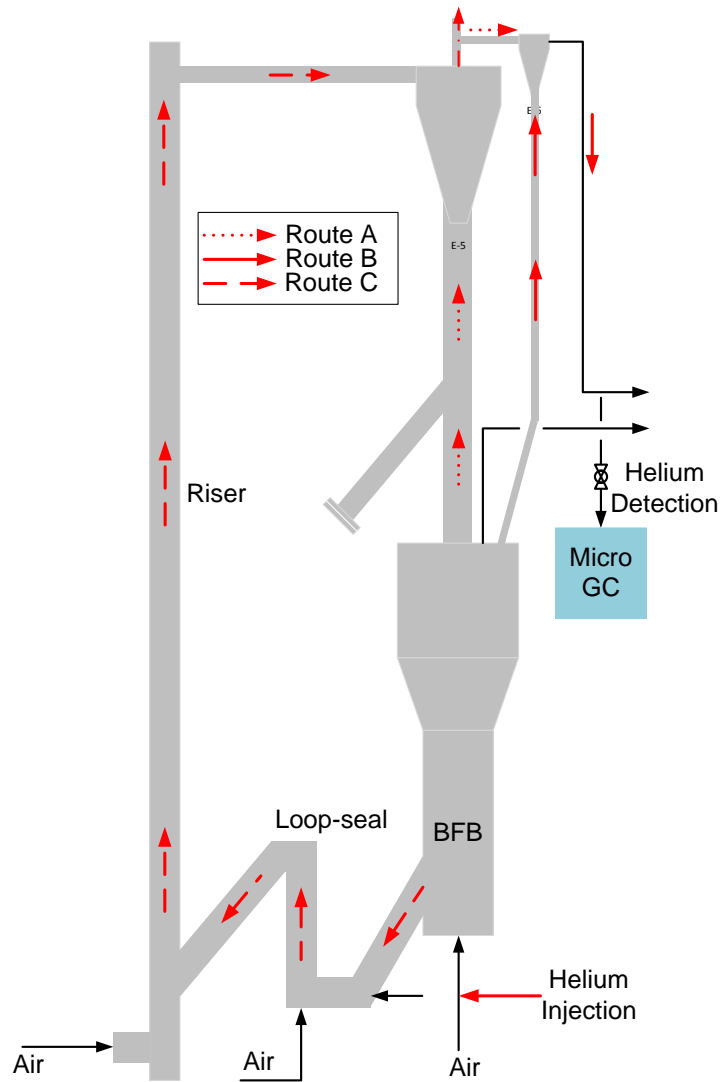
Figure 3.16: Schematic diagram of possible routes for gas leakage from BFB to riser

3.4.2. Gas leakage from riser to BFB

Gas leakage from the riser to the BFB was also determined following the procedure explained above. Figure 3.17 shows the possible routes for gas to leak from the riser to the BFB. For this case, only in route A the gas may leak into the BFB against the direction of the solids flow through the loop-seal; whereas in routes B and C, the gas follows the solids path. The path for routes B and C are *Riser − Primary cyclone − Secondary cyclone − BFB,* and *Riser − Primary cyclone − BFB*, respectively. Gas samples were taken from the loop-seal, downcomer of primary cyclone and standpipe of secondary cyclone to determine the gas leakage route. In this case, helium was detected at the outlet of the BFB. Analysis of the samples at the three different sections of the unit (mentioned before) reveals that gas leakage from riser to BFB only occurs via route A, i.e., through the downcomer of the primary cyclone, as no helium was detected at the other two locations.
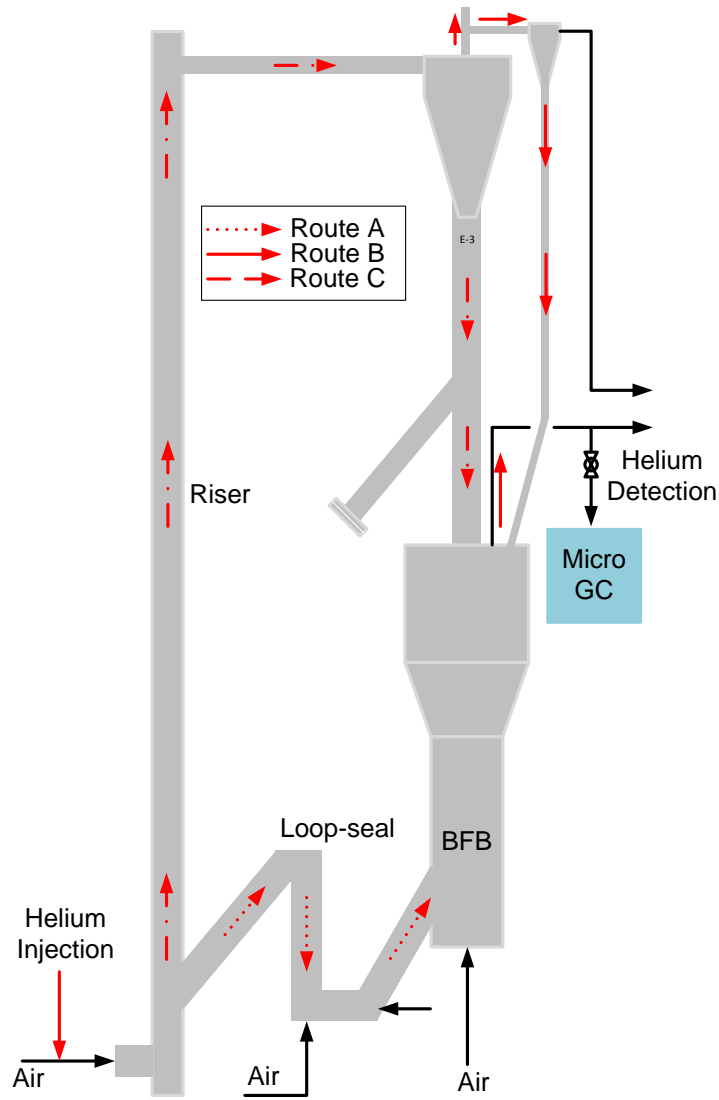
Figure 3.17: Schematic diagram of possible routes for gas leakage from riser to BFB

Figure 3.18 shows the gas leakage versus the aeration velocity (U_a) at different riser superficial velocities, (U_r). Surprisingly, for a specific superficial gas velocity, the gas leakage decreased with increasing aeration velocity, which has a positive correlation with the solids circulation flux from riser to BFB. Approximately, 8.7% to 11.5% v/v of the riser product gas found its way into the BFB. Unlike previous findings on gas leakage in DFB where gas leakage decreases with decreasing the solids mas flux between the reactors (Johansson et al., 2003 and Xu, 2010), the gas leakage in this study was found to decrease with increasing solids mass flux. As the solids circulation flux increased, the concentration of solids flowing down to the BFB increases; thereby, reducing the available area for the gas to flow through the standpipe of the primary cyclone. This implies that slippage of gas from the riser to the BFB should decrease to satisfy the pressure

balance between the two parallel paths (via the internal cyclones of the BFB, and the primary and secondary cyclone of the riser) that direct the product gases to the ventilation system.
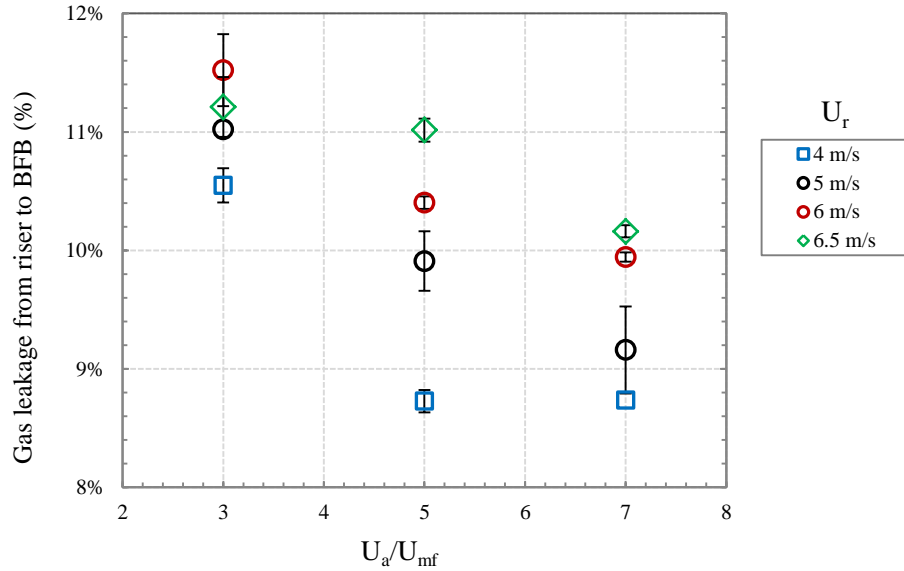
Figure 3.18: Gas leakage from riser to BFB at different aeration velocities. Error bars correspond to standard error of measurements.

Figure 3.18 also presents the effect of riser gas velocity on the gas leakage from the riser to the BFB. It is observed that the gas leakage increased with increasing volumetric flow of gas injected at the bottom of the riser. These results do not match the effect of solids circulation flux on the gas leakage described in the previous paragraphs, since U_r also positively influences G_s to some extent. This divergence can be attributed to the fact that the increments of the total flow in the riser are significantly greater than the flow of gas used for aeration of the loop-seal. Since the total riser volumetric flow increased, the amount of gas leaking through the standpipe of the primary cyclone accordingly increased to meet the pressure balance, as discussed above.

Chapter 4: Scale-up of Dual Fluidized Bed: Effect of Temperature on Hydrodynamics

The present chapter reports on the experimental investigation of fluidization behaviour of limestone particles at elevated temperatures. The use of identical reactor size, geometry and configuration, particle properties such as shape factor, particle size and density allows determination of the effect of viscosity and density of the gas on the hydrodynamics of the DFB. Table 4.1 presents the experimental conditions evaluated in this section where the reactors were fluidized with compressed air under atmospheric pressure at three bed temperatures (25, 80 and 250°C). The system was operated at two superficial gas velocities $U_r = 4.0$ and 6.0 m/s, which for the cold model experiments correspond to the fluidization and dilute-phase operation, respectively.

Table 4.1: Operating conditions for the DFB unit

Temperature (°C)	23°C ± 3°C	80°C ± 5°C	250°C ± 8°C
Gas viscosity (kg/m·s)	1.85E-05	2.12E-05	2.81E-05
Gas density (kg/m^3)	1.19	1.00	0.68
Fluidization velocity in riser, $U_{r,}$ (m/s)	4-6	4-6	4-6
Aeration velocity in loop-seal (U_a/U_{mf})	3, 4, 5	3, 4, 5	3, 4, 5
Fluidization velocity in BFB, $U_{BFB,}$ (m/s)	0.24	0.24	0.24
Minimum fluidization velocity[1], $U_{mf,}$ (m/s)	0.15	0.14	0.11
Particle terminal velocity[2], $U_{t,}$ (m/s)	2.52	1.94	1.02

[1]Based on Wen & Yu (1966); [2]based on Kunii & Levenspiel (1991)

In order to achieve hydrodynamic similarity between a cold model and a hot model, a full set of dimensionless parameters derived from the non-dimensionalization of the governing equations must be kept constant in the two beds, as noted in Chapter 1. The full set of dimensionless parameters is presented in Equation (1.3). Table 4.2 shows the values of the dimensionless parameters for the three temperatures of the experiments. Since the same unit and particles were used for all these experiments, only the dimensionless parameters independent of gas properties (viscosity and density) were matched for the three experimental sets. The superficial gas velocity in the reactors was kept constant in order to match the Froude number between the experiments. Matching the Froude number of the runs allowed us to determine the effect of gas viscosity and density on the hydrodynamics, a key objective of this part of the research. As temperature in the fluidized bed increases, the viscosity of the gas increases whereas the density decreases. These changes in gas properties make the solids-to-gas density ratio (ρ_p/ρ_g) increase, and the Reynolds number to decrease. Thus, the experiments performed in this Chapter are an indirect measurement of the effect of these dimensionless parameters on the hydrodynamics of the DFB. As reported in Xu (2010), matching ρ_p/ρ_g between the cold and hot models can be very challenging as sometimes particles of unreasonable density need to be used in the cold model to simulate the hydrodynamics of a hot unit.

U_{mf} was estimated for every temperature, and the flow in the loop-seal was adjusted accordingly to maintain the U_a/U_{mf} ratio constant for different runs and inherently the solids circulation flux. To confirm this, the solids circulation flux was measured during the experiments. Differential pressure drops were used to estimate the solids volume fraction in the riser based on the assumption that the pressure drop is mainly due to the static weight of the gas-solid suspension to compare the hydrodynamics between the hot and cold model experiments.

Table 4.2: Dimensionless parameters at different reactor temperature.

Fluidization velocity in riser, U_r	4.0 m/s			6.0 m/s		
Temperature	**23°C ± 3°C**	**80°C ± 5°C**	**250°C ± 8°C**	**23°C ± 3°C**	**80°C ± 5°C**	**250°C ± 8°C**
Dimensionless Parameter			**Riser**			
Ar	8218	5254	2016	8218	5254	2016
ρ_p/ρ_g	2407	2870	4252	2407	2870	4252
Fr	40	40	40	90	90	90
Re	10535	7714	3926	15802	11571	5889
Re_p	113	83	42	169	124	63
H/D	147	147	147	147	147	147
$(G_s/\rho_s U_r)_1$	2.36E-03	2.36E-03	2.36E-03	3.46E-03	3.46E-03	3.46E-03
$(G_s/\rho_s U_r)_2$	4.65E-03	4.65E-03	4.65E-03	6.95E-03	6.95E-03	6.95E-03
$(G_s/\rho_s U_r)_3$	7.20E-03	7.20E-03	7.20E-03	8.05E-03	8.05E-03	8.05E-03
Dimensionless Parameter			**BFB**			
Ar	8218	5254	2016	8218	5254	2016
ρ_s/ρ_g	2407	2870	4252	2407	2870	4252
Fr	0.05	0.05	0.05	0.05	0.05	0.05
Re	1983	1452	739	1983	1452	739
Re_p	7	5	3	7	5	3
H/D	16	16	16	16	16	16

4.1. Axial Distribution of Solids Hold-up in Riser

Figures 4.1 and 4.2 present the axial solids holdup (ε_p) in the riser as a function of the operating bed temperature for $U_r = 4.0$ m/s and 6.0 m/s, respectively. As seen in Figure 4.1, ε_p decreased with increasing temperature except at the lowest U_a/U_{mf} ratio and $G_s = 53 \pm 8$ kg/m^2·s, where the axial solids profile remained almost the same. The effect of temperature is mainly seen above the bottom section and below the exit zone of the riser, corresponding to the transition and fully-developed (or dilute-phase) flow regions. However, the temperature seems not to have influenced the solids holdup in the bottom section ($z_r < 0.40$ m) which contains most of the solids inventory in the riser (Figures 4.1B and 4.1C). The variation of ε_p with temperature in the higher sections of the riser could result from changes in particle-gas interactions due to gas viscosity and density effects, since an increase in temperature results in increased viscosity and decreased gas density as previously discussed.

Figure 4.1: Variation of axial solids distribution with temperature at $U_r = 4.0$ m/s.: (A) $U_a = 3U_{mf}$; (B) $U_a = 5U_{mf}$; (C) $U_a = 7U_{mf}$. Error bars correspond to standard error of measurements.

As seen in Figure 4.2 for $U_r = 6.0$ m/s, the solids holdup also decreased with increasing temperature. As in Figure 4.2, the temperature did not significantly change ε_p at the lowest solids flux ($U_a = 3U_{mf}$), which is almost the same as in Figure 4.1A, i.e., $G_s = 59 \pm 15$ kg/m^2·s. The effect of temperature is similar to that of Figure 4.1B and 4.1C at higher solids circulation flux, where ε_p decreased with increasing temperature, except in the bottom part of the reactor. The particle Reynolds number (Re_p) which varied from 113 at 23°C to 42 at 250°C (in the case of Figure 4.1) and from 169 at 23°C to 63 at 250°C (in Figure 4.2) indicates that the flow belongs to the intermediate region ($0.1 \leq Re_p \leq 1000$) in the drag coefficient (C_D) vs. Re_p diagram, where both inertial and viscous forces affect the fluid behaviour. Thus, as mentioned above, the effect of temperature on voidage could result from changes in gas density and viscosity.

One way to assess the importance of these drag forces would be through the terminal velocity. If the viscous forces were to dominate, the drag force on particles would increase, resulting in a decrease of particle terminal velocity. Consequently, at the same superficial gas velocity, more particles would be carried over from the bed, decreasing the axial particle concentration in the reactor. On the other hand, the drag force would decrease if inertial forces dominate the fluid-particle interaction. This would result in an increase of terminal velocity which subsequently leads to a higher solids holdup in the reactor at fixed superficial gas velocity.

54

Calculations of U_t showed that the terminal velocity decreases as the temperature increases as shown in Table 4.1, which results in a lower particle concentration in the riser at elevated temperatures, consistent with Figures 4.1 and 4.2. This suggests that for the experimental conditions of this study, the viscous forces most likely dominate the fluid dynamic behaviour in the DFB. This can also be explained by the fact that as the temperature increases the fluid approaches the Stokes region ($Re_p \leq 0.1$), where the fluid-particle interphase drag is a strong function of viscous forces.

Although the concentration of solids is lower at elevated temperatures, the solids holdup profiles were found to be similar to that at room temperature where the flow regime was fast fluidization for $U_r = 4.0$ m/s and dilute-phase transport at $U_r = 6.0$ m/s.
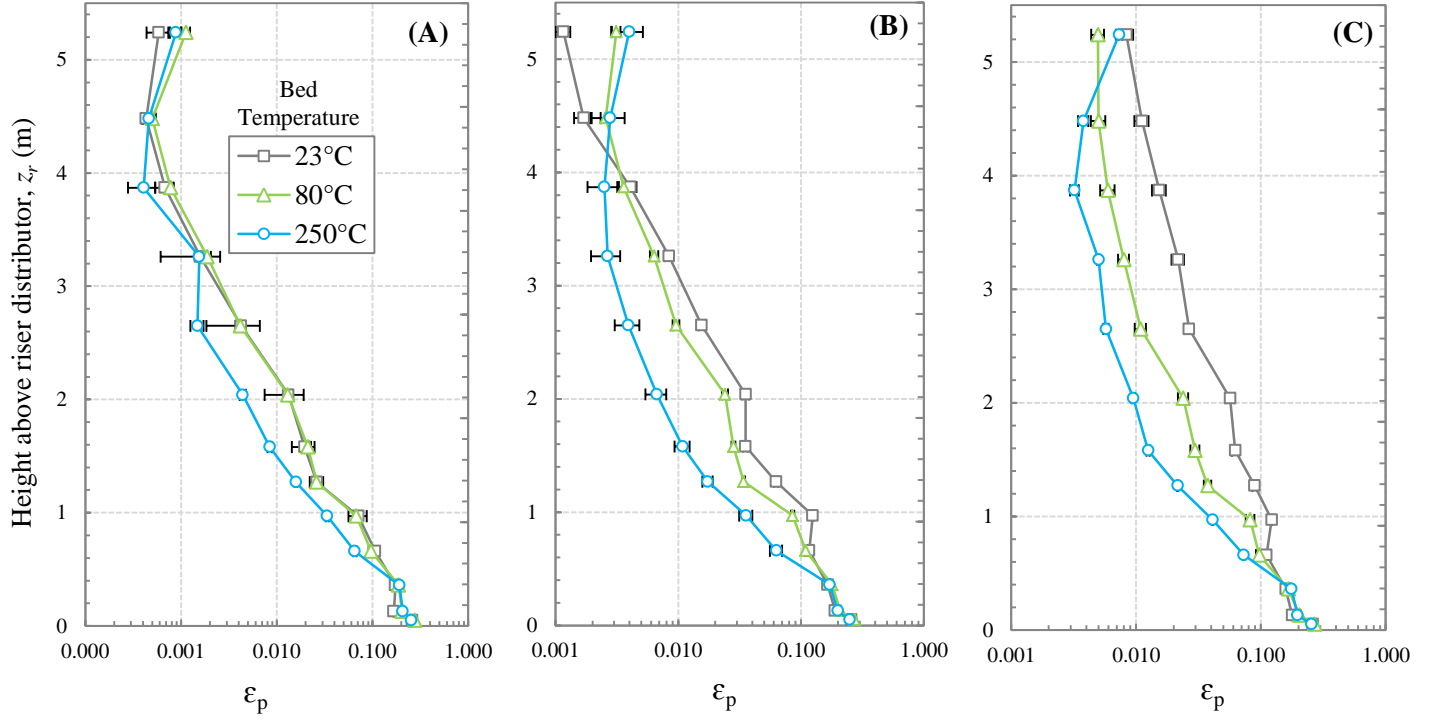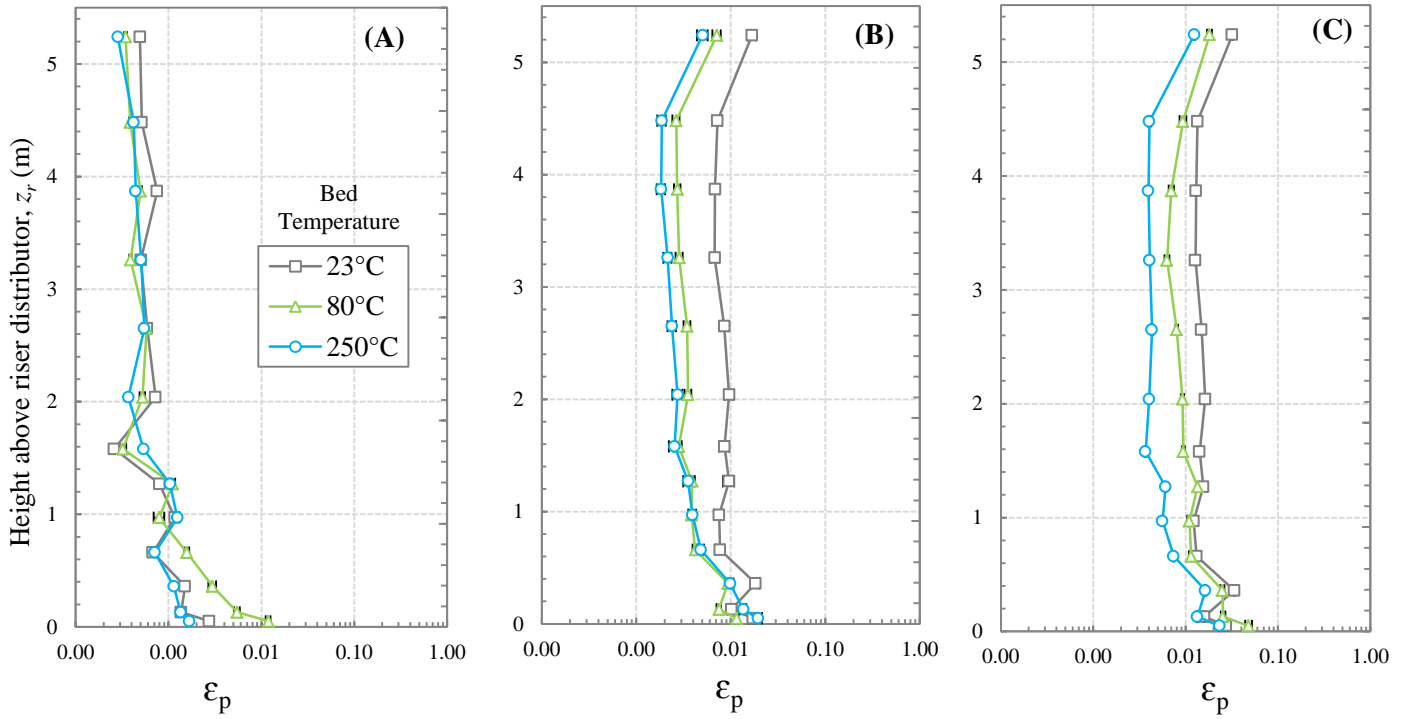

Figure 4.2: Variation of axial solids distribution with temperature at $U_r = 6$ m/s: (A) $U_a = 3U_{mf}$; (B) $U_a = 5U_{mf}$; (C) $U_a = 7U_{mf}$. Error bars correspond to standard error of measurements.

4.2. Solids Circulation Flux

The solids circulation flux was measured in the same manner as in Chapter 3. The solids mass flux (G_s) as a function of operating bed temperature for two riser velocities $U_r = 4.0$ and 6.0 m/s at different U_a/U_{mf} ratios in the loop-seal are given in Figures 4.3 and 4.4. As observed, for a given U_r and U_a/U_{mf} ratio in the loop-seal,

G_s decreased with increasing temperature. G_s was found to be less than 20 kg/m²·s when the temperature increased to 250°C at $U_r = 4.0$ m/s and less than 60 kg/m²·s at $U_r = 6.0$ m/s.
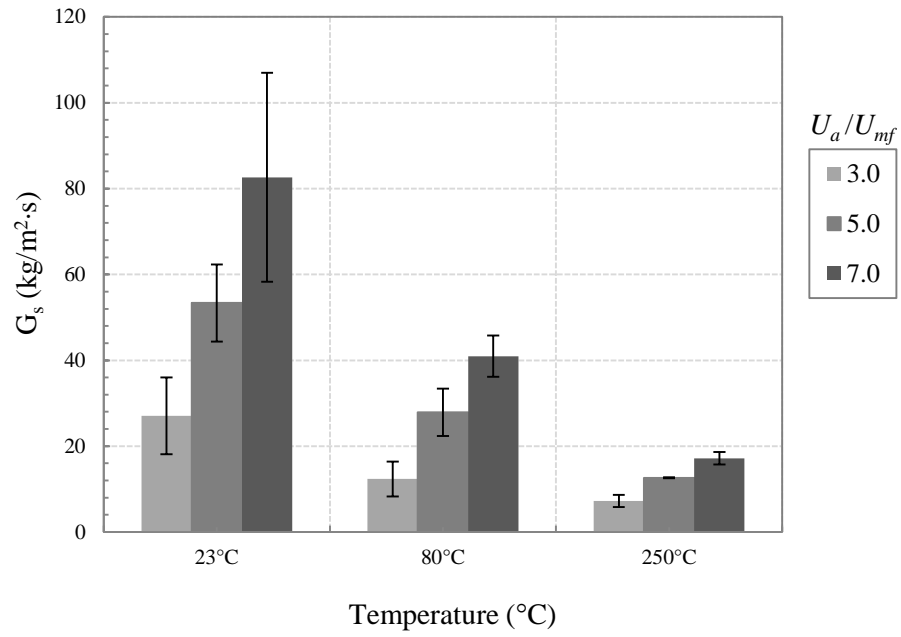
Figure 4.3: Solids circulation flux around DFB for different operating temperatures at $U_r = 4.0$ m/s. Error bars correspond to standard error of measurements.
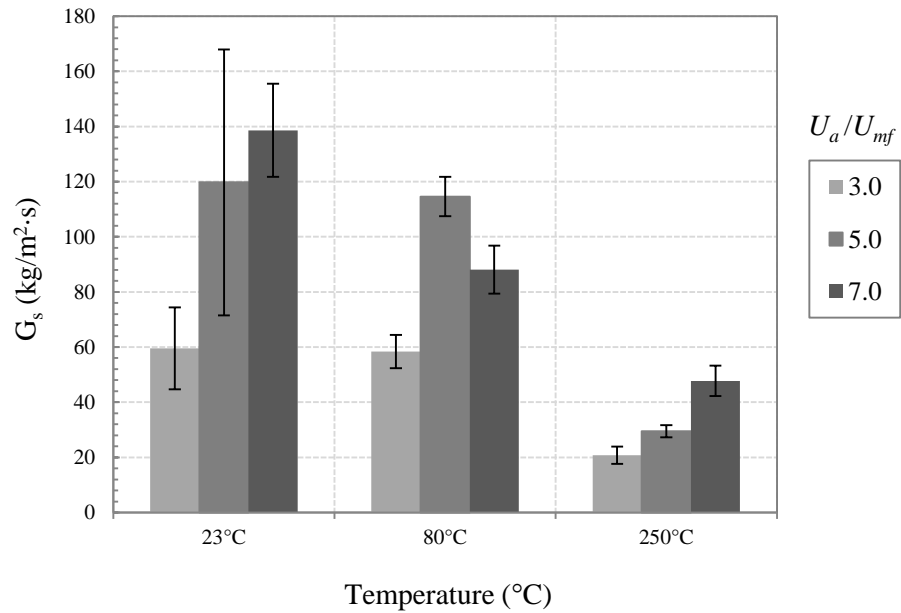
Figure 4.4: Solids circulation flux around DFB for different operating temperatures at $Ur = 6.0$ m/s. Error bars correspond to standard error of measurements.

The decrease of solids circulation flux with increasing temperature might result from the different aeration velocity in the loop-seal (U_a) for every temperature. As temperature increased, U_{mf} became lower, resulting in a lower U_a. This may have also influenced the solids holdup in the system at different temperatures. However, holding U_a constant does not guarantee constant G_s, since G_s is also influenced by gas viscosity and density. In order to prove this, an experiment was conducted at a constant temperature (250°C) and riser gas velocity (U_r=6.0 m/s) to find the effect of maintaining the same velocity (U_a) at 25°C and 250°C (◊) and the same U_a /U_{mf} at 25°C and 250°C (○) (Figure 4.5). No significant difference was found between the experimental conditions, which suggests that solids holdup (ε_p) was primarily influenced by temperature. Note that G_s itself was not measured at this operating condition, so the effect of U_a on G_s could not be determined.

It is also clear from Figures 4.3 and 4.4 that the standard error of the measurements decreased for the higher temperatures. This may be the result of smoother operation, as observed during the collection of solids in the downcomer of the primary cyclone, in contrast to the conditions reported in Section 3.1.
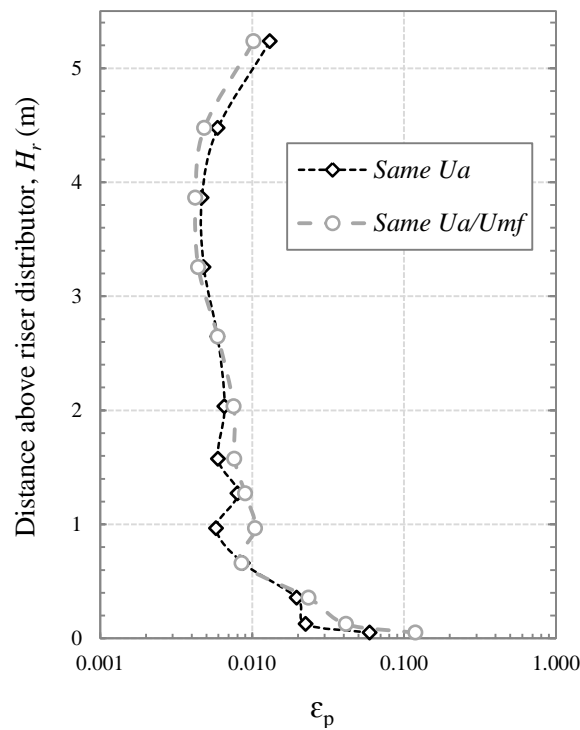
Figure 4.5: Solids holdup in riser at different flows in the loop-seal. U_r = 6.0 m/s, Temperature=250°C.

4.3. Pressure Profile

As in Chapter 3, pressures around the system were recorded during operation at the elevated temperatures. Figures 4.6 and 4.7 present the influence of temperature on the pressure profiles for a fixed U_a/U_{mf} ratio and two riser gas velocities of U_r=4.0 and 6.0 m/s. Other figures for pressure profiles at different U_a/U_{mf} ratios are reported in Appendix A. As observed above, the pressure in the system decreased with increasing operating bed temperature. Similar pressure profiles were obtained for room and elevated temperature conditions, suggesting that the system experienced stable operation at elevated temperatures. As in room temperature operation, the pressure at the bottom of the loop-seal was found to be the highest pressure in the system (point G). The pressure drop along riser (point A-B) decreased with increasing temperature, indicating higher voidage in the riser. Although the pressure at the BFB overflow pipe continues to be the lowest pressure in the system, it was observed that this value increased with increasing temperature (point F). This could be the result of a higher solids inventory in the downcomer connected to the BFB. A higher pressure in the BFB side may be beneficial to minimize gas leakage from the riser to the BFB.
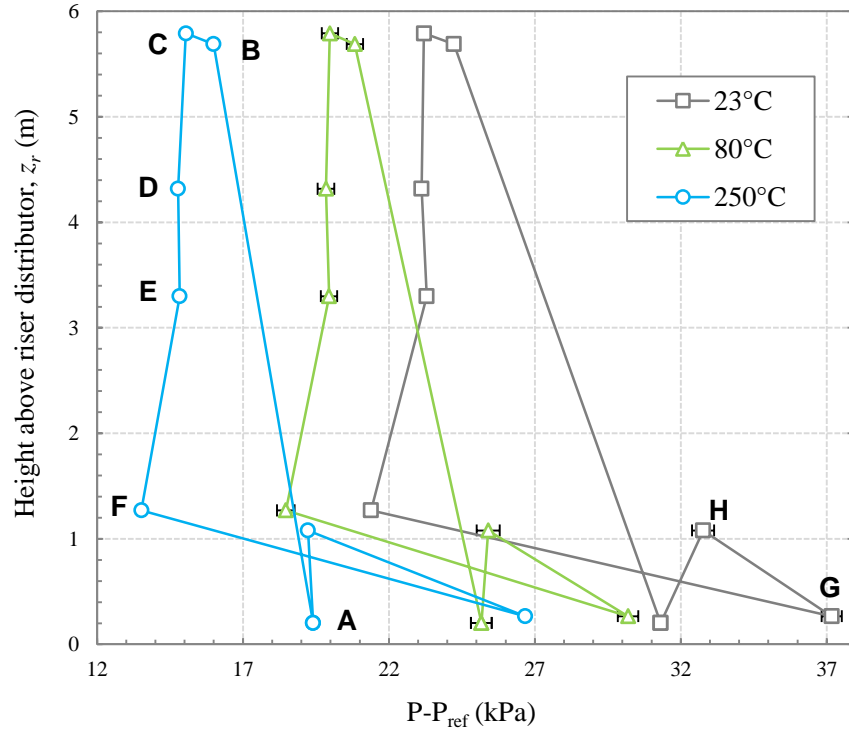
Figure 4.6: Pressure profile for various bed temperatures at U_r= 4.0 m/s and U_a=7U_{mf}, $G_{s\ (23°C)}$ = 83 kg/m^2·s, $G_{s\ (80°C)}$ = 41 kg/m^2·s, $G_{s\ (250°C)}$ = 17 kg/m^2·s. See Figure 3.10 for positions of pressure ports. Error bars correspond to standard error of measurements.
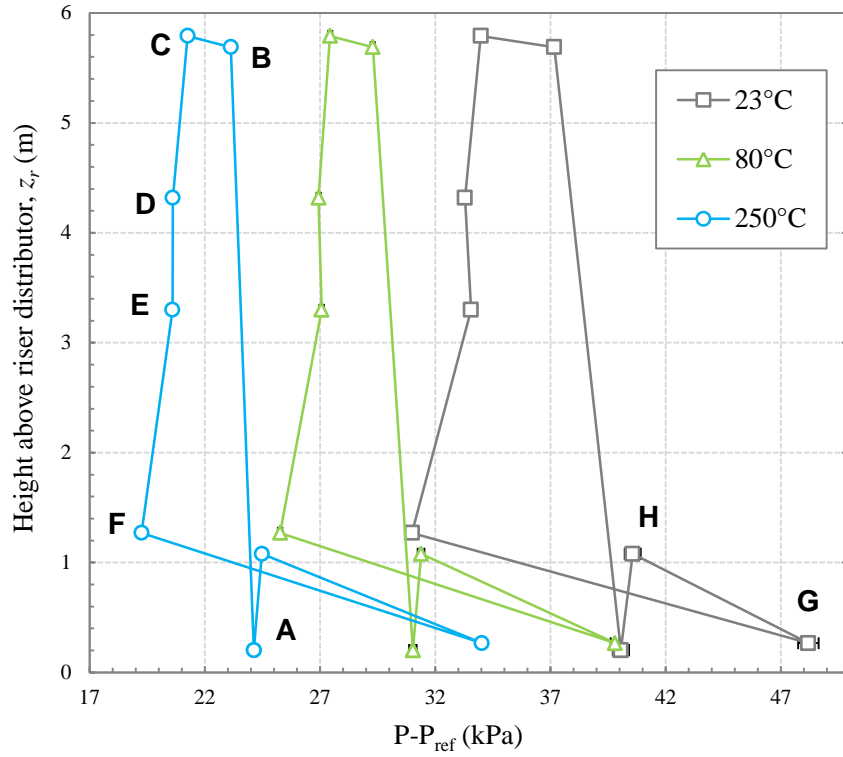
Figure 4.7: Pressure profile for various bed temperatures at U_r= 6.0 m/s and U_a=$7U_{mf}$. $G_{s\ (23°C)}$ = 139 kg/m^2·s, $G_{s\ (80°C)}$ = 88 kg/m^2·s, $G_{s\ (250°C)}$ = 48 kg/m^2·s See Figure 3.10 for positions of pressure ports. Error bars correspond to standard error of measurements.

4.4. Gas Leakage

Minimization of gas leakage between the fluidized beds is important. For this part of the research, gas leakage was measured to find the effect of changing the system temperature. The experiments were conducted following the same procedure as in Section 3.4, with helium as tracer gas and continuous gas injection. Gas leakage was determined based on the concentrations detected at the inlet and outlet of the reactors, depending on whether the gas leakage was being measured from the riser to the BFB or from the BFB to the riser.

As in room temperature experiments, no measurable gas leakage was found from the BFB to the riser side when the temperature was increased to 80°C and to 250°C. This implies that the gas produced in the BFB effectively leaves the reactor through the internal cyclones, and that no gas was carried by the particles over to the riser side. Conversely, gas leakage from the riser to the BFB side could be detected as in the case of room temperature tests. Similarly, analysis of gas samples from different sections of the DFB (Secondary downcomer and loop-seal in Figure 2.1) revealed that gas leaked into the BFB through the standpipe/downcomer of the primary cyclone. However, this leakage was found to decrease with increasing system temperature. Figure 4.10 shows the variation of gas leakage from the riser to the BFB side through the primary downcomer at different U_a /U_{mf} ratios for a given riser gas velocity (U_r = 6.0 m/s). Less than

59

approximately 4.0% of the total product gas in the riser leaked into the BFB for a temperature of 250°C. The decrease of gas leakage from riser to BFB with increasing temperature could be due to the increase of pressure on the BFB side, as shown by the pressure profile in Figure 4.7. Thus, having a high backpressure in the BFB may minimize gas bypassing between riser and the BFB. This could be accomplished by increasing the solids inventory in the downcomer or by imposing a higher pressure at the outlet of the BFB outlet. Another approach to minimize the gas leakage from riser to BFB would be the implementation of a loop-seal in the return leg of the DFB.

Figure 4.8: Gas leakage from riser to BFB for different bed temperatures and U_r = 6.0 m/s. Error bars correspond to standard error of measurements.
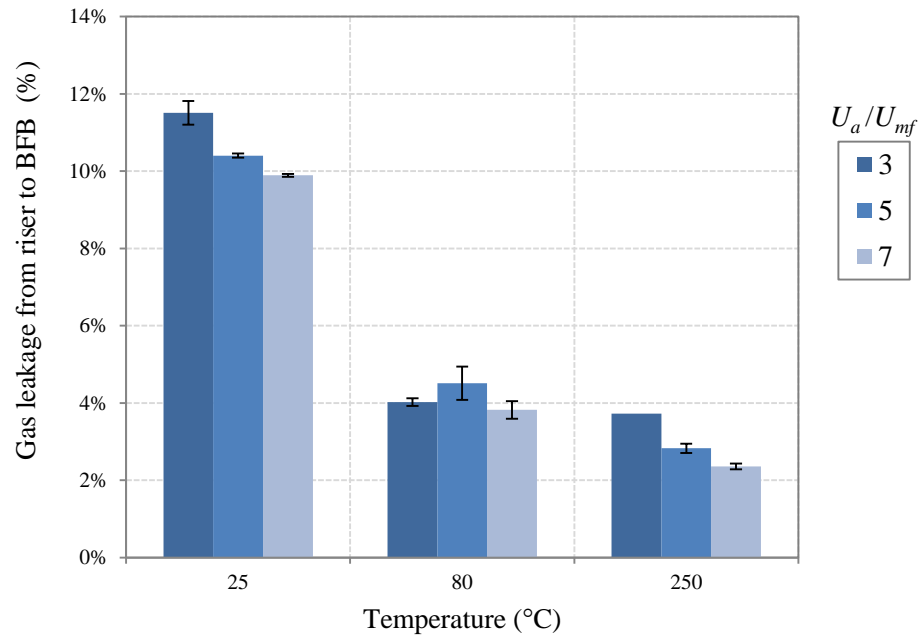
Chapter 5: Conclusions and Final Remarks

5.1. Conclusions

The recent use of Dual Fluidized Beds (DFB) to achieve gasification of carbonaceous fuels and CO_2 capture has led to increased interest in understanding the operation of these reactors and the performance of potential sorbents and bed materials. In this project, the hydrodynamic behaviour of limestone particles in a DFB that comprises a riser and BFB interconnected via a loop-seal has been investigated. The relationship between solids holdup, loop-seal aeration velocity and solids circulation flux was found through a series of experiments performed at atmospheric pressure and temperature. Experiments were also completed to study the effect of scale-up on hydrodynamics by increasing the temperature. Gas leakage between the interconnected fluidized beds and its dependence on pressure balance around the loop is also reported.

The main results of this study can be summarized as follows:

- Stable and successful operation of the DFB employing limestone particles as bed material has been achieved for the operating conditions investigated. At $U_r \geq 5.0$ m/s and $U_a \geq 5U_{mf}$, the system experienced choking flow, influencing the way the solids circulate around the loop and leading to increased pressure fluctuations.

- Riser solids holdup was found to be highly influenced by gas velocity and solids circulation flux. As found by previous researchers, higher riser solids holdups were obtained at lower superficial gas velocity (U_r) and higher solids mass flux. The results revealed that the riser operates under fast-fluidization regime and dilute-phase transport regime, which are the typical flow regimes in CFB combustors.

- As expected, the solids circulation flux is mainly controlled by the aeration velocity in the loop-seal. A positive correlation between riser gas velocity and solids mass flux was also found at $U_r \leq 5.0$ m/s. The increase in riser velocity increases the pressure head in the loop-seal. Thus, solids mass flux is also limited by the pressure head in the loop-seal. Increasing the pressure head increased the solids circulation flux. The solids mass flux ranged between 25 and 139 kg/m$^2\cdot$s with the highest circulation flux obtained at $U_r = 6.0$ m/s and $U_a = 7U_{mf}$.

- Pressure profiles were obtained for different operating conditions. The lowest pressure in the system was found to be at the outlet of BFB and the highest at the bottom of loop-seal. This implies that the loop-seal provides the driving force to move the particles around the loop. Thus, higher pressure

heads (obtained by increasing the length of the vertical section of loop-seal) favours higher solids circulation flux.

- Similar pressure profiles were obtained between the room and elevated temperature experiments. The pressure in the system increased with increasing riser superficial gas velocity and solids mass flux, but decreased with increasing temperature.

- The effect on the hydrodynamics of changes in gas viscosity and density due to varying temperature was assessed. The experiments using the same particles and facility revealed that solids holdup decreased at every height in the riser with increasing temperature except at the bottom of the reactor. However, the effect of temperature was insufficient to change the flow regime in the riser of the DFB for the limited range of conditions studied.

- Although it was not possible to maintain the prescribed solids circulation flux between the room and elevated temperature experiments, the changes in hydrodynamics were attributed to the increase in gas viscosity. Thus, under the operating conditions studied, the viscous forces dominate the gas-solid flow behaviour in the DFB. This implies that the ratio of inertial forces between solid and gas may be omitted from the group of dimensionless parameters and that the simplified form of the scaling laws could be employed to scale-up. However, more experimental data are needed to confirm this.

- Experiments using a gas tracer technique indicated no gas leakage from the BFB to the riser. Conversely, significant gas leakage was found from the riser to the BFB reactor. The main route for the gas to leak into the BFB was the standpipe/downcomer of the primary cyclone. The amount of gas leaking to the BFB was a function of the pressure on the BFB side. Higher pressures in the BFB reduced the gas leakage between the reactors. High pressures in the BFB side could be achieved by increasing the solids inventory, by applying a backpressure at the outlet or by incorporating a loop-seal between the primary cyclone and BFB. Additionally, it was found that high loop-seal aeration velocities help to minimize the gas leakage from the riser to the BFB side.

5.2. Recommendations for Future Work

1- Although the technique used to measure the solids circulation flux could be employed for the experiments in this investigation, this approach provided high errors in the measurements that were independent of the system itself. Therefore, it is recommended to investigate different techniques which could possibly provide more accurate results.

2- As mentioned in the Conclusions, to minimize gas leakage, a higher pressure is needed on the BFB side. Therefore, it is recommended to perform experimental work to test the effect of increasing the pressure in the BFB reactor on the solids circulation flux and the gas leakage between the riser and BFB.

3- Residence Time Distribution (RTD) of solids is another important hydrodynamic parameter for the design of a DFB affecting the reaction performance. Thus, for future work, it is important to measure the solids RTD.

4- Difficulties were encountered to provide the necessary heat at the bottom of the riser and BFB due to absence of preheaters. It is recommended to install preheaters for both columns in order to perform further experiments in the DFB hot unit.

5- The maximum carrying capacity of the gas-solid suspension in the riser could be influenced by temperature. Thus, it is recommended to execute experiments employing a different experimental design that covers a wider range of riser superficial gas velocities and solids circulation flux to evaluate this. In addition, experiments at higher temperatures are necessary to evaluate particle attrition as this may become significant, especially at temperatures where calcination and/or hydration occur, resulting in changes in hydrodynamic behaviour or operational problems.

References

Abanades, J.C., & Alvarez, D. (2003). Conversion Limits in the Reaction of CO_2 with Lime. *Energy & Fuels*, *17*(2), 308–315.

Abba, I. A., Grace, J. R., Bi, H. T., & Thompson, M. L. (2003). Spanning the Flow Regimes: Generic Fluidized-bed Reactor Model. *AIChE Journal*, *49*(7), 1838–1848.

Anthony, E.J., & Granatstein, D.L. (2001). Sulfation Phenomena in Fluidized Bed Combustion Systems. *Progress in Energy and Combustion Science*, *27*(2), 215–236.

Anthony, E.J. (2008). Solid Looping Cycles: A New Technology for Coal Conversion. *Industrial & Engineering Chemistry Research*, *47*(6), 1747–1754.

Alonso, M., Rodríguez, N., González, B., Grasa, G., Murillo, R., & Abanades, J.C. (2010). Carbon Dioxide Capture from Combustion Flue Gases with a Calcium Oxide Chemical Loop. Experimental Results and Process Development. *International Journal of Greenhouse Gas Control, 4(2),* 167–173.

Bai, D., Jin, Y., Yu, Z., & Zhu, J. (1992). The Axial Distribution of the Cross-sectionally Averaged Voidage in Fast Fluidized Beds. *Powder Technology*, *71*, 51–58.

Bai, D., & Kato, K. (1999). Quantitative Estimation of Solids Holdups at Dense and Dilute Regions of Circulating Fluidized Beds. *Powder Technology*, *101*, 183–190.

Bemrose, C.R., & Bridgwater, J. (1987). A Review of Attrition and Attrition Test Methods. *Powder Technology*, *49*, 97–126.

Bi, H.T., Grace, J.R., & Zhu, J.-X. (1993). Types of Choking in Vertical Pneumatic Systems. *International Journal of Multiphase Flow*, *19*(6), 1077–1092.

Bi, H.T., & Zhu, J. (1993). Static Instability of Circulating Fluidized Beds and Concept of High-density Risers. *AIChE Journal*, 39(8), 1272-1279.

Bi, H.T., & Grace, J.R. (1999). Flow Patterns in High-velocity Fluidized Beds and Pneumatic Conveying. *Canadian Journal of Chemical Engineering*, *77*(2), 223–230.

Bi, X.T., & Liu, X. (2010). High Density and High Solids Flux CFB Risers for Steam Gasification of Solid Fuels. *Fuel Processing Technology*, *91*(8), 915–920.

Bidwe, A.R., Varela, G., Nikhil, M., Zieba, M., & Scheffknecht, G. (2011). A Study of Friction Losses in a Circulating Fluidized Bed Riser. *Proceedings of the 21st International Conference on Fluidized Bed Combustion* (pp. 634–640).

Blamey, J., Anthony, E.J., Wang, J., & Fennell, P.S. (2010). The Calcium Looping Cycle for Large-scale CO_2 Capture. *Progress in Energy and Combustion Science*, *36*(2), 260–279.

Charitos, A., Hawthorne, C., Bidwe, A.R., Korovesis, L., Schuster, A., & Scheffknecht, G. (2010). Hydrodynamic Analysis of a 10kW Calcium Looping Dual Fluidized Bed for Post-combustion CO_2 Capture. *Powder Technology*, *200*(3), 117–127.

Chen, Z., Grace, J.R., & Jim Lim, C. (2008). Limestone Particle Attrition and Size Distribution in a Small Circulating Fluidized Bed. *Fuel*, *87*(7), 1360–1371.

Coppola, A., Montagnaro, F., Salatino, P., & Scala, F. (2012). Fluidized Bed Calcium Looping: The Effect of SO_2 on Sorbent Attrition and CO_2 Capture Capacity. *Chemical Engineering Journal*, *207-208*, 445–449.

Coppola, A., Montagnaro, F., Salatino, P., & Scala, F. (2012). Limestone Attrition during Fluidized Bed Calcium Looping Cycles for CO_2 capture : the effect of SO_2. *XXXV Meeting of Italian Section of the Combustion Institute* (Vol. Session V, pp. 1–6). Milan, Italy.

Corella, J., Toledo, J.M., & Molina, G. (2007). A Review on Dual Fluidized-Bed Biomass Gasifiers. *Industrial & Engineering Chemistry Research*, *46*(21), 6831–6839.

Dean, C.C., Blamey, J., Florin, N.H., Al-Jeboori, M.J., & Fennell, P.S. (2011). The Calcium Looping Cycle for CO_2 Capture from Power Generation, Cement Manufacture and Hydrogen Production. *Chemical Engineering Research and Design*, *89*(6), 836–855.

Fan, L.-S., Zeng, L., Wang, W., & Luo, S. (2012). Chemical Looping Processes for CO_2 Capture and Carbonaceous Fuel Conversion – Prospect and Opportunity. *Energy & Environmental Science*, *5*(6), 7254.

Fang, F., Li, Z.S., & Cai, N.S. (2010). Design and Cold Mode Experiment of Dual Bubbling Fluidized Bed Reactors for Multiple CCR Cycles. *20th International Conference on Fluidized Bed Combustion*, Vol. 3, pp. 533–539.

Fennell, P.S., Pacciani, R., Dennis, J.S., Davidson, J. F., & Hayhurst, A. N. (2007). The Effects of Repeated Cycles of Calcination and Carbonation on a Variety of Different Limestones, as Measured in a Hot Fluidized Bed of Sand. *Energy*, *31*(1), 2072–2081.

Fushimi, C., Guan, G., Nakamura, Y., Ishizuka, M., & Tsutsumi, A. (2011). Hydrodynamic Characteristics of a Large-scale Triple-bed combined Circulating Fluidized Bed. *Powder Technology*, *209*(1-3), 1–8.

Geldart, D. (1973). Types of Gas Fluidization. *Powder Technology*, *7*, 285–292.

Glicksman, R. (1984). Scaling Relationships for Fluidized Beds. *Chemical Engineering Science*, *39*(9), 1373–1379.

Glicksman, L. (1994). Dynamic Similarity in Fluidization. *International Journal of Multiphase Flow*, *20*(94), 331–386.

Grace, J.R. (1982). Fluidized-Bed Hydrodynamics. Chapter 8.1 in G. Hetsroni (Ed.), *Handbook of Multiphase Systems*. Washington D.C. Hemisphere Publishing Corporation.

Grace, J.R. (1990). High Velocity Fluidized Bed Reactors. *Chemical Engineering Science*, *45*(8), 1953–1966.

Grace, J. (2010). A Perspective on Development of Novel Fluidized Bed Processes for a More Sustainable Global Future. In S. D. Kim, Y. Kang, J. K. Lee, & Y. C. Seo (Eds.), *13th International Conference on Fluidization* (p. Art. 6. 1–8). Gyeong-ju, Korea: ECI Digital Archives.

Grieco, E., & Marmo, L. (2008). A Model for the Pressure Balance of a Low Density Circulating Fluidized Bed. *Chemical Engineering Journal*, *140*(1-3), 414–423.

Guan, G., Fushimi, C., & Tsutsumi, A. (2010). Prediction of Flow Behavior of the Riser in a Novel High Solids Flux Circulating Fluidized Bed for Steam Gasification of Coal or Biomass. *Chemical Engineering Journal*, *164*(1), 221–229.

Gupta, M., Coyle, I., & Thambimuthu, K. (2003). CO_2 Capture Technologies and Opportunities in Canada. Calgary, Alberta, Canada: CANMET Energy Technology Centre, Natural Resources Canada.

Han, C., & Harrison, D.P. (1994). Simultaneous Shift Reaction and Carbon Dioxide Separation for the Direct Production of Hydrogen. *Chemical Engineering Science*, *49*(24), 5875–5883.

Integrated CO_2 Network (ICO$_2$N). (2009). *Carbon Dioxide Capture and Storage, a Canadian Clean Energy Oportunity.* (pp. 1–20). Calgary, Canada. Retrieved on August 15th, 2013 from http://www.ico2n.com/wp-content/uploads/2010/07/ICO2N-Report_09_final2.pdf

Jia, L., Hughes, R., Lu, D., Anthony, E. J., & Lau, I. (2007). Attrition of Calcining Limestones in Circulating Fluidized-Bed Systems. *Industrial & Engineering Chemistry Research*, *46*(15), 5199–5209.

Johansson, E., Lyngfelt, A., Mattisson, T., & Johnsson, F. (2003). Gas Leakage Measurements in a Cold Model of an Interconnected Fluidized Bed for Chemical-looping Combustion. *Powder Technology*, *134*(3), 210–217.

Kaiser, S., Löffler, G., Bosch, K., & Hofbauer, H. (2003). Hydrodynamics of a Dual Fluidized Bed Gasifier. Part II: Simulation of Solid Circulation Rate, Pressure Loop and Stability. *Chemical Engineering Science*, *58*(18), 4215–4223.

Karmakar, M.K., & Datta, A.B. (2010). Hydrodynamics of a Dual Fluidized Bed Gasifier. *Advanced Powder Technology*, *21*(5), 521–528.

Kehlenbeck, R., Yates, J., Di Felice, R., Hofbauer, H., & Rauch, R. (2001). Novel Scaling Parameter for Circulating Fluidized Beds. *AIChE Journal*, *47*(3), 582–589.

Kim, S.W., Namkung, W., & Kim, S.D. (1999). Solids Flow Characteristics in Loop-seal of a Circulating Fluidized Bed. *Korean Journal of Chemical Engineering*, *16*(1), 82–88.

Kim, Sung Won., Kim, Sang Done & Lee, Dong Hyun (2002). Pressure Balance Model for Circulating Fluidized Beds with a Loop-seal. *Industrial & Engineering Chemistry Research*, *4*(20), 4949-4956.

Knowlton, T.M. (2003). Standpipes and Nonmechanical Valves. Chapter 21 in W.-C. Yang (Ed.), *Handbook of Fluidization and Fluid Particle Systems*. New York: Marcel Dekker, Inc. Press 2003.

Kronberger, B., Beal, C., Morin, J.-X., & Hofbauer, H. (2004). Design, Hydrodynamic Testing and Scale-up Recommendations of a Conceptual Large-scale Chemical-looping Combustion Power Plant. *3rd Conference on Sequestration*. Alexandria, USA.

Kunii, D., & Levenspiel, O. (1991). *Fluidization Engineering*. Boston: Butterworth-Heinemann.

Kuramoto, K., Fujimoto, S., Morita, A., Shibano, S., Suzuki, Y., Hatano, H., Shi-Ying, L., et al. (2003). Repetitive Carbonation−Calcination Reactions of Ca-Based Sorbents for Efficient CO_2 Sorption at Elevated Temperatures and Pressures. *Industrial & Engineering Chemistry Research*, *42*(5), 975–981.

Lackermeier, U., & Werther, J. (2002). Flow Phenomena in the Exit Zone of a Circulating Fluidized Bed. *Chemical Engineering and Processing*, *41*, 771–783.

Lei, H., & Horio, M. (1998). A Comprehensive Pressure Balance Model of Circulating Fluidized Beds. *Journal of Chemical Engineering of Japan*, *31*(1), 83–94.

Lim, K.S., Zhu, J.X., & Grace, J.R. (1995). Hydrodynamics of Gas-solid Fluidization. *International Journal of Multiphase Flow*, *21*, 141–193.

Löffler, G., Kaiser, S., Bosch, K., & Hofbauer, H. (2003). Hydrodynamics of a Dual Fluidized-bed Gasifier— Part I: Simulation of a Riser with Gas Injection and Diffuser. *Chemical Engineering Science*, *58*(18), 4197–4213.

Lu, D.Y., Hughes, R.W., & Anthony, E.J. (2008). Ca-based Sorbent Looping Combustion for CO_2 Capture in Pilot-scale Dual Fluidized Beds. *Fuel Processing Technology*, *89*, 1386–1395.

Manovic, V., & Anthony, E.J. (2007). Steam Reactivation of Spent CaO-based Sorbent for Multiple CO_2 Capture Cycles. *Environmental Science & Technology*, *41*(4), 1420–1425.

Martínez, A., Lisbona, P., Lara, Y., & Romeo, L. M. (2010). Carbonate Looping Cycle for CO_2 Capture : Hydrodynamic of Complex CFB Systems. *Energy Procedia*, *00*, 0–6.

Mastellone, M.L., & Arena, U. (1999). The Effect of Particle Size and Density on Solids Distribution Along the Riser of a Circulating Fluidized Bed. *Chemical Engineering Science*, *54*, 5383–5391.

Montagnaro, F., Salatino, P., & Scala, F. (2010). The Influence of Temperature on Limestone Sulfation and Attrition Under Fluidized Bed Combustion Conditions. *Experimental Thermal and Fluid Science*, *34*(3), 352–358.

Nguyen, T.D.B., Seo, M.W., Lim, Y.-I., Song, B.-H., & Kim, S.-D. (2012). CFD Simulation with Experiments in a Dual Circulating Fluidized Bed Gasifier. *Computers & Chemical Engineering*, *36*, 48–56.

Pacciani, R., Müller, C.R., Davidson, J.F., Dennis, J.S., & Hayhurst, A. N. (2008). Synthetic Ca-based Solid Sorbents Suitable for Capturing CO_2 in a Fluidized Bed. *Canadian Journal of Chemical Engineering*, *86*(3), 356–366.

Pfeifer, C., Rauch, R., Hofbauer, H., Świerczyński, D., & Courson, C. (2004). Hydrogen-rich Gas Production with a Ni-Catalyst in a Dual Fluidized Bed Biomass Gasifier. *Science in Thermal and Chemical Biomass Conversion*, Victoria, Canada, August 30-September 2.

Pfeifer, C., Puchner, B., & Hofbauer, H. (2007). In-Situ CO_2 -Absorption in a Dual Fluidized Bed Biomass Steam Gasifier to Produce a Hydrogen Rich Syngas. *International Journal of Chemical Reactor Engineering*, *5*(A9), 1–13.

Pfeifer, C., Koppatz, S., & Hofbauer, H. (2011). Steam Gasification of Various Feedstocks at a Dual Fluidised Bed Gasifier: Impacts of Operation Conditions and Bed Materials. *Biomass Conversion and Biorefinery*, *1*(1), 39–53.

Pfeifer, C., Schmid, J.C., Pröll, T., & Hofbauer, H. (2011). Next Generation Biomass Gasifier. *19th European Biomass Conference and Exhibition* (pp. 1–7). Berlin, Germany.

Pugsley, T.S., & Berruti, F. (1996). A Predictive Hydrodynamic Model for Circulating Fluidized Bed Risers. *Powder Technology*, *89*, 57–69.

Pugsley, T., Lapointe, D., Hirschberg, B., & Werther, J. (1997). Exit Effects in Circulating Fluidized Bed Risers. *The Canadian Journal of Chemical Engineering*, *75*(6), 1001–1010.

Reyes-Ramirez, P. (2012). *Standard Operating Procedure of Chemical Looping Hot Unit,* Internal report, 42 pages. UBC, Fluidization Research Centre. Department of Chemical and Biological Engineering. Vancouver, Canada.

Rhodes, M.J., & Geldart, D. (1987). A Model for the Circulating Fluidized Bed. *Powder Technology*, *53*(3), 155-162.

Rodriguez, N., Alonso, M., & Abanades, J.C. (2011). Experimental Investigation of a Circulating Fluidized-bed reactor to capture CO_2 with CaO. *AIChE Journal*, *57*(5), 1356–1366.

Ryu, H.-J., Park, Y.-C., Jo, S.-H., & Park, M.-H. (2009). Development of Novel Two-interconnected Fluidized Bed System. *Korean Journal of Chemical Engineering*, *25*(5), 1178–1183.

Ryu, H.-J., Lee, S., Park, Y.C., & Park, M.-H. (2007). Solid Circulation Rate and Gas Leakage Measurements in an Interconnected Bubbling Fluidized Beds. *World Academy of Science, Engineering and Technology*, *28*, 169–174.

Saastamoinen, J., Pikkarainen, T., Tourunen, A., Räsänen, M., & Jäntti, T. (2008). Model of Fragmentation of Limestone Particles During Thermal Shock and Calcination in Fluidised Beds. *Powder Technology*, *187*(3), 244–251.

Saastamoinen, J.J., Shimizu, T., & Tourunen, A. (2010). Effect of Attrition on Particle Size Distribution and SO_2 Capture in Fluidized Bed Combustion Under High CO_2 Partial Pressure Conditions. *Chemical Engineering Science*, *65*(1), 550–555.

Salvador, C., Lu, D., Anthony, E.J., & Abanades, J.C. (2003). Enhancement of CaO for CO_2 Capture in an FBC Environment. *Chemical Engineering Journal*, *96*(1-3), 187–195.

Scala, F. (2000). Attrition of Sorbents During Fluidized Bed Calcination and Sulphation. *Powder Technology*, *107*(1-2), 153–167.

Schmid, J.C., Pfeifer, C., Kitzler, H., Pröll, T., & Hofbauer, H. (2011). A New Dual Fluidized Bed Gasifier Design for Improved In Situ Conversion of Hydrocarbons. *Int. Conf. on Polygeneration Strategies (ICPS)*.

Seo, M.W., Nguyen, T.D.B., Lim, Y.I, Kim, S.D., Park, S., Song, B.H., & Kim, Y.J. (2011). Solid Circulation and Loop-seal Characteristics of a Dual Circulating Fluidized Bed: Experiments and CFD Simulation. *Chemical Engineering Journal*, *168*(2), 803–811.

Soukup, G., Pfeifer, C., Kreuzeder, A., & Hofbauer, H. (2009). In Situ CO_2 Capture in a Dual Fluidized Bed Biomass Steam Gasifier - Bed Material and Fuel Variation. *Chemical Engineering & Technology*, *32*(3), 348–354.

Stewart, P. S. B., & Davidson, J. F. (1967). Slug Flow in Fluidised Bed. *Powder Technology*, *1*(2), 61–80.

Sung, Y. K., Song, J.H., Bang, B.R., Yu, T.U., & Lee, U.Do. (2010). A Hydrodynamic Characteristic of a Dual Fluidized Bed Gasification. *20th International Conference on Fluidized Bed Combustion* (pp. 664–668).

Van der Meer, E.H., Thorpe, R.B., & Davidson, J.F. (1999). Dimensionless Groups for Practicable Similarity of Circulating Fluidised Beds. *Chemical Engineering Science*, *54*, 5369–5376.

Wen, C.Y., & Chen, L.H. (1982). Fluidized Bed Freeboard Phenomena, Entrainment and Elutriation. *AIChE Journal*, *28*, 117–128.

Wen, C.Y., & Yu, Y.H. (1966). A Generalized Method for Predicting the Minimum Fluidization Velocity. *AIChE Journal*, *12*(3), 610–612.

Wu, Y., Blamey, J., Anthony, E.J., & Fennell, P.S. (2010). Morphological Changes of Limestone Sorbent Particles during Carbonation/Calcination Looping Cycles in a Thermogravimetric Analyzer (TGA) and Reactivation with Steam. *Energy & Fuels*, *24*(4), 2768–2776.

Xu, M. (2010). *Chemical Looping Combustion : Cold Model Hydrodynamics and Modeling of Methane Combustion*. Chemical and Biological Engineering Ph.D. Dissertation. University of British Columbia.

Xu, G., Murakami, T., Suda, T., Matsuzawa, Y., & Tani, H. (2006). The Superior Technical Choice for Dual Fluidized Bed Gasification. *Industrial & Engineering Chemistry Research*, *45*(7), 2281–2286.

Xu, G., Nomura, K., Gao, S., & Kato, K. (2001). More Fundamentals of Dilute Suspension Collapse and Choking for Vertical Conveying Systems. *AIChE Journal*, *47*(10), 2177–2196.

Xu, G., Nomura, K., Nakagawa, N., & Kato, K. (1999). Collapse of Dilute Suspension in Different Circulating Fluidized Bed Risers with Respect to Different Particles. *Canadian Journal of Chemical Engineering*, *77*(2), 238–246.

Yang, W.-C. (2003). Bubbling Fluidized Beds. In W.-C. Yang (Ed.), *Handbook of Fluidization and Fluid Particle Systems*. New York: Marcel Dekker, Inc. Press 2003.

Yao, X., Zhang, H., Yang, H., Liu, Q., Wang, J., & Yue, G. (2010). An Experimental Study on the Primary Fragmentation and Attrition of Limestones in a Fluidized Bed. *Fuel Processing Technology*, *91*(9), 1119–1124.

Yinghai, W., Manovic, V., He, I., & Anthony, E.J. (2012). Modified Lime-based Pellet Sorbents for High-temperature CO_2 Capture : Reactivity and Attrition Behavior. *Fuel*, *96*, 454–461.

Zero Emissions Platform. (2009). *Capturing and Storing CO_2-The Hard Facts Behind CCS*. Retrieved on May 8th, 2013 from http://www.zeroemissionsplatform.eu/library/publication/86-the-hard-facts-behind-ccs.html

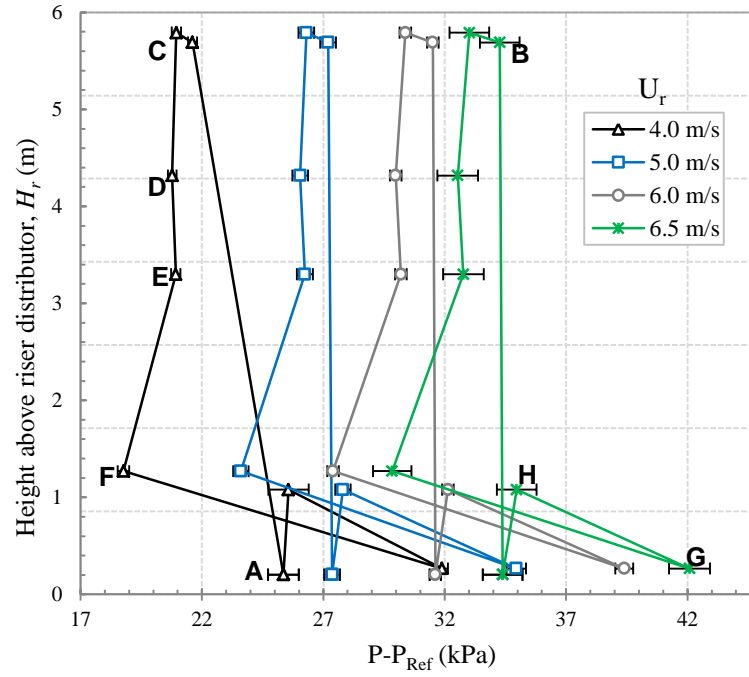# Apendix A: Additional Experimental Results

Pressure Profiles

Figure A.1: Pressure profiles for different riser fluidization velocities and U_a = $3U_{mf}$, U_{BFB} = 0.24 m/s. Error bars correspond to standard error of measurements.
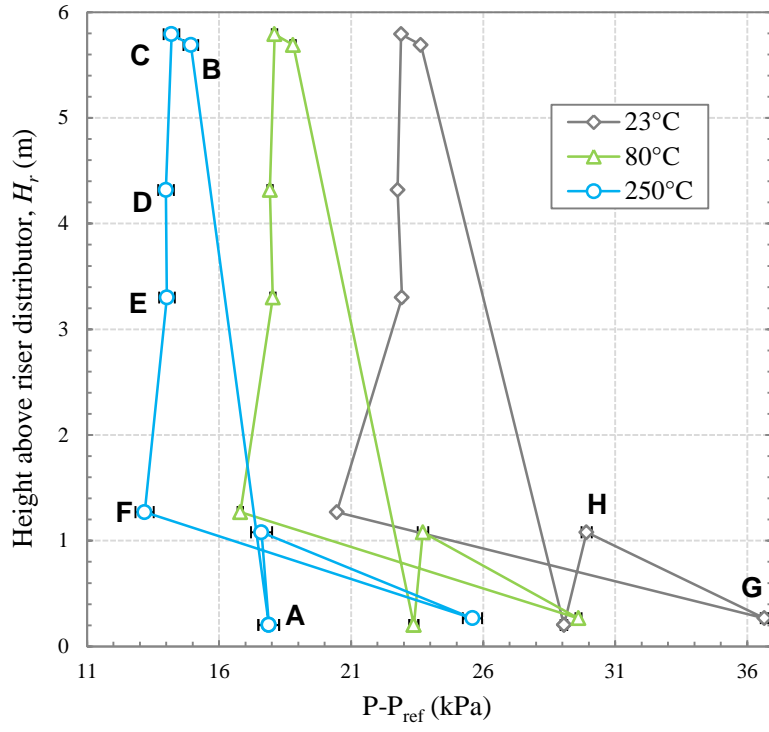
Figure A.2: Pressure profiles for various bed temperatures and $U_r = 4.0$ m/s and $U_a = 5U_{mf}$. Error bars correspond to standard error of measurements
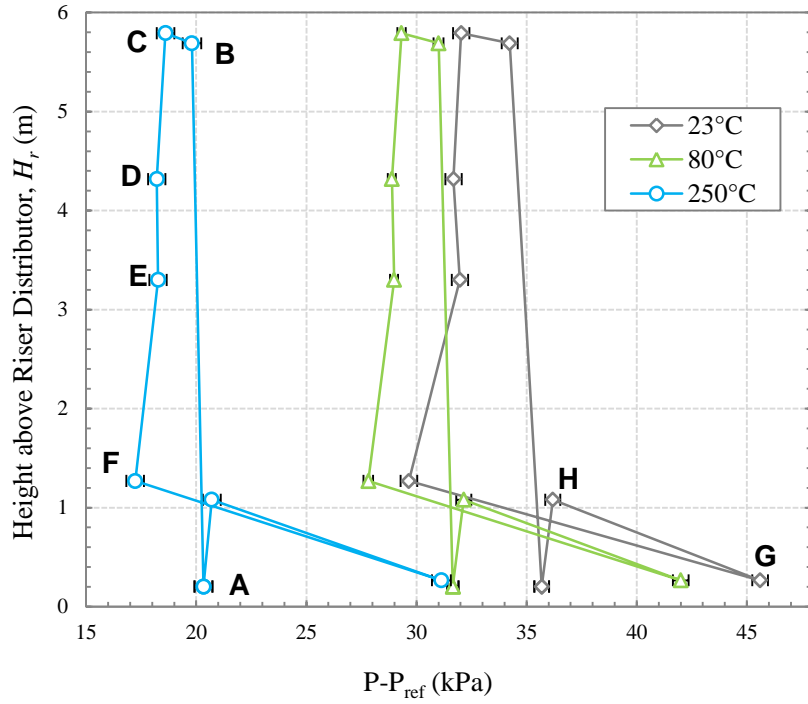

Figure A.3: Pressure profile for various bed temperatures at $U_r = 6.0$ m/s and $U_a = 5U_{mf}$. Error bars correspond to standard error of measurements

Evaluation of Material Loss and Particle Size Distribution of Bed Material During Operation

It is of great importance to evaluate the attrition and elutriation of potential CO_2 capture sorbents, since these phenomena may affect the hydrodynamics, reaction performance and process economics. As mentioned in Chapter I, one of the main drawbacks of using limestone as bed material for gasification with CO_2 capture is the high extent of attrition that the material undergoes when subjected to chemical, thermal and mechanical stresses, all of which are encountered in high velocity fluidized beds.

This section reports on the attrition of limestone during the operation of the DFB in a cold and warm environment. The attrition of limestone has been analyzed based on changes in Particle Size Distribution (PSD), mean particle diameter of bed material and material loss. Some Scanning Electron Microscope (SEM) images of samples of bed material are also presented to analyze the degradation and changes in particle shape and roughness.

Material Loss

The elutriation of bed material is a consequence of attrition. Elutriation is highly dependent on operating conditions such as superficial gas velocities, temperature, solids mass flux and equipment performance (cyclone efficiency). The relationship between operating conditions and material loss could not be determined since it was not possible to isolate the conditions in the DFB. However, material accumulated in bag filter was often measured during the experiments to track changes in TSI.

The material loss was measured by collecting the particles elutriated from the bed during specific time intervals. A bag filter made of fiberglass (FB700) located at the exit of the riser was designed and installed at the beginning of the experiments to facilitate the collection of elutriated material. Figure 2.6 of Chapter 2 shows the downstream filter. A pipe cup at the bottom of the filter was removed to drain the material accumulated in the bottom section. Additionally, a backpressure line (550 kPa) of air was used to further remove as much limestone as possible from the filter bag to increase accuracy of the measurements. The collected particles were weighted in a 0.01g precision scale and samples were subsequently taken for PSD analysis. The collected material was not returned to the system since it was assumed that these particles were going to be later removed by the gas from the DFB. Instead, fresh limestone was added to the system after every measurement to minimize changes of material inventory. Figure A.4 shows the material loss vs. time. As expected, the highest material loss was found during the first 12 hours of operation, probably due to the removal of particle edges by abrasion and initial removal of a fraction of small particles from roughness elements on the particles. Material loss decreased with time to nearly a constant value, but increased again after 111 hours of operation. The increase in the amount of particles elutriated from the system probably resulted from fresh material abrasion and initiation of particle fragmentation. The initiation of experiments in

a hot environment could have also influenced the material loss by elutriation, as shown in Zone 7 and 8 of Figure A.4. Zones in Figure A.4 represent the time intervals where material loss was quantified.
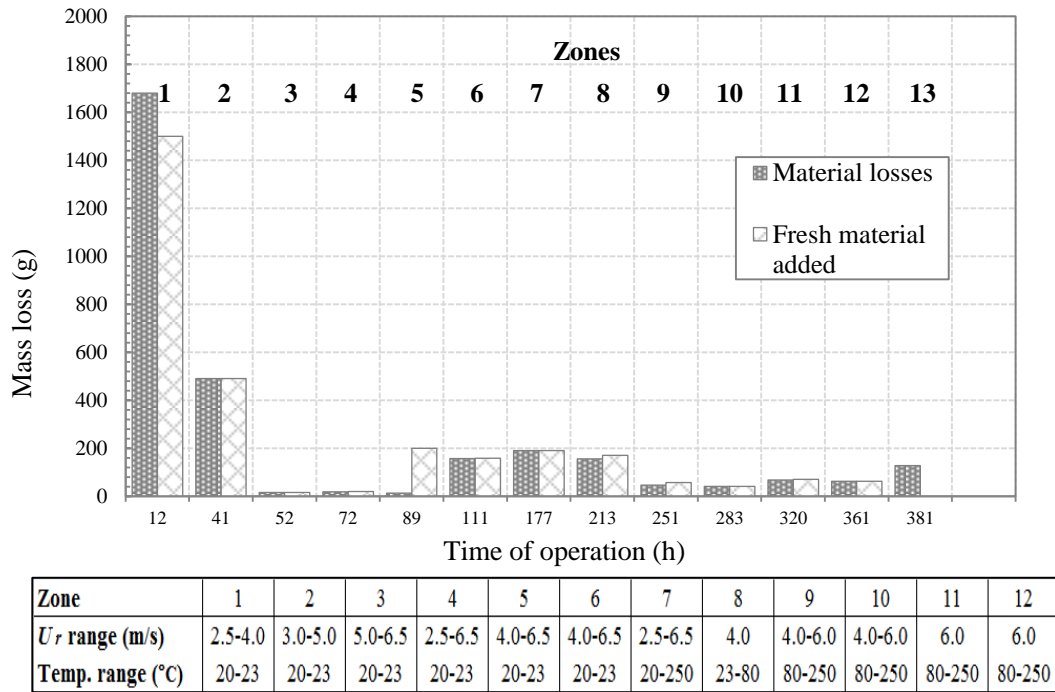

Zone	1	2	3	4	5	6	7	8	9	10	11	12
U_r range (m/s)	2.5-4.0	3.0-5.0	5.0-6.5	2.5-6.5	4.0-6.5	4.0-6.5	2.5-6.5	4.0	4.0-6.0	4.0-6.0	6.0	6.0
Temp. range (°C)	20-23	20-23	20-23	20-23	20-23	20-23	20-250	23-80	80-250	80-250	80-250	80-250

Figure A.4: Material loss during the operation of the DFB.

During the operation of the DFB, it was observed that some particles were leaving the system with the gas via the internal cyclones of the BFB. The BFB outlet was connected directly to the ventilation system, and no filter was available to collect the elutriated material from this reactor. Thus, no accurate quantification of this material was possible during the operation of the DFB. However, the BFB elutriated material was removed from the ventilation system at three different times during the experiments. The results are shown in Figure A.5.
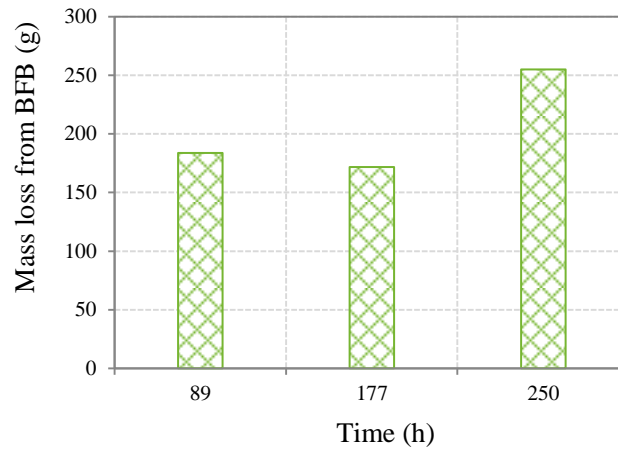
Figure A.5: Elutriated particles from BFB

Considering the material losses due to elutriation from the BFB and riser, solids circulation flux measurement and the material removed for PSD analysis, it was estimated that approximately 11.5% of the initial load (12 kg) was lost due to elutriation after 381 total hours of operation at riser superficial velocities of 2.5 to 6.5 m/s and temperature of 23 and 250°C.

Particle Size Distribution Bed and Elutriated Material

To study the change in PSD of limestone particles during the operation of the DFB, solids samples were taken from the bed at different time intervals during the solids mass flux measurement experiments (from the downcomer of the primary cyclone) for the same operating conditions i.e. $U_r = 6.0$ m/s and $U_a=5U_{mf}$. Samples of bed material were collected from the downcomer assuming that all particles were completely mixed in the system. Three samples of 10 g each were taken from the bulk of solids collected by employing the cone and quartering technique in order to increase sample representativeness. Samples were analyzed by a dry laser diffraction technique employing a Mastersizer2000 provided by *Malvern Instruments Inc*. A Scirocco 200 apparatus attached to the main unit was used as the dry powder disperser. Figure A.6 shows the average cumulative undersize volume fraction and particle size frequency distribution curves at different time intervals during the operation. As can be seen the distribution shifted towards a larger particle size. During the first 41 hours of operation, a shift in PSD is seen accompanied by a generation of fraction of smaller particles ranging between 50-100 µm that were not elutriated from the bed (Figure A.7B). The appearance of particles of smaller size could be the result of initial particle surface abrasion. Initial fragmentation may have also occurred during the first 41 hours of operation, leading to elutriation of particles of size comparable to that of the original particles. Consequently, the PSD shifted to a higher particle size after 41 hours of operation as seen in Figure A.6B. The cumulative undersize curve and the particle size frequency distribution of elutriated particles are presented in Figure A.7. Note that 83% of the elutriated material correspond to particles of sizes $d_p \leq 17$ µm, with the remainder percentage consisting of particles in the range of 40-630µm.
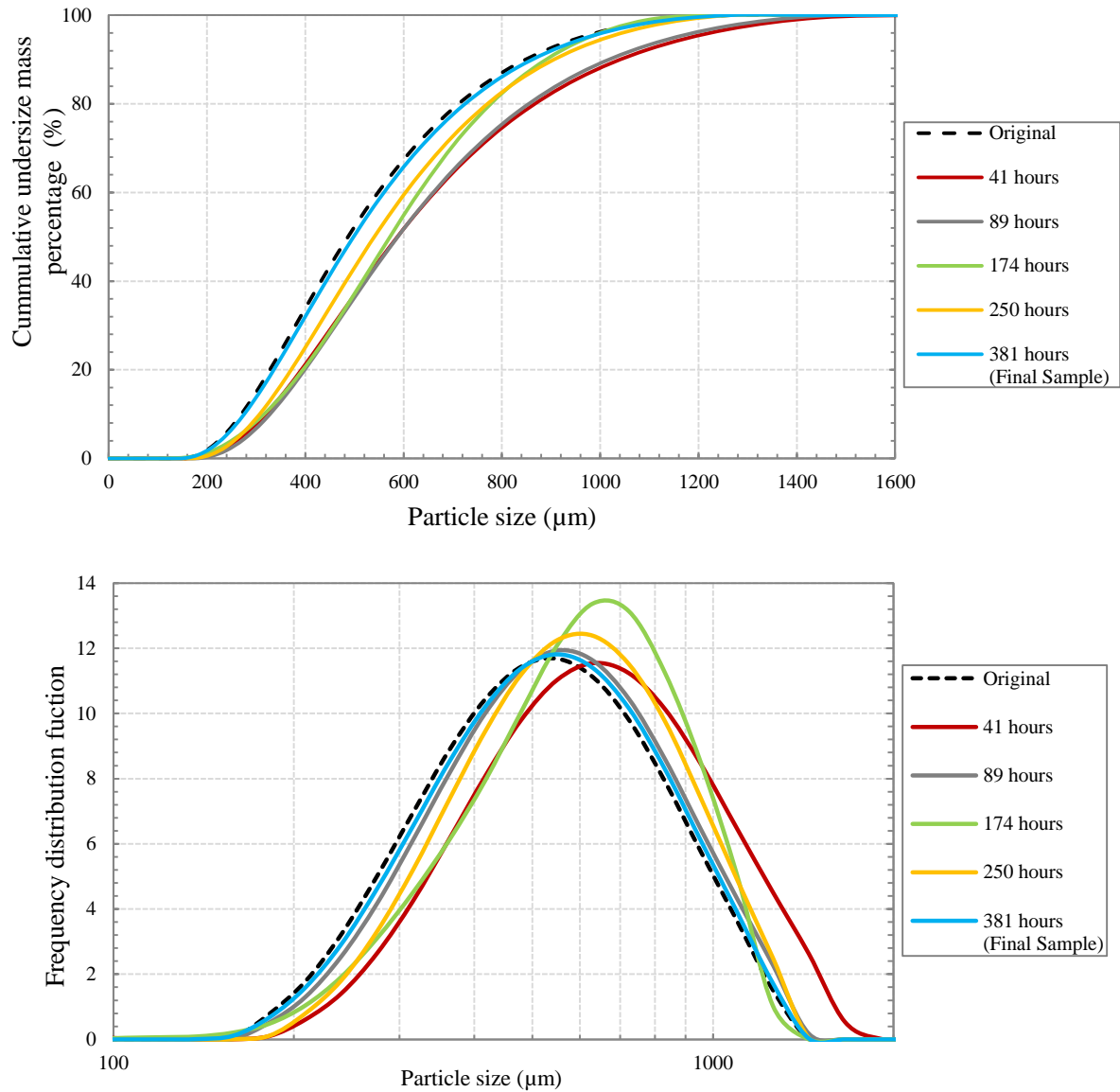
74

Figure A.6: Particle size distribution of limestone particles at different times during operation. (A) Cumulative undersize distribution; (B) Distribution frequency curve.

A slight change in particle size distribution of the bed material is seen after 89 hours of operation. The fraction of particles under 158 μm is no longer present in the distribution after 89 h, whereas particles larger than 630 μm become smaller in size. This is the result of elutriation of fines that remained in the bed after the probable initial attrition by abrasion, and the increasing fragmentation of the bigger mother particles as observed in the particle size distribution curves of Figure A.7. However, the attrition during this interval seems to be sufficiently small to not change the mean particle size of the bed material, as discussed further below.
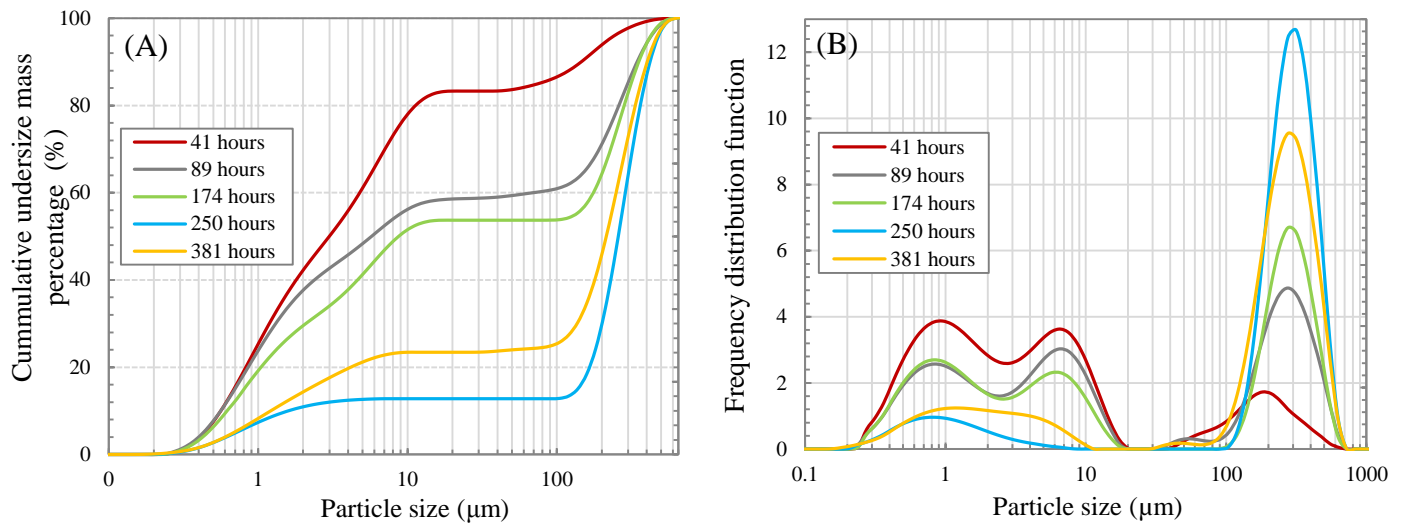
Figure A.7: Particle size distribution of elutriated particles during DFB operation: (A) Cumulative undersize distribution; (B) Distribution frequency function.

After 174 hours of operation, a change in particle size distribution is observed where particles of smaller sizes (< 550μm) remained almost invariable, but coarser particles (d_p >550 μm) became smaller as observed in Figure A.7A. As seen in Figure A.7, 53% of the material lost after 174 hours consisted of particles in the range of 0.24-15μm. This fraction could corresponds to asperities that were further removed from the initial distribution and fresh particles added to the system during this time interval. The remaining fraction of elutriated material corresponds to particles in the range of ~90-630μm, which are possibly the product of fragmentation of mother particles leading to higher material loss. Note that the experiments at high temperature were initiated within this time interval. The thermal stresses to which particles were subjected could result from increase particle fragmentation and elutriation rate as stated in Saastamoinen et al., (2008) and Coppola et al., (2012).

Particle fragmentation seems to become more significant after 250 hours of operation. This led to a shift in the PSD of the material in the bed towards a smaller particle size and a wider PSD (Figure A.6B). Attrition by abrasion may continue to be present but less intensive after 250 hours of operation. The elutriation of bed material at this operating time decreased as shown in section A.4. However, the PSD of the elutriated material changed significantly compared to that obtained after 174 hours. Approximately 13% of the elutriated particles were smaller than 10 μm with the remaining ones being in the particle size range of 104-630 μm.

The PSD of bed material and elutriated particles was also measured at the end of the experimental runs. After 381 hours of operation at different operating conditions, the bed material was completely removed from the DFB and samples were collected for PSD analysis. A shift in the PSD of limestone towards a smaller size is observed in Figure A.4B, indicating possible further particle fragmentation. The elutriated material showed

multiple peaks in the distribution where fractions between 0.2-10µm and 100-630 µm were also found. However, after 381 hours, particles in the range of 30-100 µm were also present in the collected material.

Mean Particle Size of Bed Material

Figure A.8 shows the mean particle size of bed material over time during the operation of the DFB. It is observed that the mean particle diameter increases from 438 µm to 514 µm during the first 41 hours due to losses by elutriation. Subsequently, the attrition of limestone became insignificant after 89 h of operation. Once the experiments under warm environment began (after 174 hours), particle fragmentation possibly became substantial, with particle abrasion being still a probable mode of attrition. Thus, the mean particle diameter subsequently decreased to 490 µm after this interval of time. The PSD of bed material shifted to a smaller particle size after 250 h of operation. This led to a decrease in the mean particle diameter, as displayed in Figure A.6. Particle fragmentation gained importance after this operating time, with abrasion being lower. The absence of fines produced by particle abrasion led to an increase in mean particle diameter of elutriated particles after 250 h of operation. The mean particle size of the material remaining inside the bed at the end of the experiments (after 381 hours) decreased successively. The appearance of a small fraction of particles with size ranging between 30-100µm, and the reduction of particles of other size ranges caused the mean particle diameter of elutriated particles to decrease. In general, the mean particle diameter of bed material was not considerably affected by attrition and elutriation during the experiments.
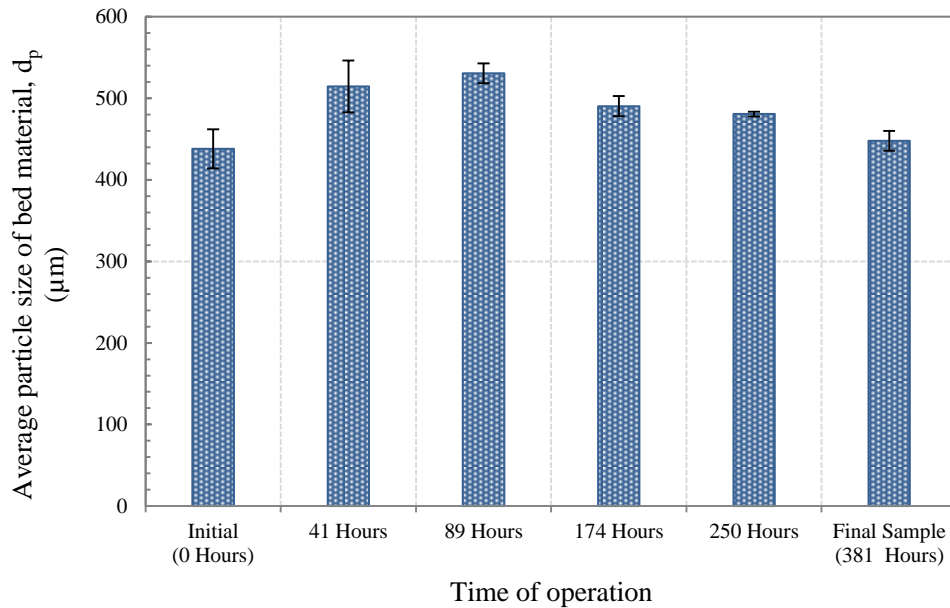

Figure A.8: Average mean particle size of bed material at different times during the operation of the DFB. Error bars correspond to standard error of measurements.
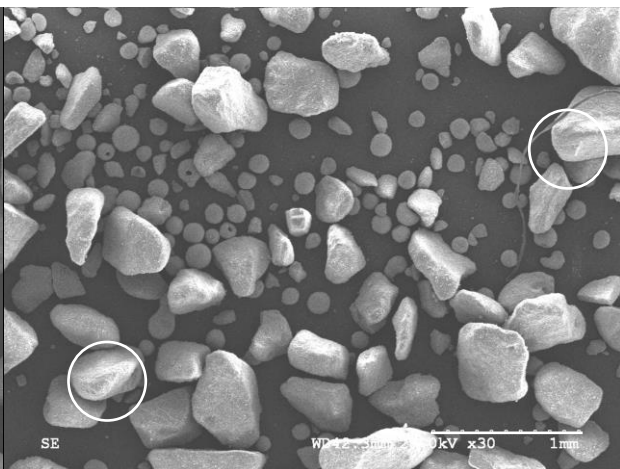
SEM Images

In order to find the effect of attrition on particle surface characteristics, selective samples from bed material were seen through a Scanning Electron Microscope (SEM) model S3000N provided by Hitachi Science Systems, Ltd. Figure A.9 shows the resulting SEM images of initial bed material and after 41, 89,171,250 and 381 hours of operation. As revealed in Figure A.9A, the initial bed material is characterized by an irregular shape with rough surface where some of the fines originated form the crushing step remained attached to the surface. Figure A.9B reveals that after 41 hours of operation, abrasion was the main mechanism of particle degradation as some of the edges and fines were still present in the system. Additionally, Figure A.9B also indicates that as stated in previous paragraphs, particles may have undergone an initial fragmentation during this period of time. Particle fragmentation could be the result of increasing gas velocity during this period of time which may have magnified the collisions between particle-reactor walls and particle-cyclone walls.

Figure A.9 illustrates how the particles became rounded and with smoother surfaces with time. This may resulted from continuous abrasion. However, it is also observed that after 171 hours some particles became smaller in size but bigger than those produced by abrasion. This confirmed the previous statement that particle fragmentation could have become important after 171 hours due to high velocities and hot bed environments. Some particles in the images presented in Figure A.9 show irregular shapes and strong edges indicating the presence of fresh material added to the system. More experimental work is needed to further investigate the attrition mechanisms of limestone particles in a DFB and the effect of operating conditions on the extend of attrition.
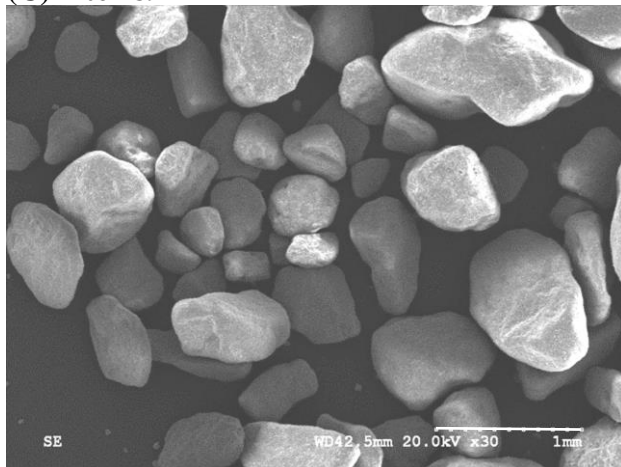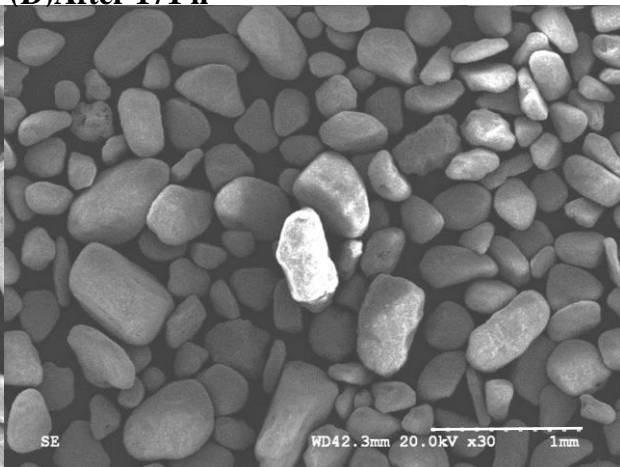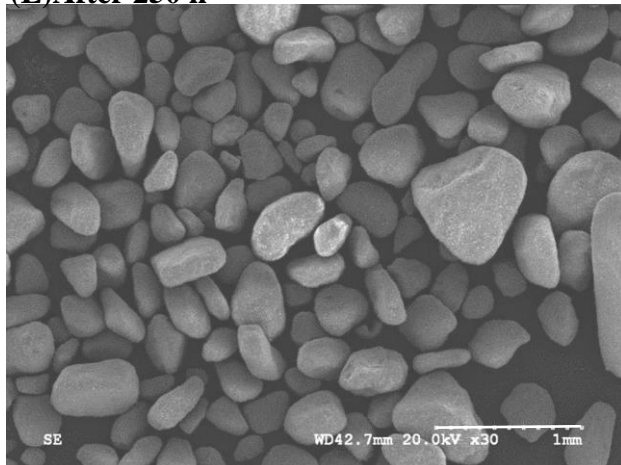
(A)Initial bed material
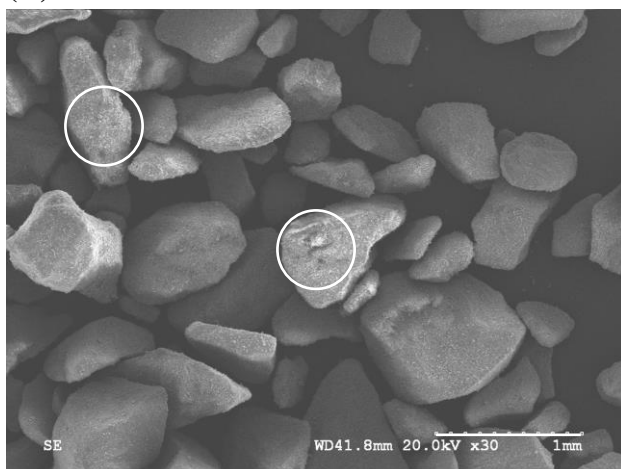
(B)After 41 h

(C)After 89 h

(D)After 171 h
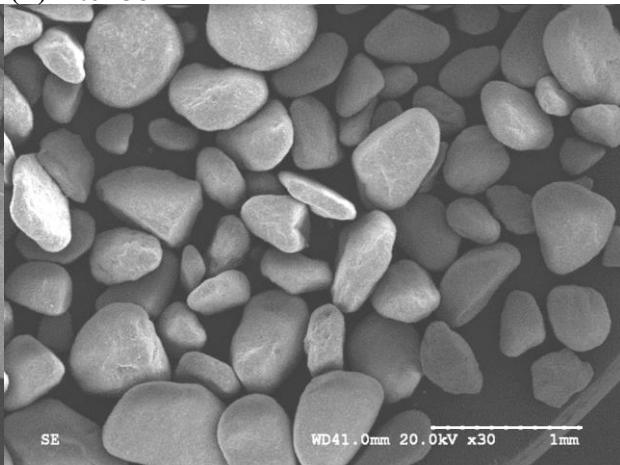
(E)After 250 h

(F)After 381 h

Figure A.9: SEM imagines of samples of bed material at different operating times

Apendix B: Instrument Calibration

Calibration of Micro Gas Chromatography

The micro gas chromatograph was calibrated with standard samples of mixtures of air and helium. Argon was used during experiments as the carrier gas for the micro GC. Two mass flow controllers, previously calibrated for helium and nitrogen were used to prepare the standard samples (see Figure B.1). The samples with known helium concentration were measured in the micro GC by means of Galaxie WorkStation1.9x software. The software generated a calibration curve based on the known concentrations, and the area under the curve of a peak on the chromatogram, corresponding to helium concentration in every standard sample.

A standard sample was analyzed on the micro GC before every experiment to verify the calibration curve. The micro GC was recalibrated every time the concentration of a standard sample deviated by more than 10% from the original value in the calibration curve.
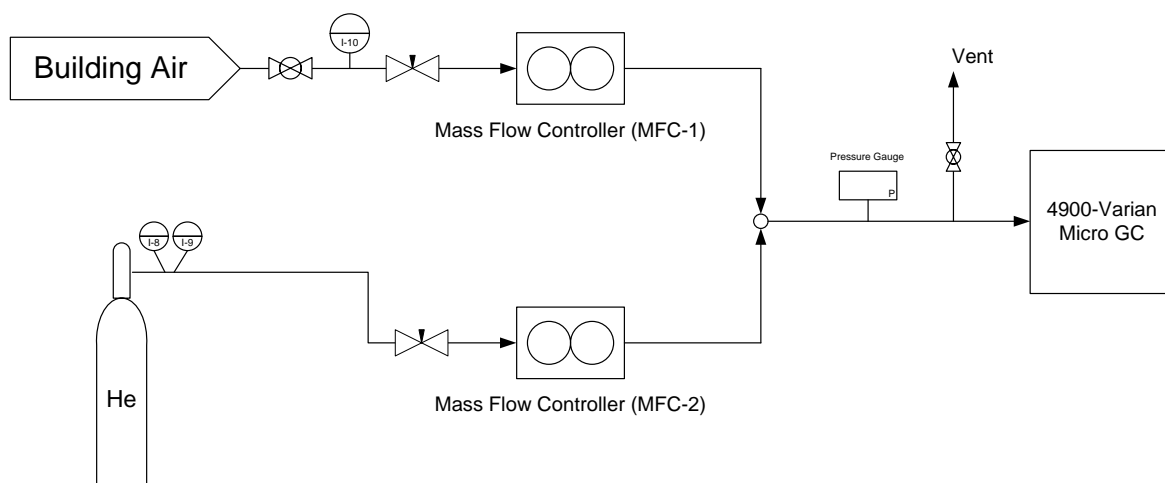
Figure B.1: Experimental set-up for calibration of micro gas chromatograph

Calibration of Pressure Transducers

A U-tube water manometer was employed to calibrate all the pressure transducers shown in Figure 2.6. The output electrical signals for the corresponding pressures were recorded by LabVIEW software. Figures B.2 to B.6 show examples of calibration curves for pressure transducers of different ranges used in this project. A list of all calibration curves can be found in the operating manual (Reyes-Ramirez, 2012).
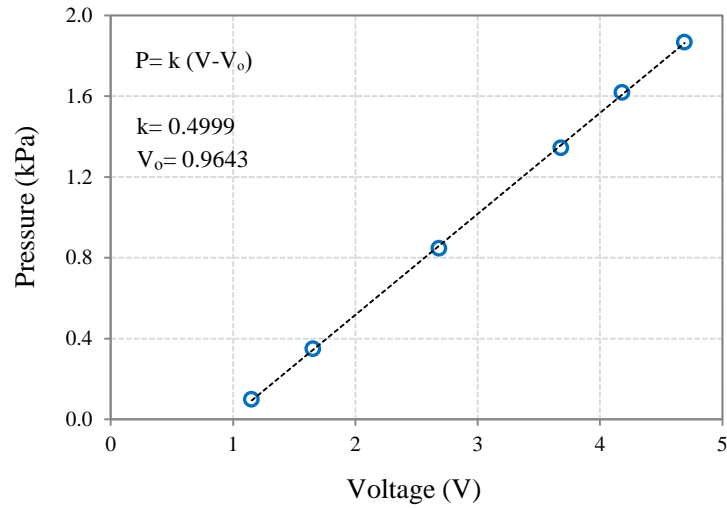

Figure B.2: Calibration curve for differential pressure transducer (PX164-010D5V). Maximum pressure = 2.1 kPa.
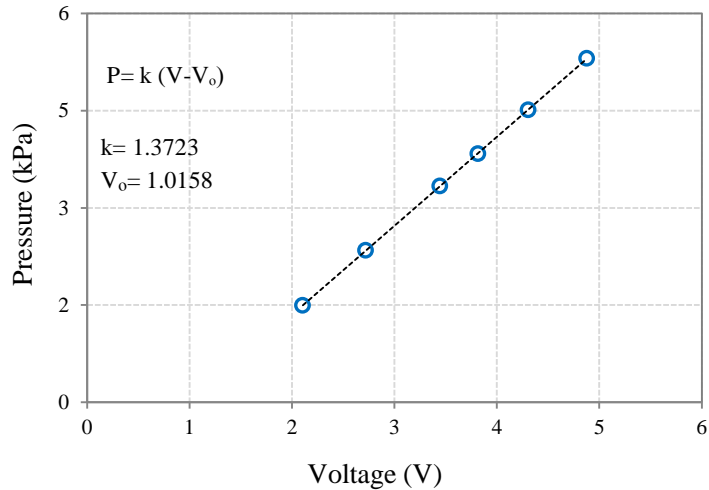

Figure B.3: Calibration curve for differential pressure transducer (PX142-001D5V). Maximum pressure = 6.7 kPa.
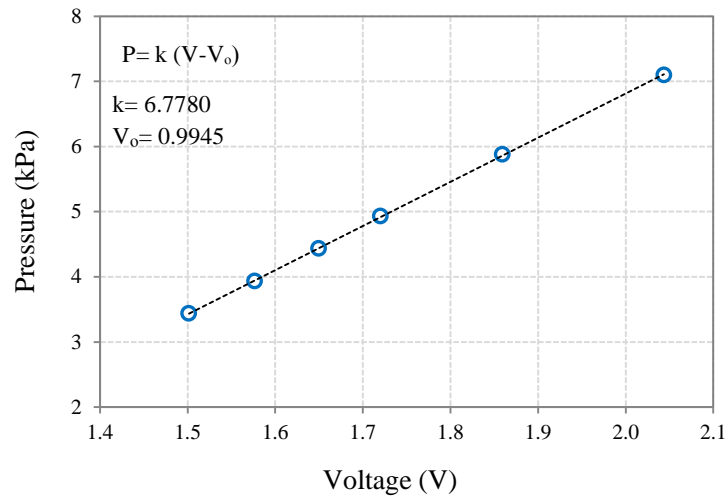
Figure B.4: Calibration curve for differential pressure transducer (PX142-005D5V). Maximum pressure = 34.5 kPa.
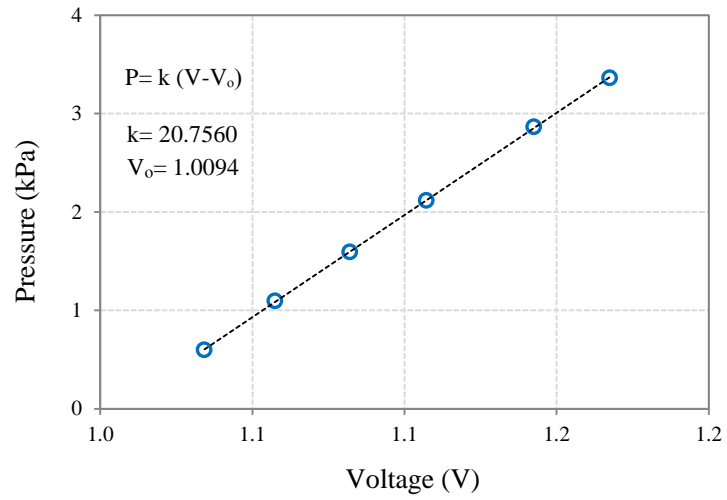

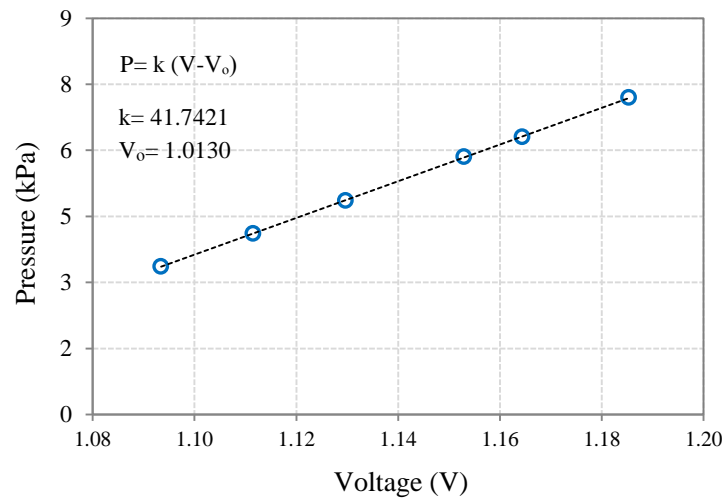Figure B.5: Calibration curve for differential pressure transducer (PX142-015D5V). Maximum pressure =103.4 kPa.

Figure B.6: Calibration curve for differential pressure transducer (PX142-030D5V). Maximum pressure = 206.8 kPa.

Apendix C: Equations

Equations Used for Data in Tables 3.1 and 3.2

1. Velocity at the onset of turbulent regime, U_c was determined based on correlation of Aba et.al. (2003) as follows:

$$U_c = \frac{Re_c}{Ar^{1/3}} \tag{C.1}$$

Where,

$$Re_c = 0.74Ar^{0.426} \tag{C.2}$$

2. Minimum slugging velocity, U_{ms} was determined based on correlation of Stewart & Davidson (1967) as follows:

$$U_{ms} = U_{mf} + 0.07\sqrt{gD} \tag{C.3}$$

4. To calculate the maximum bubble diameter, the terminal velocity for a spherical particle of d_p=1183 μm (i.e., U_t^*) was estimated. U_t^* was determined based on Kunii & Levenspiel (1969) diagram that provides values of Re_t (i.e., U_t) given the physical properties of solids and gas.

Using values of Equation (C.4) and $\emptyset = 1.0$, the Re_t = 500 (U_t^* =6.56 m/s)

$$C_d Re_t^2 = \frac{4}{3} Ar \tag{C.4}$$

Apendix D: Dual Fluidized Bed – Hot Unit

Figure D.1: Photography of Dual Fluidized Bed (DFB) facility at UBC

Apendix E: Distributor Plate of Riser and BFB

Table E.1: Specifications of distributor plates

	Riser	**BFB**
Type of distributor	Perforated plate	Perforated plate
Hole size	1.0 mm	1.0 mm
Open area	7.7 %	7.7%
Pitch arrangement	Square (3.2 mm)	Square (3.2 mm)